UCLouvain

AGRO LOUVAIN

Faculté des bioingénieurs

Hybrid catalysis for stereoselective ketone reduction

Author: Aurélien Doutry

Supervisor: Prof DEBECKER Damien (UCLouvain/IMCN/MOST)

Readers: Prof LEYSSENS Tom (UCLouvain/IMCN/MOST)

Prof STENUIT Benoît (UCLouvain/ELI/ELIM)

Academic year 2022-2023

Thesis presented in partial fulfillment of the requirements for the degree of Master in bioengineering: chemistry and bioindustries

ACKNOWLEDGMENT

In the first instance, I would like to express my gratitude to my supervisor, Prof. Damien Debecker, for welcoming me into his team as a master's thesis student. I am thankful for his availability, insightful analysis, and numerous ideas provided throughout the experiments and the writing of this work.

I would also like to extend my special thanks to Marty for all his support during my work. His assistance, both in the lab manipulations and in the writing, has been invaluable to me. But also, those puns and jokes in the corrections that lifted my spirits when I was writing this manuscript.

This master's journey would not have been the same without the warm welcome from the members of C3. I am immensely grateful for your support, valuable insights and for the team-building activities at “La Cabane”.

A special thank goes to François Devred for taking the time to explain how to use all the laboratory equipment and for his analysis of my results, to Laurent Collard for performing the chiral GC analyses, and to Geert Watson for synthesizing the Bpy-PMOs and and its help in the interpretation of the DRX results.

I am deeply grateful to Pr Tom LEYSSENS and Pr Benoit STENUIT for accepting to be readers of my master’s thesis and for being part of my defense committee.

Finalement, je voudrais remercier mes parents qui m’ont constamment soutenu depuis le début de mes études et qui m’apportant leur soutien dans mes hésitations ainsi que dans mes pertes de motivations. Je ne serais pas là où je suis sans votre aide. Un grand merci à ma sœur Faustine, qui ne manquait pas de me soutenir à sa façon mais aussi à nos nombreux moments de rigolade pendant nos blocus. Je remercie Laura pour ses corrections et son soutien inconditionnel depuis bientôt 7 ans. Un grand merci à Renald d'avoir accepté de lire mon mémoire. Cette année n’aurait pas été la même sans l’ensemble des membres du Kotelan qui étaient là le midi pour me changer les idées quand mes expériences ne fonctionnaient pas et lors de l’écriture de ce mémoire. Mais aussi pour tous les jeudis CI qui furent mémorables ou immémorables.

ABSTRACT

Production of chiral alcohol in the pharmaceutical industry has a huge impact on the environment. The utilization of current homogeneous catalysts for asymmetric reduction generates wasted chemicals for the synthesis of the catalyst and post purification of the pharmaceutical's drugs. Moreover, for the enzymatic reduction of ketones to chiral alcohol, stoichiometric concentration of NADH needs to be provided. The combination of an active metal for the regeneration of NADH and an enzyme for the synthesis of chiral alcohol is impossible because there is a mutual inactivation. New catalysts with the heterogenization of a metal active and an enzyme appear to be the future generation of catalysts. This combination generates good activity and enantioselectivity. This master thesis aims to study a hybrid catalyst for stereoselective ketone reduction.

The hybrid catalyst used in this case is the combination of a rhodium complex and an alcohol dehydrogenase (HLADH). The enzyme is used to reduce a ketone into an alcohol in presence of NADH as an electron donor and produce NAD+. The regeneration of NADH is done by the reduction of NAD+ in presence of formate with the rhodium as catalysts. The enzyme and the rhodium are supported on special material: bipyridine-periodic-mesoporous-organosilica (Bpy-PMO). PMO are new materials with uniform pores, huge specific surface and highly functionalization capability. The presence of Bypiridine inside the PMO allows the immobilization of rhodium complex and the hydroxyl group serve for the immobilization of the enzyme.

This work focuses on a model reaction. It is the reduction of 4-phenyl-2-butanone into 4-phenyl-2-butanol with in parallel the regeneration of NADH with formate as electrons donor. The study of the reaction conditions for the reduction by HLADH and rhodium complex for the regeneration was done. Rh@Bpy-PMO as catalyst demonstrates its capacity to adsorb the substrates and the interaction between HLADH and Rh@Bpy-PMO was studied. The immobilization of HLADH by APTES demonstrates remaining activity but also massive textural changes for the support of the decrease of the specific area. The current hybrid catalyst has shown no activity for the alcohol reduction, but some other possible strategies can be tested.

TABLE OF CONTENT

TABLE OF ABBREVIATION

ADH: Alcohol DeHydrogenase

API: Active Pharmaceutical Ingredients

APTES: (3-Aminopropyl)triethoxysilane

BET: Brunauer Emmett Teller

BJH: Barret Joyner Halenda

Bpy: Bipyridine

CLEA: Cross-Linked Enzyme Aggregate

$[Cp^*RhCl_2]_2$: pentamethylcyclopentadienyl rhodium dichloride dimer

$[Cp*Rh(Bpy)(H_2O)]^{2+}$: pentamethylcyclopentadienyl rhodium bipyridine complexes

COMOC: Center for Ordered Materials Organometallics & Catalysis

DRUV: Diffuse Reflectance UV-Vis spectroscopy

e.e.: enantiomeric excess

ELI: Earth and Life Institute

FWHM: Full Width at Half Maximum

GC: Gas Chromatography

GLU: Glutaraldehyde

GLU@Bpy-PMO: GLU-APTES@Bpy-PMO

GLU-Rh@Bpy-PMO: GLU-APTES-Rh@Bpy-PMO

GLYMO: (3-glycidyloxypropyl)trimethoxysilane

GSI: Gamma Secretase Inhibitor IV

HCEHCs: Hybrid ChemoEnzymatic Heterogeneous Catalysts

HLADH: Horse Liver Alcohol DeHydrogenase

HLADH-Rh@Bpy-PMO: HLADH-GLU-APTES-Rh@Bpy-PMO

HLADH@Bpy-PMO: HLADH-GLU-APTES@Bpy-PMO

ICP-AES: Inductively Coupled Plasma-Atomic Emission Spectroscopy

MLCT: Metal Ligand Charge Transfert

MOCA: Mineral & Organic Chemical Analysis

MOF: Metal Organic Framework

NADH: Nicotinamide adenine dinucleotide

NADPH: Nicotinamide adenine dinucleotide phosphate

Adjusted carbon balance: This is the addition of the number of moles of PBOL and PBON

PBOL: 4-phenyl-2-butanol

PBON: 4-phenyl-2-butanone

PMO: Periodic Mesoporous Organosilicas

Rh@Bpy-PMO: Rhodium-Bipyridine-Periodic Mesoporous Organosilicas

TEM: Transmission Electron Microscopy

UV-vis : UltraViolet-visible

XPS: X-ray Photoelectron Spectroscopy

XRD: X-Ray Crystallography

TABLE OF FIGURES

TABLE OF TABLES

Introduction

1. CONTEXT

The production of highly pure active pharmaceutical ingredients (API) can have a significant impact on the environment. The synthesis of pharmaceutical drugs requires the utilization of natural resources for the synthesis of the non-reusable homogeneous catalysts [1], [2]. The extensive use of homogeneous catalyst involves their separation after use. A large amount of solvents is then necessary for the purification of very small amounts of drug/product [3]. The yield between the different steps for the synthesis cannot be 100% at every step and intermediate purifications are required. Moreover, pharmaceuticals and other chemical compounds which come from the synthesis of pharmaceutical drugs are present in waste water due to the intensive use of water for cleaning [4], [5].

There are many enzymes that are currently used as biocatalyst for the production of chiral molecules, especially chiral alcohols [6]–[10]. The advantages of biocatalytic synthesis are that enzymes are often highly enantioselective, regioselective and can be produced in a large amount with a minor environmental impact in comparison with the usage of homogeneous catalyst as production methods [10]. Chiral alcohols can be present in the drugs or a drug precursor. Examples of drugs bearing a chiral alcohol functions are: Buspirone (Buspar®) as treatment of anxiety (3S,5R)-Dihydroxy-6-(Benzyloxy) Hexanoic Acid, Ethyl Ester-4 as intermediate for multiple anticholesterol drugs, ethyl (R)-4-cyano-3-hydroxybutyric acid is a key intermediate for the synthesis of Astrovastin an anticholestrol drug [3].

A great example of biocatalytic synthesis in pharmaceutical industries is the production of gamma secretase inhibitor IV (GSI). GSI was initially used as a treatment of Alzheimer disease but it is also used for treating cancer [12]. Figure 1 shows the production of the GSI from a hydroxy ester previously produced by stereoselective reduction of a ketone and the production of a chiral alcohol [10]. This reaction is already enzymatically done at industrial scale by Pfizer, but the enzyme is not recovered.

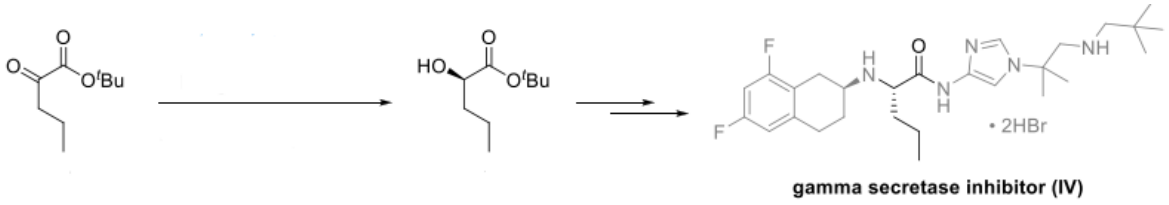

Figure 1: Process to access a hydroxy ester to produce Gamma secretase inhibitor IV [10]

From an economic point of view, the price difference for enantiopure mixtures compared with the racemic mixtures of chiral molecules is highly significant. Table 1 compares the price for various racemic mixtures and for the corresponding enantiomerically pure compounds on Sigma-Aldrich online catalogue [13]. There is a massive difference between each mixture, clearly indicating the economic interest of obtaining chiral molecules in an enantioselective way.

Table 1: Price comparison between racemic mixture and enantiopure mixture

Name	Racemic price [€/ml]	Enantiomer pure price [€/ml]
Terpineol	0.356	51.8
2-butanol	0.026	60.7
Citronellal	0.33	80.5
4-phenyl-2-butanol	6.6	147
Propylen oxide	0.5	15.9

In this context, the pharmaceutical industry is committed to building a healthier and more environmentally sustainable future. Biocatalysis appears as one of the possible solutions for the reduction of their impact on the environment. But classical production methods are not without advantages especially when the catalyst is heterogeneous because they have been uses for decades, high stability, a wide range of reactions, some of which are impossible for enzymes (reaction with C-H bond). Therefore, it is extremely profitable to try to combine biocatalysis and chemo-catalysis in order to beneficiate from the pros and avoid the cons of each technique.

This master thesis demonstrates the synthesis of a chiral alcohol, using a chemo-enzymatic cascade which combines an active metal site and an enzyme on a silica support, in the perspectives of an application in pharmaceutical industries [11].

1.1. Stereoselectivity and approach to produce enantiopure molecules

1.1.1 Definitions

Isomers are chemical compounds that possess the same molecular formula but with a different arrangement of atoms in their structure. Isomers can be divided into two main categories: constitutional isomers and stereoisomers. Constitutional isomers are characterized by different atomic sequences and therefore, don't have the same structural form [14]. Figure 2 is the representation of 2 constitutional isomers of chlorobutane, the position of the chlorine changes but the number of atoms is unchanged.

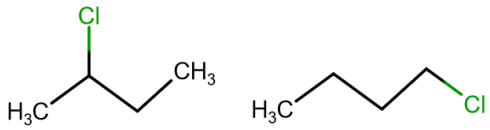

Figure 2: Structures of 2-chlorobutane and 1-chlorobutane

Stereoisomers differ from the isomers of constitutions because their atoms are linked the same way but are arranged differently in space. It is necessary to define chirality for a better understanding of stereoisomers. A molecule is said to be chiral if it cannot be superposed on its mirror image by any combination of rotation or translation. Chiral molecules contain at least one asymmetric center, and an asymmetric center is a carbon atom, which has four different atoms bound. Asymmetric carbon can also be called chiral center. Figure 3 shows the chirality concept applied to bromochlorofluoromethane.

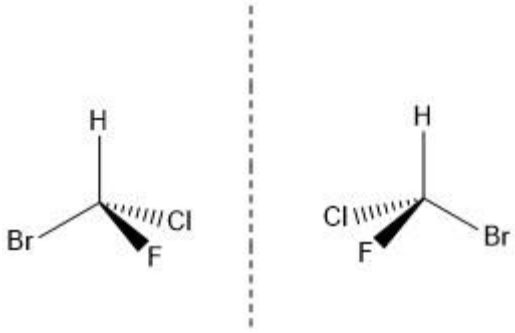

Figure 3: Chirality of bromochlorofluoromethane

There are 2 subclasses of stereoisomers: diastereomers and enantiomers. Enantiomers are chiral molecules that mirror each other without being stackable. In opposition with enantiomers, diastereomers are also non-stackable chiral molecules but here the molecules are not mirror images of each other. In Figure 4, the molecule A and B are enantiomers because they are mirror images but not superposable, molecule C and D are also enantiomers. Molecules A and D are not mirror images and non-superposable; they are diastereomers. By definition, diastereomers must have 2 asymmetric centers.

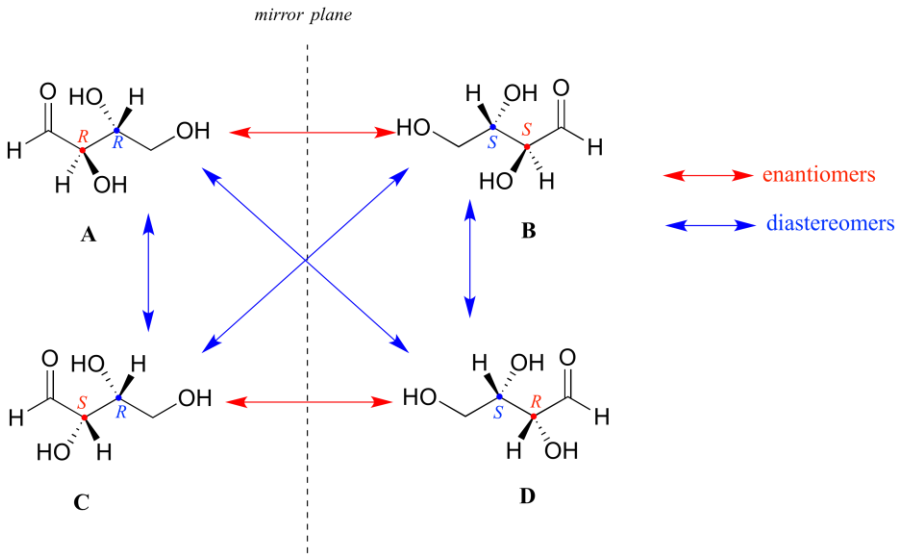

Figure 4: Comparison between enantiomer and diastereomer [15]

In the case of the stereoisomers, there are rules for designating them. This is the Cahn-Ingold-Prelog sequence rules, and the purpose of these rules is to assign the letter S or R for each stereocenter to name stereoisomers. The set of laws for naming stereoisomers will not be presented here but the nomenclature is based on the importance of the substituents on the asymmetric center to give a sense of rotation of theses substituents [16]. A mixture composed of 50% of the S-isomer and 50% of the R-isomer is called a racemic mixture. Figure 5 summarizes the classification of isomeric molecules [14]:

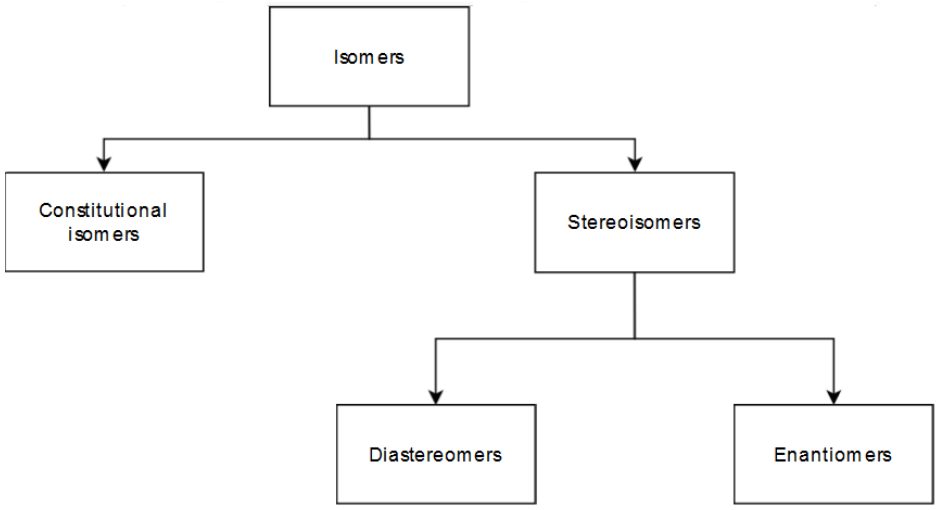

Figure 5: Classification of the different types of isomers

In nature, it is quite frequent to observe chiral molecules. As a matter of fact, 2 enantiomers can have very different properties. This can be illustrated with 4 examples:

Flavor

Aspartame has 4 isomers, but only D-Aspartame gives a sweet taste while the others do not give any taste or bitterness [17].

Odor

One of the best-known examples is limonene. Limonene exists in 2 forms, R-limonene has an odor of orange while S-limonene smells like mint [14].

Biological Effectiveness

Drugs are often sold as a racemic mixture in which only one of the two enantiomers has an effect on the organism while the other enantiomer has no impact. For example, Dichlorprop® is a weed killer in which only the R-enantiomer is active [18].

Drug Safety

In pharmacology, chirality is crucial as it is one of the reasons for the efficacy of a drug. About 56% of pharmaceutical drugs that are on the market are chiral molecules [19]. A well-known example which shows the importance

of chirality in molecules used in pharmacy is thalidomide. This drug was first sold in the 1960s as a racemic mixture of R and S-thalidomide to relieve nausea associated with pregnancy. Studies later showed that S-thalidomide had adverse effects on fetal growth. It destroyed fast-growing cells, causing deformations on the arms of newborns. It was also later discovered that even if the S-isomer was removed, there was spontaneous epimerization of R-thalidomide to form a racemic mixture. Today this drug is used to treat cancers [20].

1.1.2 Strategies for the production of a single enantiomer

The enantiomeric purity is usually expressed using the concept of "enantiomeric excess" (e.e.). By definition, the parameter is calculated as Equation 1. With R the molar fraction of the R-enantiomer and S the molar fraction of the S-enantiomer. This is a measurement of purity for chiral substances. A racemic mixture has an e.e. of 0% and a single chiral mixture has an e.e. of 100% [21]. A solution comprising 90% of component R and 10% of component S exhibits an enantiomeric excess of 80%

$$e.e. = \frac{|R - S|}{R + S} * 100 \quad (1)$$

There are 5 main methods to obtain a single enantiomer:

Chiral pool

This strategy is based on the use of chiral molecules as reagents. Indeed, reagents such as amino acids, sugars, terpenes are naturally present in nature with a very high level of enantiopurity. The chiral center(s) are preserved during their reaction. It may use a chiral center already present in the molecule to generate a different chiral center [22]. Chiral pool synthesis is the easiest manner to produce a chiral molecule, but this approach requires stoichiometric amount of enantiopure reagent which can be very expensive. Another limitation is the number of possible reactions available, which is very restricted [23].

Chiral Auxiliaries

The chiral auxiliary technique consists in the temporary incorporation of a chiral chemical compound to control the stereochemistry of a reaction. The chiral auxiliaries could temporarily bind to a reactant which will favor the

environment and decrease the activation energy to produce one of the two enantiomers. One of the problems of this technique is that to produce the chiral auxiliary it is often necessary to use another method of enantiomeric synthesis [24]. The reaction auxiliaries are generally quite expensive and often difficult to reuse/recycle. A purification step of the medium is also necessary after the synthesis [14].

Separation/Purification of the Enantiomer

Post-reaction purification is an alternative method whereby both enantiomers are generated during synthesis, but the desired enantiomer is purified at a later stage. A large array of purification methods is documented in the literature such as preparative chromatography (HPLC, GC and LC) [25][26], capillary electrophoresis [28], crystallization [29]–[31] or solvent extraction [32], [33]. Chiral separation in the case of a small amount of product is one of the best strategies to produce enantiopure compounds. However, these techniques can only be used for small chemical production [34], [35].

Asymmetric Reduction

The final approach is the use of chiral catalyst to obtain an enantiomeric pure product [36]. This method is what interests us more particularly and will be discussed further in the following section.

1.2 Asymmetric reduction

Asymmetric catalysis is a growingly significant discipline, as evidenced by the 2001 Nobel Prize in Chemistry by Knowles, Noyori and Sharpless for their work on hydrogenation and asymmetric oxidation, in the 2012 Nobel prize in chemistry by MacMillan and List for the development of asymmetric organocatalysis [37], [38]. There are two types of asymmetric catalysis: chemical catalysis and biocatalysis [39].

1.2.1 Chemical catalysis

The catalyst used in asymmetric reduction is itself divided into two subcategories: homogeneous catalysts and heterogeneous catalysts. Homogeneous asymmetric reduction catalysts are complexes composed of metal atoms surrounded by chiral ligands, and they are used in the same phase as the medium (i.e. a homogeneous liquid reaction medium). This methodology

is the most widely used. The ligands used are often Salen bases (Figure 6A) as they allow a high e.e. and are easily synthesized. Figure 6B is one example of a Salen complex for epoxidation [40]. The advantage of homogeneous catalysts is their enantioselectivity in comparison to heterogeneous catalysts.

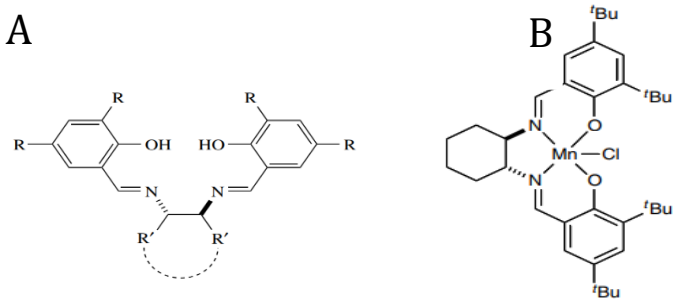

Figure 6: Salen base and metal Salen complex for epoxidation catalysis [40]

Unlike homogeneous catalysts, heterogeneous catalysts exist as solid materials, i.e. as a distinct phase from the reagents. The great advantage of a heterogeneous catalysts is their easy recovery and reusability, whereas a homogeneous catalyst is often difficult to recover, which can be very bothersome in the pharmaceutical industry, especially if the catalyst is toxic or expensive. A heterogeneous catalyst can also be used several times because it can be recovered and regenerated, whereas a homogeneous one can hardly be recycled at all.

Immobilized chiral homogeneous catalysts

Homogeneous catalysts can be immobilized on a support to make them heterogeneous. There are a multitude of techniques that allow the immobilization of homogeneous complexes, some examples can be seen in Figure 7 [41].

Chiral modification of heterogeneous catalyst

This technique uses the enantiospecific adsorption on a chiral surface where an achiral catalyst is combined with a chiral organic molecule. The two work together as a catalyst. The surface modifier influences the selectivity and activity. In these catalysts, it's a chiral organic molecule, which is chemisorb on the surface that creates a chiral environment. For example, the hydrogenation of methyl pyruvate by a supported platinum or palladium catalyst with cinchona alkaloids [42]. Another possibility is to modify a di or

polypeptide surface that is chiral with metals to turn it into a heterogeneous catalyst [41], [43], [44].

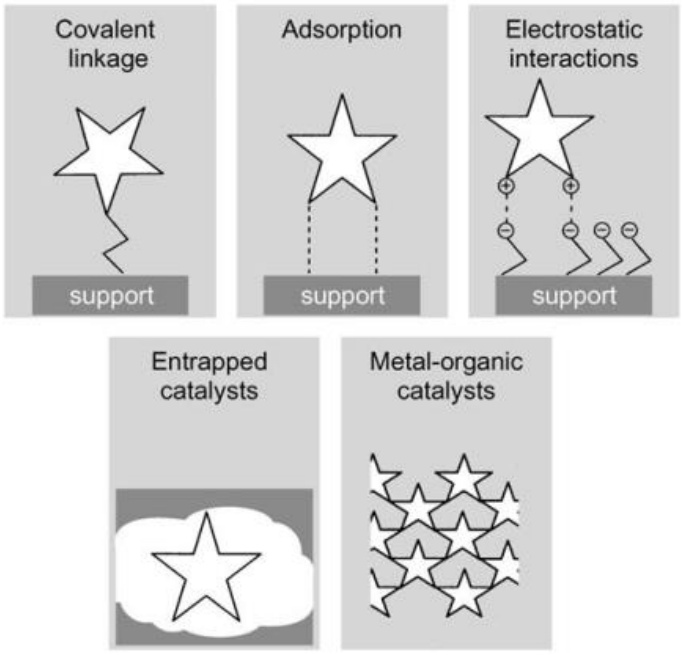

Figure 7: Strategies for the immobilization of chiral homogeneous catalysts [40]

Table 2 is a comparison of the different enantiomeric production methods for hydrogenation reactions, except the techniques of purification because it's not an approach for production but an downstream or upstream process [42].

Table 2: Pros and cons of enantiomer production for hydrogenation

Methods	Homogeneous catalyst	Immobilized chiral homogeneous catalysts	Chiral modification of heterogeneous catalyst
Enantiomeric excess	Good→excellent	Good→excellent	Good→excellent
Yield	Excellent	Good	Good
Scope	Broad	Increasing	Increasing
Industrial application	Good	Promising	Limited
Advantages	High selectivity and stereoselectivity	Easy separation	Easy separation and High activity
Disadvantages	Difficult separation of the catalyst	Decreases activity and selectivity	Limited scope

1.2.2 Biocatalysis

Biocatalysis is the utilization of natural catalyst such as an enzyme to accelerate a reaction [45]. This subject is explained more thoroughly in the next section.

1.3 Biocatalysis for asymmetric reduction

Biocatalysis has become increasingly essential in the industrial world. Enzymes are now used for enantioselective reactions as they bring significant advantages: sustainability, safety, specificity, and selectivity. While organometallic compounds require resources from earth, enzymes can be found in nature in almost unlimited quantities. There are a lot of possible reactions with enzymes in the nature and they can work under mild conditions [46]. The problem with the utilization of enzymes resides in the relatively strict pH and temperature conditions required and the limited choice of solvents. Being homogeneous catalysts, they are difficult to recover. The challenge is to implement biocatalysts into industry by finding the right reaction conditions while remaining economically competitive [47], [48].

1.3.1 Alcohol dehydrogenase (ADH)

ADH is a type of dehydrogenation enzyme which catalyzes the oxidation of hydroxyl groups into aldehydes or ketones. These enzymes use nicotinamide adenine dinucleotide (NAD+) as electrons acceptor [49]. It's necessary to have a regeneration system coupled to the redox reaction. The natural function of this enzyme is the degradation of toxic alcohols for humans and other organisms. They are also able to catalyze the opposite reaction, the reduction of aldehydes or ketones into alcohols for the regeneration of NAD+ [50]. This type of enzyme usually has two zinc active sites. They are composed of two monomers which weigh around 40 kDa. Horse Liver Alcohol DeHydrogenase (HLADH) reduces ketones in an enantioselective way which makes it very promising for the asymmetric synthesis of chiral alcohols [28]–[30]. HLADH is stable at temperatures below 45 °C. Above this temperature, the enzyme will undergo thermal denaturation. It is interesting to know the structure and the surface composition of the enzymes for their immobilization, because the choice of the immobilization method will depend on the presence of certain amino acids on the surface. Figure 8 shows the 3D structures of the HLADH. On this same figure in fluorescent green, we notice the large presence of lysine

residues on the external surface of the enzyme. This will play an important role in the immobilization (see 1.5.5).

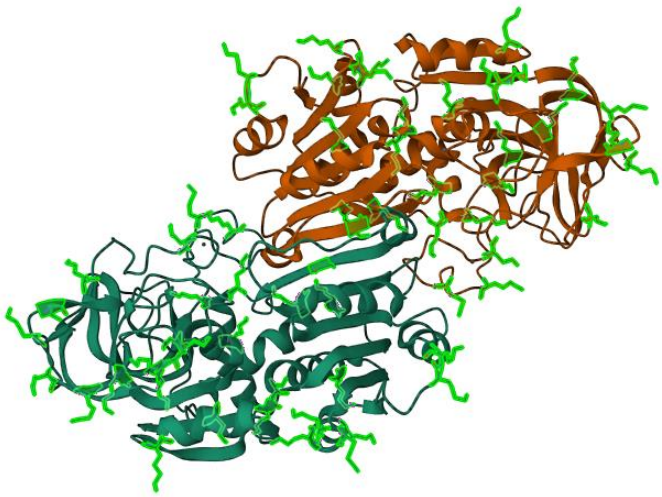

Figure 8: The three-dimensional structure of HLADH (7UHD) [52]

1.3.2 Cofactor in biocatalysis

Cofactors are non-protein molecules bound to a protein and regulate its activity (most of the time, an enzyme). Cofactors assist biochemical transformations; without their presence, reactions cannot be done. There are 2 major categories of cofactors: inorganic and organic. Inorganic cofactors are typically metal ions such as zinc, iron, or manganese. NADH (Nicotinamide Adenine Dinucleotide) or NADPH (Nicotinamide Adenine Dinucleotide Phosphate) are organic cofactors. NADH is present in all living cells; it is the combination of two nucleotides (adenine nucleobase and nicotinamide) [54]. Serving as an electron carrier molecule, it exists in 2 forms: NAD+ and NADH for the oxidized and reduced form respectively. Figure 9 shows the structure of NAD+ and NADH the red circle points to the difference between the NAD+ and NADH [55], [56]. The molecular weight of NADH is 663.43 g/mol and the molecular width is approximately 1 nm x 2 nm [57].

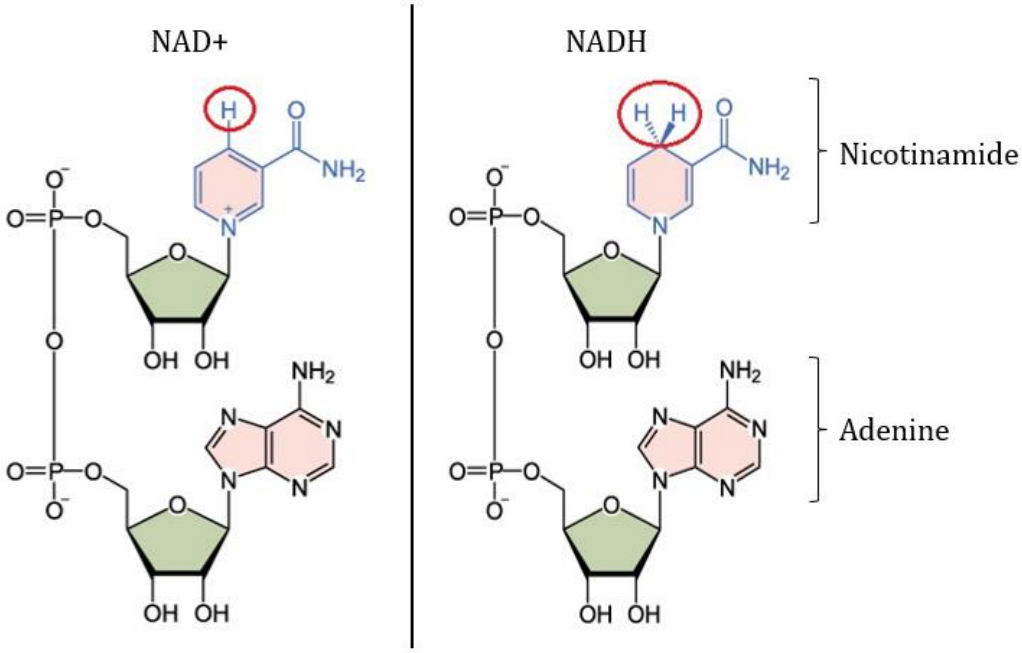

Figure 9: NAD+ and NADH structure adapted from [56]

1.3.3 Cofactor recycling

Cofactor regeneration can be done electrochemically [58], [59], photochemically [60]–[62], enzymatically [63], [64] or chemically [54]–[56]. The following section discusses more precisely of these recycling methods.

1.4 Integrated cofactor recycling

1.4.1 Electrochemical cofactor recycling

Electrochemistry offers a very efficient way to regenerate NADH from NAD+ by the utilization of an electrode as electron donor. This technique is efficient and can be green if the electricity is produced by renewable energy. The problem with this technique is the possible inactivation of NADH by dimerization. There are 2 steps involved in direct electrochemical reduction of NAD+ to NADH. The first one is the reduction of NAD+ to NAD radical and the second one is the reduction of NAD radical to NADH. The second step is very slow and 2 NAD radicals can react together to form $(NAD)_2$ dimer as a side product which is not active [59], [68], [69].

1.4.2 Photochemical cofactor recycling

The massive advantage of using photochemistry is the opportunity to use the sun as a source of energy. In nature, photosynthesis is the recycling system for cofactors. However, research about this technique is rare because the turnover frequency is low and it is essentially homogeneous catalysis [61]. Figure 10 is the description of natural photosynthesis on the left and the artificial photosynthesis by xanthene dyes [70].

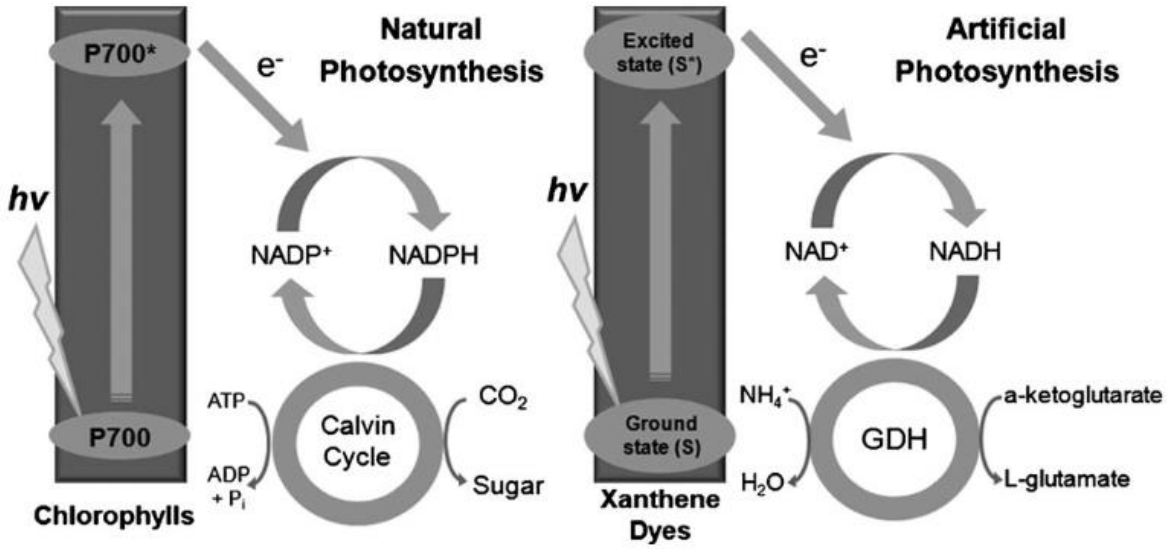

Figure 10: Natural photosynthesis (left) and artificial photosynthesis (right) [70]

1.4.3 Enzyme cofactor recycling

This is the only method applied currently at the industrial scale. The use of enzymes offers the same advantages that are already described in the biocatalysis section. There are 2 strategies for the regeneration of NADH, illustrated in Figure 11. Two enzymes – one for the synthesis and one for the NADH regeneration – can be coupled or only one enzyme for the two reactions. Unless the enzymes are immobilized, it is possible to have unwanted interactions between the enzymes such as competitive inhibition or interference between the cofactors. Moreover, enzymes being very sensitive to the reaction conditions, finding optimal reaction conditions can be complicated. The most widely used enzymes for cofactor regeneration are Glucose dehydrogenases, Fructose dehydrogenases, Phosphite dehydrogenases, alcohols hydrogenases [71], [72].

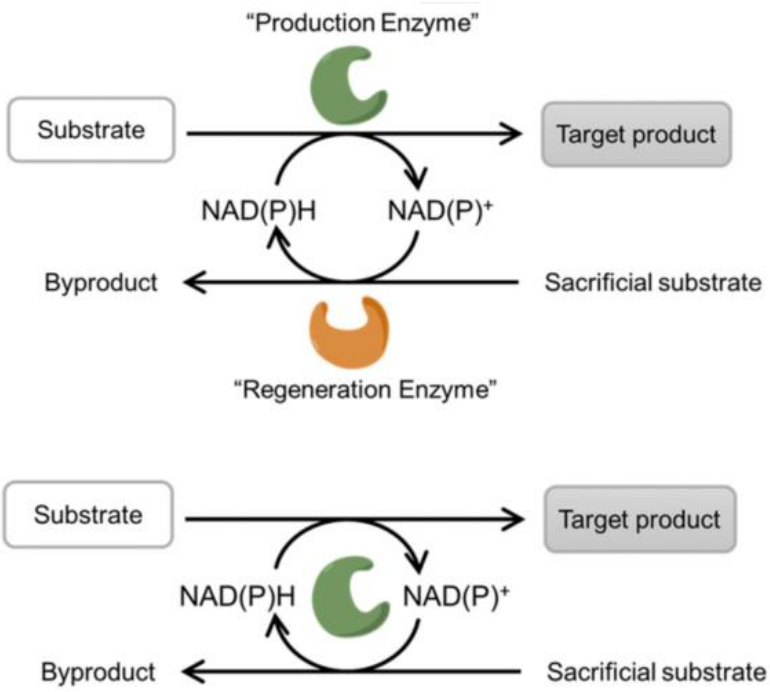

Figure 11: Schematic representation of the two strategies for NAD(P)H regeneration [71]

1.4.4 Chemical cofactor recycling

There is a multitude of organometallic systems for NADH regeneration in the literature. These include Au [73], Pt [66], Ir [65], [74], Ru [71] or the best known and most widely used of all via Rh [74]–[77]. The pentamethylcyclopentadienyl rhodium dichloride dimer ($[Cp^*RhCl_2]_2$) and the pentamethylcyclopentadienyl rhodium bipyridine complexes ($[Cp*Rh(Bpy)(H_2O)]^{2+}$) are the most used complexes as a catalyst for NADH regeneration [78]. These complexes have the advantage of being very efficient, using cheap electron donors such as formate or alcohols and are water soluble. They are also very stable between pH 5 and 9 and under temperatures of up to 80 °C [77]. For all these reasons, they are used for the regeneration of NADH. The structure of these two complexes can be seen in Figure 12.

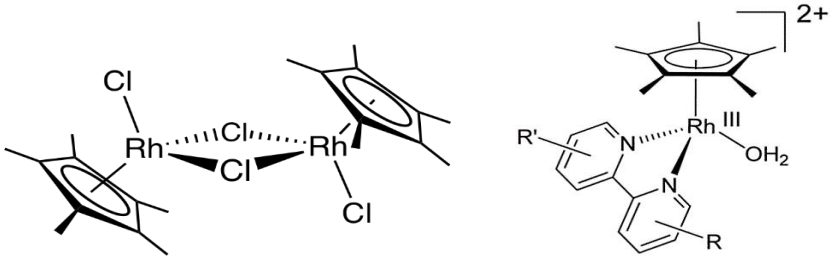

*Figure 12: ([Cp*RhCl2]2) on the left and ([Cp*Rh(Bpy)(H2O)]2+) on the right [77]*

The mechanism of regeneration by rhodium catalysts is shown in Figure 13. This mechanism is currently the most plausible and is widely accepted within the scientific community [67], [79]. The first step is the fixation of formate on the complex, it produces one molecule of CO_2. The second step is the binding of NAD+ to the complex. There are two possible pathways for the attachment to the complex. Finally, NAD+ is reduced by hydrogen transfer from the formate, this final step returns the catalyst to its initial state.

This regeneration system works well but it cannot be combined with an enzyme, because this leads to mutual inactivation [80]–[82]. Recently, it was demonstrated that the problem can be solved by immobilization of the rhodium complex. This immobilization will also provide the possibility to reuse the catalyst easier.

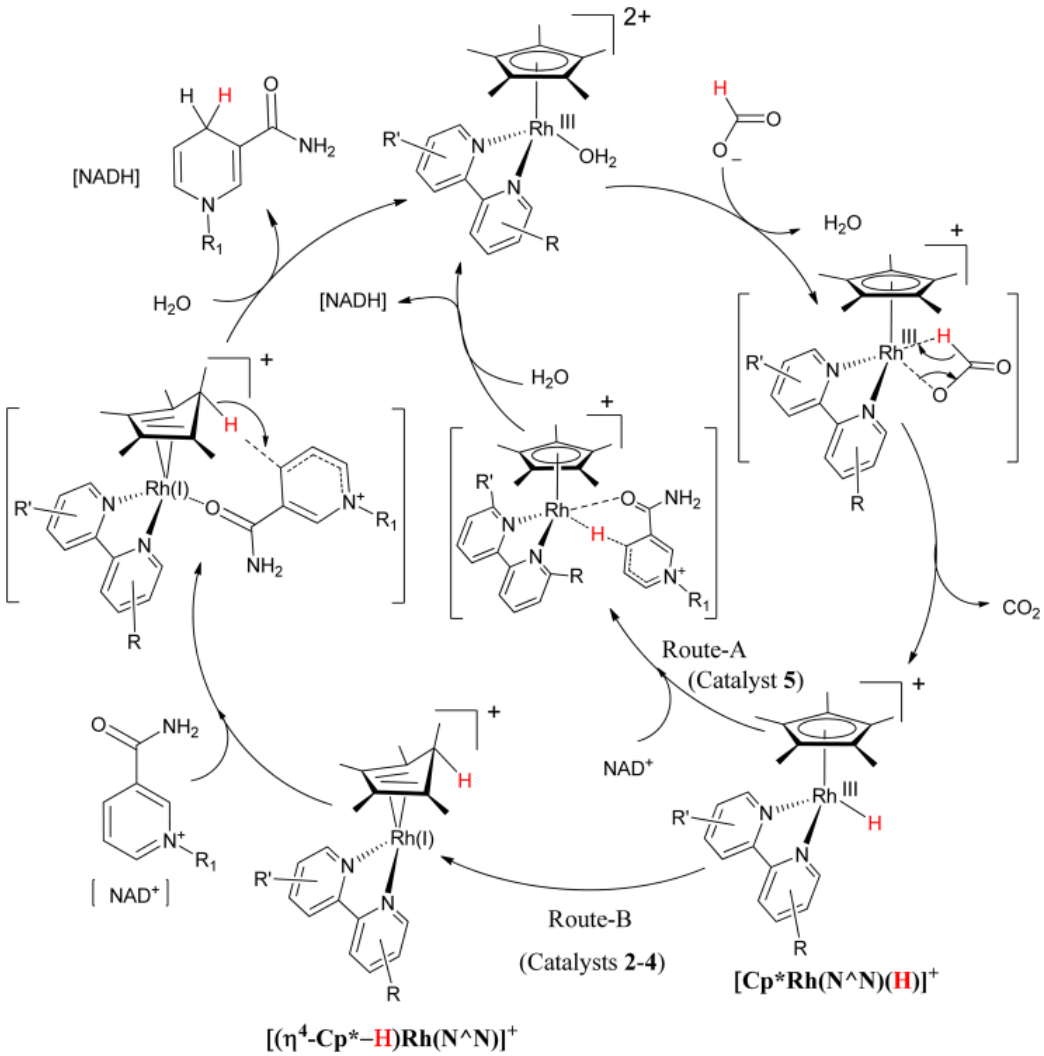

Figure 13: Mechanism for the regeneration of NADH from formate using a Rh catalyst [77]

1.5 Hybrid catalysis and hybrid catalyst

1.5.1 Rhodium immobilization

Methods of immobilization of metal complex in the literature are numerous. Covalent bounding, ionic interactions, π-π-stacking, physical adsorption, coordination, etc [83].

1.5.2 Bypiridine as chelating agent

Immobilization of this rhodium catalyst can be done by chelating the homogeneous catalyst with bipyridine (Bpy) [87]–[90]. Bpy is one of the most common chemical compounds used as a chelating agent for metals [84], [85]. Six isomers of bipyridine exist but only two isomers are prominent: 2.2'-bipyridine is a chelating agent and 4.4'-bipyridine an herbicide precursor as depicted on Figure 14 [86].

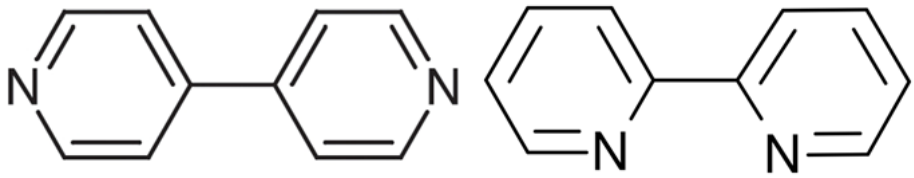

Figure 14: Structure of 4.4'-bipyridine on the left and 2.2'-bipyridine on the right

Bpy alone is soluble in water, but some brand-new materials allow the incorporation of organic compounds such as Bpy inside its structure.

1.5.3 Periodic mesoporous organosilicas (PMO) as heterogeneous support

PMOs are nanostructured materials with (2–50 nm) pores. Thanks to the suitable pore volume, well-accessible porous framework, large surface area, possibility of modifications of pore structure and the functionalization possibility. PMOs are interesting for a plenty of applications such as catalysis, gas storage, biomolecule adsorption, drug delivery, chromatography and many more, making PMOs highly attractive. Figure 15 shows a typical PMOs structure with R organic groups which can be changed [91]–[93].

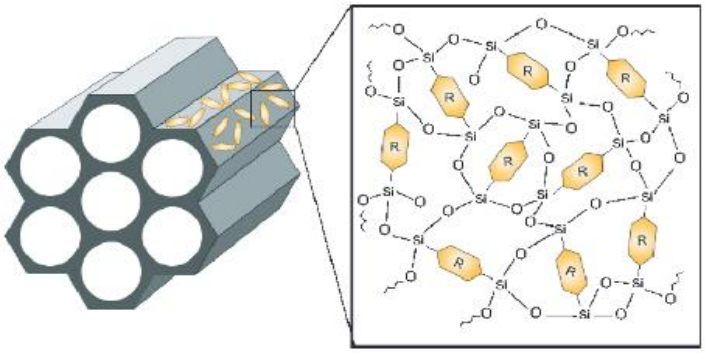

Figure 15: Schematic structure of PMOs with R as organic groups [91]

It is possible to modify the structure composition of PMOs. The goal of this modification is to provide new properties to the PMOs. A well-known PMO modification is the incorporation of bipyridine moieties inside the organosilica network. Various metal complexes can then be immobilized and thanks to the large pore size of the Bpy-PMO, diffusion inside the pores enables substrates and products to migrate easily. Bpy-PMO can thus be used as heterogeneous support for immobilization of complex in catalysis [74]–[77]. Figure 16 shows the rhodium complex chelated on the surface of the Bpy-PMO surface. The $[Cp^*RhCl_2]_2$ complex dimer divides into 2 equal units and the rhodium atom coordinates with 2 nitrogen atoms.

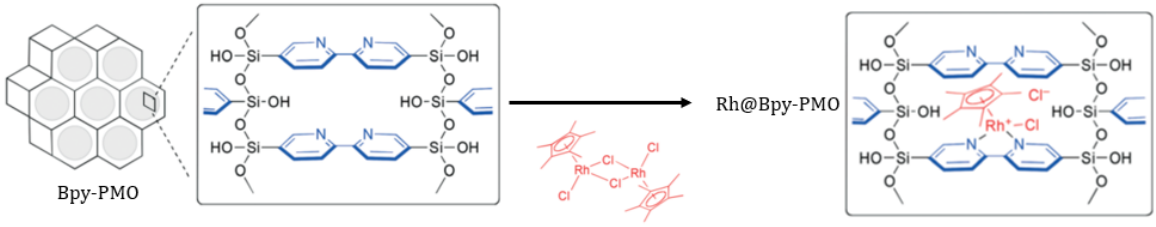

Figure 16: Immobilization of $[CpRhCl_2]_2$ on the surface of Bpy- PMO adapted from [98]

1.5.4 Hybrid catalysis

Hybrid catalysis is the integration of multiple catalysts together inside one system. The catalysts have different functions independent of each other [99]. Hybrid catalysis here is the combination of HLADH and the Rhodium-Bipyridine-Periodic-Mesoporous-Organosilica (Rh@Bpy-PMO). However, the homogeneous nature of the enzyme remains an important drawback. A good solution would be to immobilize it on a support.

1.5.5 Enzyme immobilization

Despite the significant advantages they offer, the utilization of enzymes in the industry is constrained by the need for restrained conditions due to their fragility. Additionally, the high cost and enzyme loadings required for industrial applications impose limitations on the use of free enzymes. Immobilization of enzymes can be used in order to surpass all these problems and offer the opportunity to recycle and reuse the enzyme [100], [101]. Moreover, after immobilization, the enzyme can be easier to store, because their thermal resistance and pH resistance can be improved. There are many strategies for immobilizing enzymes on organic or inorganic supports. The enzyme immobilization techniques can be divided into 2 major categories: physical methods and chemical methods. Physical immobilization is identified as all the methods where the enzyme is separated from the medium by weak interactions such as hydrogen bonds, van der Waals forces, entrapment, or hydrophobic repulsion. Chemical methods are all the immobilization techniques with the creation of covalent bonds between the support and the enzyme [102], [103]. Figure 17 is a summary of the different enzyme immobilization methods.

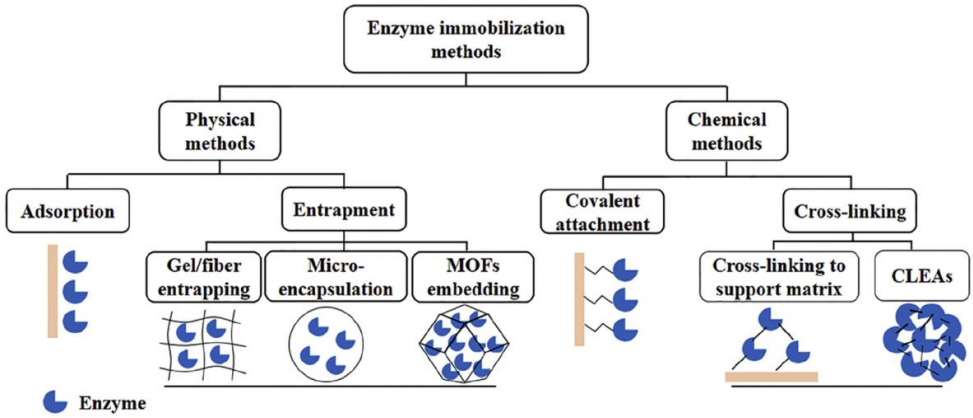

Figure 17: Methods for enzyme immobilization [102]

In this work, the only method of immobilization that will be used is the covalent attachment, and it will be the only technique described in this manuscript. This technique is chosen because it is the most common, the strongest and the simplest for enzyme immobilization.

Covalent attachment consists of the creation of a covalent bond between the support and specific amino acids (e.g. lysine, cysteine, aspartic amino acids

or glutamic amino acids) [104]. There is a wide array of organic groups suitable as covalent binding chemicals such as cyanogen bromide, carbodiimide and glutaraldehyde [105].

Covalent attachment for silica-base materials is often based on the functionalization of the silanol groups with amines such as (3-Aminopropyl) triethoxysilane (APTES). Then, glutaraldehyde (GLU) is added to the solution as a coupling agent. one aldehyde group reacts with the amino groups of APTES. Finally, the lysine residues of enzymes react with the remaining aldehyde group, to create a imine bond [106]–[108] [109]. Figure 18 is a summary of the mechanism of immobilization with APTES on a silica support.

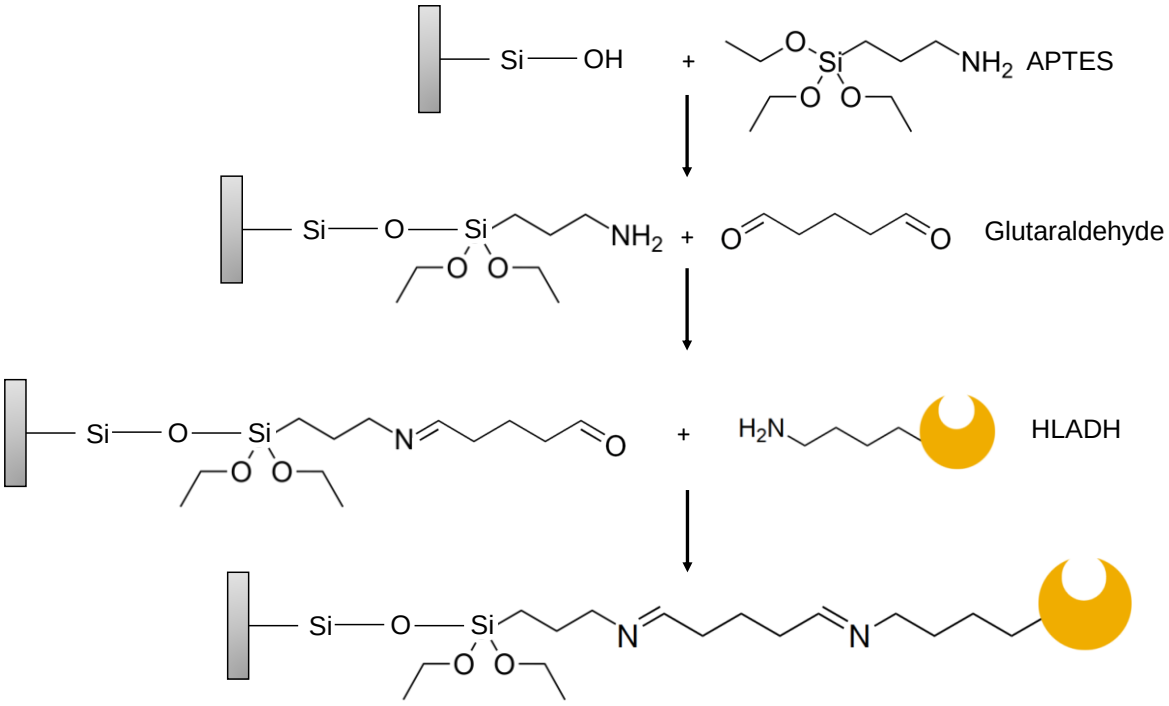

Figure 18: Mechanism of immobilization with APTES

Covalent attachment provides a good stability and recyclability for the enzyme. However, this strong interaction may affect the activity of the enzyme because those modifications can cause denaturation or active site blocking [110].

1.5.6 Hybrid ChemoEnzymatic Heterogeneous Catalysts (HCEHC)

HCEHCs are heterogeneous catalysts which contain both a chemo-catalytic function and an active enzyme [111], [112]. The advantage of HCEHCs is that the combination of the enzyme and a metal can bring a cooperative effect as well as a proximity which limits diffusion problems [113]. One type of particle is also more convenient for handling during filtration and their use in a fixed bed. However, the challenge with this catalyst type lies in discovering appropriate methods for their preparation while preserving the activity of both partners [114].

1.6 Reaction of interest in this study

This work focuses on the enantioselective reduction of a ketone to a chiral alcohol. The most common methods are those using reducing agents such as $LiAlH_4$ or $NaBH_4$ modified with a chiral molecule. The problems with these reactions are that the synthesis of the reducing agent is not green and it is consumed stoichiometrically [115]. It is also possible to carry out this reaction using an homogeneous catalyst, as the CBS (Corey-Bakshi-Shibata) catalysts which are chiral oxazaborolidines (Figure 19A)[116]. There is also the so-called MPV reduction (Meerwein-Ponndorf-Verley) which is the reduction of a carbonyl to an alcohol in the presence of a sacrificial alcohol and a chiral catalyst possessing Lewis acidity, which is often an aluminum alkoxide (Figure 19B)[117]–[119]. Here, a biocatalytic route will be pursued, using HLADH as the biocatalyst.

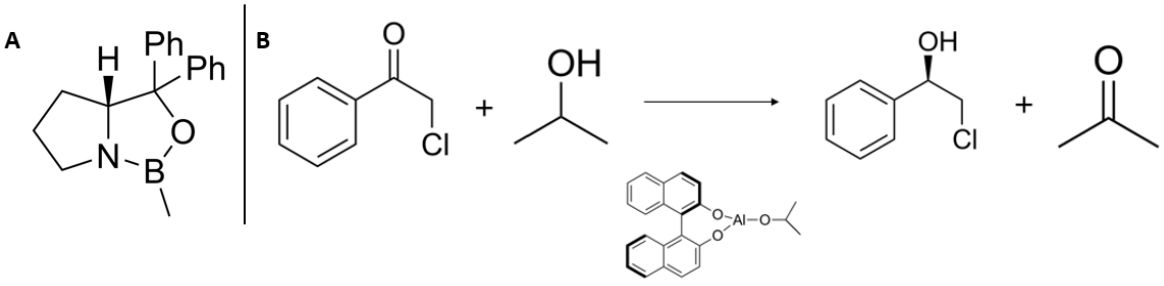

Figure 19: A) Chiral oxazaborolidine B) MPV reaction by aluminum alkoxide catalyst

The main objective is to investigate a model reaction of the reduction of 4-phenyl-2-butanone (PBON) to 4-phenyl-2-butanol (PBOL) by HLADH. This

substrate is not of economic or pharmaceutical interest, but it is inexpensive and since HLADH is not very specific, the choice of the substrate is not a major factor. In addition to PBON, the enzyme needs NADH. This gives the following reaction on Figure 20:

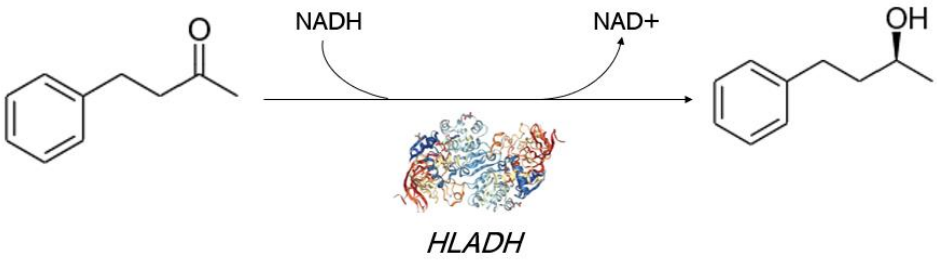

Figure 20: Reduction of PBON into (S)-PBOL by HLADH

This reaction works under mild reaction condition, and it is possible to achieve high conversion levels. Without the presence of NADH as the cofactor, the reaction is not possible. The reduction of each molecule of PBON requires the oxidation of one NADH molecule. The large-scale application of this reaction becomes highly complex due to several factors. Firstly, the exorbitant cost of NADH, coupled with its low stability, poses challenges. Secondly, the accumulation of NADH in the medium poisons the enzymes, and necessitates post-synthesis purification, which further complicates the process [72], [120]. The solution is to follow how nature works by recycling NAD+ into NADH.

Previously, a homogeneous rhodium complex was described as a good regeneration catalyst by the oxidation of formate to CO_2. Unfortunately, it was shown that when HLADH and the rhodium complex are combined in solution, a mutual deactivation occurs through both enzyme denaturation and complex deactivation. This problem was solved by the heterogenization of the rhodium complex on a Bpy-PMO material [80]. The cascade with Rh@Bpy-PMO and the homogeneous HLADH works and avoids mutual deactivation, but in this study the enzyme was still used in its free form, as a homogeneous catalyst. Our strategy is to immobilize the enzyme on the Rh@Bpy-PMO, providing proximity between the enzyme and the rhodium which will limit diffusion

limitations and possibly bring cooperative effect. The entire reaction is on Figure 21.

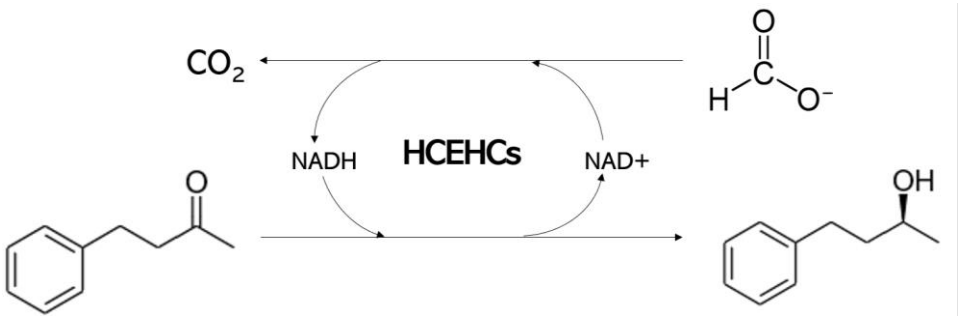

Figure 21: Reduction of PBON into PBOL and the regeneration of NADH by a HCEHCs

2. OBJECTIVES

This work is part of Marty Kinnaer's PhD thesis, which aims to investigate hybrid catalysts for various types of reactions. The primary focus of this study is to explore a model reaction involving the reduction of 4-phenyl-2-butanone (PBON) to 4-phenyl-2-butanol (PBOL) using a hybrid catalyst consisting of HLADH and a rhodium complex immobilized on a Bpy-PMO support.

The main tasks involved in this work include studying the reaction conditions for PBON reduction and NADH regeneration, as well as investigating the interactions among the different reagents. The characterization and catalytic testing of the immobilized enzyme and rhodium complex are also important objectives of this research. Ultimately, the aim is to produce and characterize a first hybrid catalyst.

3. STRATEGY

The strategy to achieve the objectives is divided into several steps:

Firstly, the temperature optimization for the reduction of PBON using free HLADH is investigated. The impact of each reagent involved in the cascade reactions and the enantioselectivity of free HLADH are studied.

Secondly, the temperature optimization for $[Cp^*RhCl_2]_2$ is performed. The characterization of Bpy-PMO before and after grafting the rhodium complex is conducted to assess its impact on the structure. Rh@Bpy-PMO is tested as a catalyst for NADH regeneration and PBON/PBOL reduction. The leaching and reusability of Rh@Bpy-PMO are also investigated.

Thirdly, cascade reactions using free HLADH with Rh@Bpy-PMO and $[Cp^*RhCl_2]_2$ as NADH regeneration catalysts are tested (in attempt to reproduce the work of Inagaki et al. [80]). Enantioselectivity of this final cascade is also evaluated in this section.

Finally, the characterization of Bpy-PMO and Rh@Bpy-PMO after the reaction with APTES and GLU is conducted to observe changes in structure, textural properties, and chemical functions. The study includes the immobilization of HLADH on Bpy-PMO and a comparison with free HLADH as a catalyst, particularly in terms of enantioselectivity for PBON reduction. The

analysis of HCEHCs loaded with both the rhodium complex and HLADH and the quantification of HLADH on the catalysts are performed. First attempts of cascade reaction with this hybrid are made.

Experimentals

4. MATERIALS AND METHODS

4.1 Catalysts preparation

4.1.1 Bpy-PMO synthesis

The PMO was produced by the Center for Ordered Materials Organometallics & Catalysis (COMOC) of the Ghent University, by PhD candidate Geert Watson, under the supervision of Prof. Pascal van der Voort. They use 2 monomers for the production of the PMOs in an aimed loading of 20% of the Bipyridine-PMO monomer (5.5'-bis(triethoxysilyl)-2.2'-bipyridine) and 80% of ethane-PMO monomer (1.2-Bis(triethoxysilyl)ethane). To a 250 mL flask equipped with a screw cap and a stirring bar, 0.973 g (1,372 mmol) Brij-76 and 2.92 g (50 mmol) NaCl were added to 50.63 mL (2.81 mol) H_2O after which 3.73 mL (44.76 mmol) of $HCl_{(aq)37\%}$ was added. The resulting mixture was continuously stirred at 50 °C for 2 hours. Another solution was made with the prepared precursors. This was achieved by adding 0.5 g (1.0146 mmol) of BTBP and 1.14 mL (3,359 mmol) BTEE to 0.97 mL EtOH in a vial. The vial was subsequently put in a shaker for 5-10 minutes until a homogeneous solution was formed. The as-formed precursor solution was added dropwise to the surfactant solution while stirring at 50°C after which the whole solution was continuously stirred for 24 hours at 50 °C. Following this step, the flask was moved to an oven where the reaction mixture was heated to 90°C for 24 hours (heating ramp of 2 °C/min). After removing the flask from the oven, the formed solids were collected by (vacuum assisted) filtration using a Nylon 0.45µm filter. The residue was washed with EtOH, after which the dried solids were redispersed in an acidified EtOH solution containing 576.32 mL EtOH and 15.38 mL $HCl_{(aq,\ 37\%)}$ (0.312 M). This mixture was left to stir for 20h at room temperature to allow the extraction of the surfactant from the porous PMO framework. (Vacuum assisted) filtration was applied to collect the residue, after which the latter was thoroughly washed with EtOH until a neutral pH was reached. Upon drying the solids under vacuum conditions at 120°C for 12h, the final $BiPy_{20}$-Et_{80}-PMO was obtained [96]

4.1.2 Rh@Bpy-PMO synthesis

The synthesis of Rh@PMO is based on the report of Inagaki et al. [58]. A suspension of 13.6 mg $[Cp^*RhCl_2]_2$ (powder, 96%, TCI) in 30 mL of MeOH (liquid, >98.8%, TCI), was stirred at room temperature for 4h under N_2 for the deoxygenation of the solution. Bpy-PMO (200 mg) was transferred into this solution in a glove box under argon atmosphere. The resulting suspension was stirred at 60 °C for 21h. The reaction mixture was filtered via a vacuum-assisted filtration through 0.22 µm filter. The obtained solid was washed 3 times with 10 mL of MeOH to eliminate unattached Rh complex residues with a theoretical rhodium loading of 0.22 $mmol_{Rh}/g_{Bpy\text{-}PMO}$. The pale-yellow solid material was dried under vacuum for 24h at 25 °C to give Rh@Bpy-PMO.

4.1.3 APTES@Bpy-PMO and APTES-Rh@Bpy-PMO synthesis

The PMOs (100 mg) was degassed at 80°C under vacuum for 24h. After cooling to room temperature under vacuum, the solid is suspended in 10 mL of water saturated toluene (liquid, >99.5%, Roth), and a dynamic vacuum was applied to force the solution into the pores of the PMOs until effervescence stopped. A test without the dynamic vacuum was also done. To this solution, 5 mL of APTES (liquid, 99%, Sigma) and 10 mL of water saturated toluene were added. The resulting mixture was stirred for 24 h at room temperature under N_2-atmosphere. Separation was carried out via vacuum-assisted filtration through a 0.22 µm mesh. The resulting solid was then washed three times with 10 mL of a water-saturated-toluene and 3 times with 10 mL of acetone (liquid, >99.5%, Sigma). Functionalized PMOs were dried under vacuum at 60 °C for 24h and then stored in a desiccator at room temperature. Protocol adapted from [106], [121]–[123].

4.1.4 APTES-GLU@Bpy-PMO and APTES-GLU-Rh@Bpy-PMO synthesis

20 mg of APTES@Bpy-PMO or APTES-Rh@Bpy-PMO were functionalized and then dispersed in a mixture of 5%v/v of glutaraldehyde (liquid, 50%, TCI) in Phosphate-buffered saline (PBS) at pH 7. The mixture was stirred for 1h at room temperature. They were then washed three times with 10 mL of PBS. Functionalized PMOs were dried and then stored in a desiccator at room temperature.

To simplify writing the catalyst names, APTES-GLU@Bpy-PMO and APTES-GLU-Rh@Bpy-PMO will be written GLU@Bpy-PMO and GLU-Rh@Bpy-PMO.

4.1.5 APTES-GLU-HLADH@Bpy-PMO and APTES-GLU-HLADH-Rh@Bpy-PMO synthesis

20 mg of GLU@Bpy-PMO or GLU-Rh@Bpy-PMO was immersed into 10 ml PBS pH 7 and 1,5 mg enzyme/ml for 1h at room temperature in an incubator shaker with 300 rpm shaking speed. Then, the immobilized silica gel was washed and filtered 3 times with PBS buffer. The HLADH solution, after immobilization, and the filtrate were kept together for protein assay to determine the amount of immobilized HLADH with Bradford method. Finally, the powder is suspended in PBS buffer at pH 7, and stored in the fridge at 7°C [124].

To simplify writing the catalyst names HLADH-APTES-GLU@Bpy-PMO and HLADH-APTES-GLU-Rh@Bpy-PMO will be written HLADH@Bpy-PMO and HLADH-Rh@Bpy-PMO.

4.2 Characterization methods

4.2.1 UV-vis spectroscopy

Ultraviolet – visible (UV – vis) spectroscopy includes absorption spectroscopy and reflectance spectroscopy in the UV – vis spectral region. Molecules containing π-electrons or n-electrons, can absorbed photons at specific wavelength to have their valence electrons promoted to a more energetic molecular orbital [70].

In Diffuse reflectance UV-vis spectroscopy (DRUV), photons are captured by an integrating sphere after hitting the powder and scattering on the surface of its grains. This allows a reading of the absorbance measurement without having the light reflected from the sample surface. It is a common method to measure opaque samples that absorb too strongly to be measured in transmission.

Samples are prepared using a Harrick Praying Mantis™ Sampling kit (DRPSAP); the powder is placed in a cylindrical sample holder, packed and sleeked to obtain a smooth surface. After running a Spectralon® blank from

the kit, the sample can be inserted in the chamber for analysis. This is carried out with a Shimadzu UV-3600 Plus series spectrometer with a deuterium lamp for the ultraviolet range. Wavelength range is set to 200 nm to 800 nm, with sampling interval of 0.5 nm. The Shimadzu's proprietary software UVProbe 2.62 is used.

4.2.2 Infrared spectroscopy FTIR-ATR

Fourier Transform Infrared spectroscopy – Attenuated Total Reflectance (FTIR-ATR) is the measurement of the decrease in intensity of the radiation passing through a sample, as a function of the wavelength. Infrared spectroscopy gives information about the surface chemical environment. This technique is used to determine the nature of the species on the sample because infrared waves have enough energy to stimulate molecular vibrations.

In practice, an optical beam will undergo several reflections at the interface between a solid sample and a parallelepiped diamond that is transparent in infrared but with a very high reflection index. This beam will undergo total reflection at the crystal-sample interface and will then be detected. During the reflection of the ray, it is possible that a wave penetrates the solid being analyzed, this wave is called evanescent wave. The consequence of this phenomenon is the attenuation of the reflected wave.

The device used is a Bruker Equinox IFS55. The IR detection is made by a DTGS dielectric detector. The spectrum is recorded at room temperature for wave numbers between 4000 cm^{-1} and 600 cm^{-1}. The spectra are acquired by an accumulation of 100 scans with a spatial resolution of 4 cm^{-1} with air as background. The software used is OPUS.

4.2.3 X-ray Diffractometry (XRD)

X-Ray diffractometry relies on the elastic diffusion of photons through the crystalline planes of the sample. It is a non-destructive method, XRD allows determining the atomic and molecular structure of a crystal.

The Bragg's law is utilized in this technique to identify crystalline phases, with "d" representing the distance between two atomic planes in nanometers, "n" being a multiple of the X-ray wavelength "λ" in nanometers, and "θ" representing the angle of diffraction in radians. By deducing the

distance between atomic planes, it is possible to determine the composition or crystalline structure.

$$2d \sin\theta = n\lambda \quad (2)$$

Lattice parameter (a_0) represent the distance between two pores center. It can be calculated from d_{100}, the interplanar spacings of the reflections peak (100) using the equation 3. The wall thickness is acquired by subtracting from a_0 the pore diameter computed from N_2 physisorption [126].

$$a_0 = \frac{2 * d_{100}}{\sqrt{3}} \quad (3)$$

In practice, the sample is sprinkled on a sample holder coated with Nivea cream, which is then inserted in a Bruker-D8 Advance diffractometer with a Bragg-Brentano geometry. A copper anode under 40 kV and 30 mA produces the X-ray radiation with a Kα wavelength of 1.54 Å. The Bruker detector was using a LynxEye XE-T technology and was recording values obtained with a 2θ value between 1° and 5° with 2θ increments of 0.0074° and 3 seconds per step. The diffractograms obtained were analyzed with the DIFFRAC.EVA software.

4.2.4 Nitrogen physisorption

Nitrogen physisorption is used to characterize the textural properties of the catalyst such as specific surface area, porosity or pore width.

Approximately 50 mg of PMOs is precisely weighted for analysis and degassed under vacuum at 150 °C during minimum 12h using a Micromeritics VacPrep 061. The samples are weighted again after degassing. Nitrogen physisorption isotherms are measured at 77K in a liquid nitrogen bath using a Micromeritics TriStar 3000.

4.2.5 Inductively coupled plasma-atomic emission spectroscopy (ICP-AES)

This analysis gives the elemental content of a sample in mass percentage. More specifically rhodium was analyzed. The device used is a Thermo Scientific ICP 6500. The calcined sample were solubilized by sodium peroxide fusion in carbon crucibles. Plasma is generated with inductive currents and produces excited atoms and ions, which in turn emit electromagnetic radiations at wavelengths characteristic of a particular element.

The analysis was carried out by the Mineral & Organic Chemical Analysis (MOCA) platform of the Earth and Life Institute (ELI) at UCLouvain.

4.2.6 X-ray Photoelectron Spectroscopy (XPS)

XPS is used to monitor the surface chemistry of solid materials. In XPS, the sample surface is irradiated by monochromatic X-ray and the emitted photoelectrons are detected. These emitted photoelectrons have a specific kinetic energy depending on their binding energy. They are filtered and analyzed to deduce this binding energy, as each element produces a set of unique peaks in the photoelectron spectrum.

In this work, an SSX 100/206 Photoelectrons Spectrometer from Surface Science Instruments, equipped with an AI RX monochromatic and micro-focused source, was used. The pressure inside the analysis chamber is about 10^{-6} Pa, the analysis angle is 55 ° and the pass energy is fixed at 150 eV. Data was processed with CasaXPS from Casa Software Ltd, UK. To calibrate the binding energy scale, the C 1s peak, C-C bond component has been set at 284.8 eV. Spectra are then decomposed, and molar fractions can be obtained based on the acquisition parameters and sensitivity factors provided by the manufacturer.

4.2.7 Transmission electron microscopy (TEM)

In TEM, which uses transmitted and diffracted electrons to create an image. An electron beam of high energy and high intensity passes through a sample. The transmitted electron electrons form a two-dimensional projection of the sample.

Two-dimensional transmission electron microscopy (2D TEM) images were taken using a JEOL JEM-1010 TEM instrument operated at 100kV without spherical aberration (Cs) correction. All the TEM images were carried out by the Center for Ordered Materials, Organometallics & Catalysis (COMOC) at UGent.

4.3 Catalytic testing

4.3.1 Standard NADH regeneration

The reaction was conducted in a 10 mL round bottom flask loaded with in 1.5 mL of a sodium phosphate (0.10M, pH 7.0) buffer suspension containing 0.10M formate, NAD+ 1.5 mM, and 1 mg/mL of $[Cp^*RhCl_2]_2$ or 2 mg/mL of Rh@Bpy-PMO as a catalyst at a temperature between 22°C and 50°C. One reaction medium sample of 500 μL was collected and filtered to monitor the reaction by UV-vis spectroscopy. The yield of NADH was estimated by monitoring the absorbance at 340 nm and using the extinction coefficient of NADH, $\varepsilon_{340\ nm}$ = 6300 $M^{-1}cm^{-1}$.

4.3.2 Standard ketone reduction test

The reactions were carried out in a 0.10 M (pH 7.0) sodium phosphate buffer solution (1.5 mL) containing 0.1 M formate, NADH (5 mM), HLADH (3U) or 10 mg of Bpy-PMO-HLADH and 4-phenyl-2-butanone (5 mM) as the substrate. 500 µL of the reaction mixture was subsequently collected and filtered. Phenol (20 µL) was added as internal standard before the extraction with ethyl acetate (1000 μL). The organic phase was analyzed by gas chromatography.

4.3.3 Ketone reduction test with NADH regneration

The reactions were carried out in a 0.10 M (pH 7.0) sodium phosphate buffer solution (1.5 mL) containing 0.1 M formate, NAD+ (1.5 mM), HLADH (3U) or 10 mg of Bpy-PMO-HLADH and 4-phenyl-2-butanone (5 mM) as the substrate. NADH regeneration is achieved by 2 mg/mL of Rh@Bpy-PMO or 1 mg/mL of $[Cp^*RhCl_2]_2$ as catalyst. 500 µL of the reaction mixture was subsequently collected and filtered. Phenol (20 µL) was added as internal standard before the extraction with ethyl acetate (1000 μL). The organic phase was analyzed by gas chromatography.

4.3.4 Ketone reduction test by the hybrid catalyst

The reactions were carried out in a 0.10 M (pH 7.0) sodium phosphate buffer solution (1.5 mL) containing 0.1 M formate, NAD+ (1.5 mM), 10 mg of Rh@Bpy-PMO-HLADH and 4-phenyl-2-butanone (5 mM) as the substrate. 500

µL of the reaction mixture was subsequently collected and filtered. Phenol (20 µL) was added as internal standard before the extraction with ethyl acetate (1000 μL). The organic phase was analyzed by gas chromatography.

4.3.5 Rh@Bpy-PMO catalyst recycling test

After a standard test run, the medium is filtered, the solid is then washed 3 times with 15 mL of PBS pH 7 and dried under vacuum at 25 °C. The reaction is carried out in the same conditions as a standard NADH regeneration test adjusting the amount of reagents and standard with respect to the remaining mass of powder.

4.3.6 Rh@Bpy-PMO PBON adsorption

The amount of PBON adsorbed on the surface of the catalyst was evaluated by adding 0.0224g of powder to 8mL of 0.10 M (pH 7.0) of sodium phosphate buffer solution containing 4 mL PBON (0.08 M). 500 µL of the reaction mixture was subsequently collected and filtered. Phenol (20 µL) was added as internal standard before the extraction with ethyl acetate (1000 μL). The organic phase was analyzed by gas chromatography.

4.3.7 Rh@Bpy-PMO specificity

The reactions were carried out in 0.1 M sodium phosphate buffer solution (pH 7) with 2.7 mM of PBON or 5.1 mM of PBOL and 2 mg/mL of Rh@Bpy-PMO. 500 µL of the reaction mixture was subsequently collected and filtered. Phenol (20 µL) was added as internal standard before the extraction with ethyl acetate (1000 μL). The organic phase was analyzed by gas chromatography.

4.3.8 Gas chromatography (GC)

GC analysis of the sample was carried out on a Bruker SCION 456-GC. The system was equipped with an Agilent DB-5 column (30 m x 0.32 mm x 1 µm), a split/splitless injector ratio of 1/20 set at a temperature of 250°C and an automatic sampler injecting 10 µL. The detector used was an FID detector at a temperature of 250°C using 300 mL.min^{-1} of air, 30 mL.min^{-1} of hydrogen and 25 mL.min^{-1} of helium as make-up gas.

The head of the column was kept at a constant pressure of 10 psi. The oven followed a temperature profile shown in Figure 22. The program starts at 70°C and then rises to 100°C in 3 minutes (ramp rate of 10 K/min). After that, the temperature is increased to 180°C after 7 minutes and kept constant for 4 minutes.

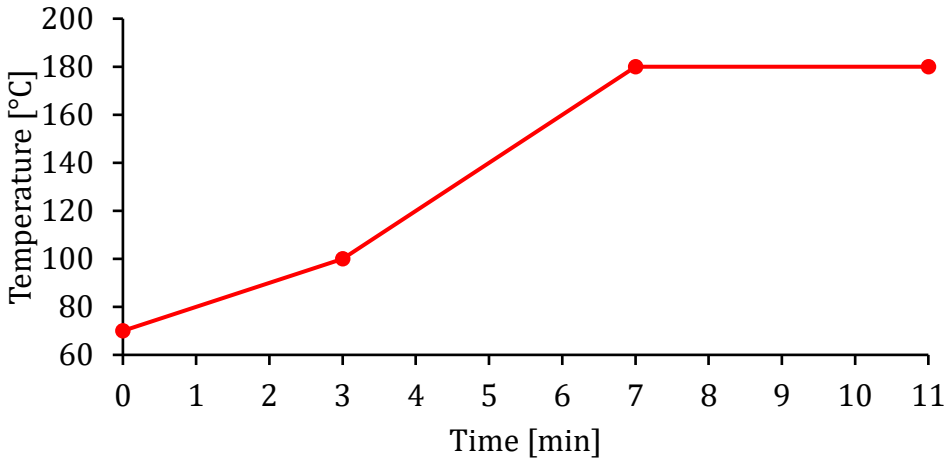

Figure 22: Temperature profile of the GC oven during an analysis

To quantify the concentration of PBON and PBOL in ethyl acetate, two calibrations curves were produced. First, a stock solution of PBS at pH 7 and phenol was produced. The solution was composed of 10.44 g of K_2HPO_4, 5.44 g KH_2PO_4 in 1 L of deionized water. Then, 50 µL of 4-phenyl-2-butanone in 50 mL of PBS and 100 µL of 4-phenyl-2-butanol in 100 mL of PBS produce stocks solutions. Then 5 intermediary solutions with respectively 1, 5, 10, 15 and 20 mL of the 4-phenyl-2-butanone were diluted with PBS to reach 20 mL. The same procedure was achieved for the 4-phenyl-2-butanol with 2 µL, 150 µL, 400 µL, 700 µL, 10 mL and 20 mL. Finally, 500 µL of each intermediary solution were extracted with 1000 µL of ethyl acetate and inject in GC. In appendix (Figure S I), one can find the calibrations curves.

The ratio of the concentration and the area gives a linear relationship:

$$\frac{[PBON]}{[phenol]} = \frac{CR_{PBON}}{CR_{phenol}} * \frac{Area_{PBON}}{Area_{phenol}}$$

$$\frac{[PBOL]}{[phenol]} = \frac{CR_{PBOL}}{CR_{phenol}} * \frac{Area_{PBOL}}{Area_{phenol}}$$

With CR the response coefficient. With the slope of the calibration curves, the CR ratio can be found. The R^2 of both regressions being above 0.99, the confidence of this value is high.

The area of the 2 organics molecules and of the internal standard are measured and the concentration of phenol is known, so the concentration of PBON and PBOL can be calculated in mol/L^{-1} with theses equations:

$$[PBON] = 0.651 * \frac{Area_{PBON}}{Area_{phenol}} * [\text{phenol}]$$

$$[PBOL] = 0.5532 * \frac{Area_{PBOL}}{Area_{phenol}} * [\text{phenol}]$$

Chiral GC analysis was carried out on a Shimadzu GC-2014. The system was equipped with an CPChirasil DEX (25 m x 0.25 mm x 0.25 µm), a split/splitless injector ratio 1/10 set a temperature of 220°C and an automatic sampler injecting 1µL. The detector used was an FID detector at a temperature of 250°C using 300 mL/min of air, 30 mL/min of hydrogen and 25 mL/min of helium as make-up gas. The linear velocity was 35 cm/s. The oven was kept at constant temperature of 110°C for 15 minutes. The retention time for the (S)-4-phenyl-2-butanol was 15.2 min and for (R)-4-phenyl-2-butanol was 15.7 min.

4.3.9 Calculation of catalytic performance

The yield after t hours of reaction was calculated using the following equation 4:

$$Y_y = 100 * \frac{n_{x,t} - n_{x,0}}{n_{x,0}} \quad (4)$$

With Y_y the yield of the molecule y being calculated in %, $n_{y,0}$ and $n_{y,t}$ being the molar quantities of y in the whole system at the start and after t hours of reaction and $n_{x,0}$ being the molar quantities of x in the whole system at the start of reaction.

The conversion of x after t hours of reaction was calculated using equation 5:

$$C_x = 100 * \frac{n_{x,0} - n_{x,t}}{n_{x,0}} \quad (5)$$

With C_x the conversion of x calculated in %, $n_{x,0}$ and $n_{x,t}$ being the molar quantities of x in the whole system at the start and after t hours of reaction.

The selectivity toward the molecule x is calculated using equation 6:

$$S_x = 100 * \frac{Y_y}{C_x} \quad (6)$$

With S_x the selectivity in %, Y_y the yield and C_x the conversion expressed in %.

The productivity was calculated using the following equation 7:

$$Productivity = \frac{n_x}{m_{cata} * t} \quad (7)$$

With the productivity in µmol/(mg_{cata}*h), n_x the number of moles of x in µmole, m_{cata} the mass of catalyst in mg and t the time of reaction in hour.

Results and discussion

5. RESULTS AND DISCUSSION

This section is organized following the strategy of this study. First, the ketone reduction catalyzed by HLADH as free enzyme tests will be presented. Afterwards, the regeneration of NADH by rhodium catalyst will be analyzed and its combination with free HLADH. Then, the cascade is investigated with two separate catalysts. Finally, the cascade with the hybrid catalyst is studied.

5.1 HLADH-CATALYZED KETONE REDUCTION

5.1.1 Temperature range

Figure 23 illustrates the conversion, yield, selectivity, and productivity after 5h for the reduction of PBON to PBOL using HLADH as a free enzyme (in the homogeneous phase) at different temperatures with NADH as the electron donor.

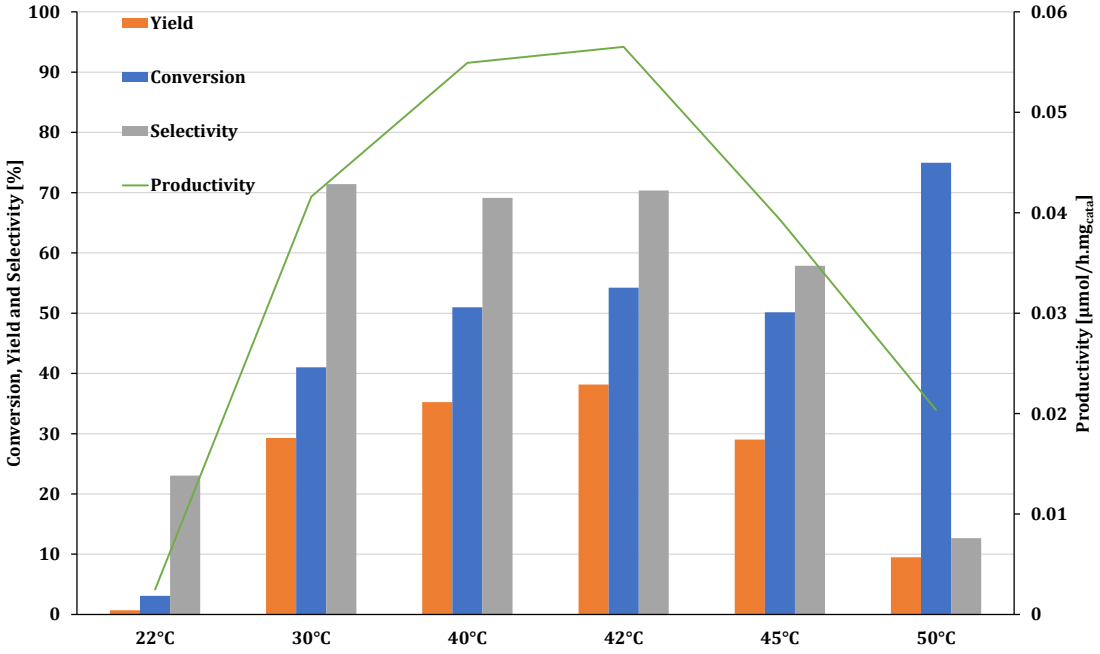

Figure 23: Conversion, selectivity, yield and productivity for the reduction of PBON into PBOL by free HLADH after 5h for different temperatures.

It can be observed that the maximum yield and productivity are achieved at 42°C, while the highest conversion is at 50°C and the better selectivity at 30°C. The enzyme has a temperature range (30°C - 45°C) within which it demonstrates significant catalytic activity. The temperature compromise is at

42°C. Below this temperature (40°C) the conversion and productivity decrease and at higher temperature (50°C) the conversion is high, but the selectivity and the productivity are low. The temperature for all the reduction tests will be done at a temperature around the 42°C.

5.1.2 Dependency of NADH for PBON reduction

HLADH uses NADH as a cofactor, which acts as the ultimate reducing agent. To illustrate the fact that the action of the enzyme is NADH-dependent, we performed a test in the presence of NAD^+ instead of NADH (Figure 24). This led to a substantial decrease in the conversion of PBON and virtually no production of PBOL. Thus, NADH must be supplied in sufficient amounts to run the ketone reduction or regenerated (see 5.3.2).

Another experiment was conducted to highlight the significance of having a stoichiometric amount of NADH. This involved performing a standard test with a lack of NADH. The concentration of NADH for the standard test was set at 5 mM and at 1mM for the low NADH concentration test while the concentration of PBON was 5mM for both tests. In theory, there is enough NADH to achieved 100% of conversion in a standard test but as it can be seen after 5h, the conversion is only at 50%. Since the reduction of PBON to PBOL is an equilibrium reaction, achieving a 100% conversion is impossible. The conversion and yield observed in the "Low NADH" test are approximately 5 times lower than those of the standard test. These results were expected due to the NADH concentration being 5 times lower.

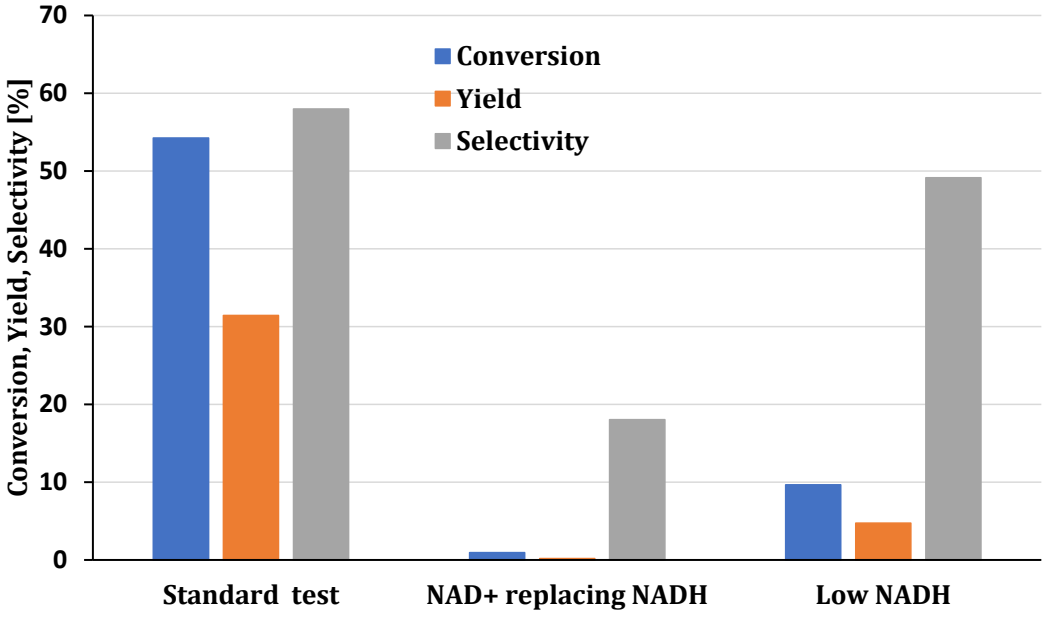

Figure 24: Conversion, yield and selectivity for the standard test, a standard test with NAD+ instead NADH and a standard test with 1mM of NADH instead of 5mM by HLADH after 5h at 42°C.

5.1.3 Effect of formate

Figure 25 (green frame) presents the comparison between the result from the standard test and the same test with the addition of formate. The goal of this test is to be sure that the formate does not have any influence on the ketone reduction because it will serve as electron donor for the NADH regeneration in the cascade. The results demonstrate no significant changes after the addition of formate.

5.1.4 Replacement of NADH by formate

The dependency of NADH as an electron donor has already been established, but the replacement of NADH with another electron donor has not been attempted yet. Figure 25 (purple frame) illustrates a comparison between a standard test and a standard test where formate is used instead of NADH as the electron donor. in such case, there was no production of PBOL after 5 hours. This shows that formate cannot serve as the electron donor for the enzymatic reduction of PBON to PBOL.

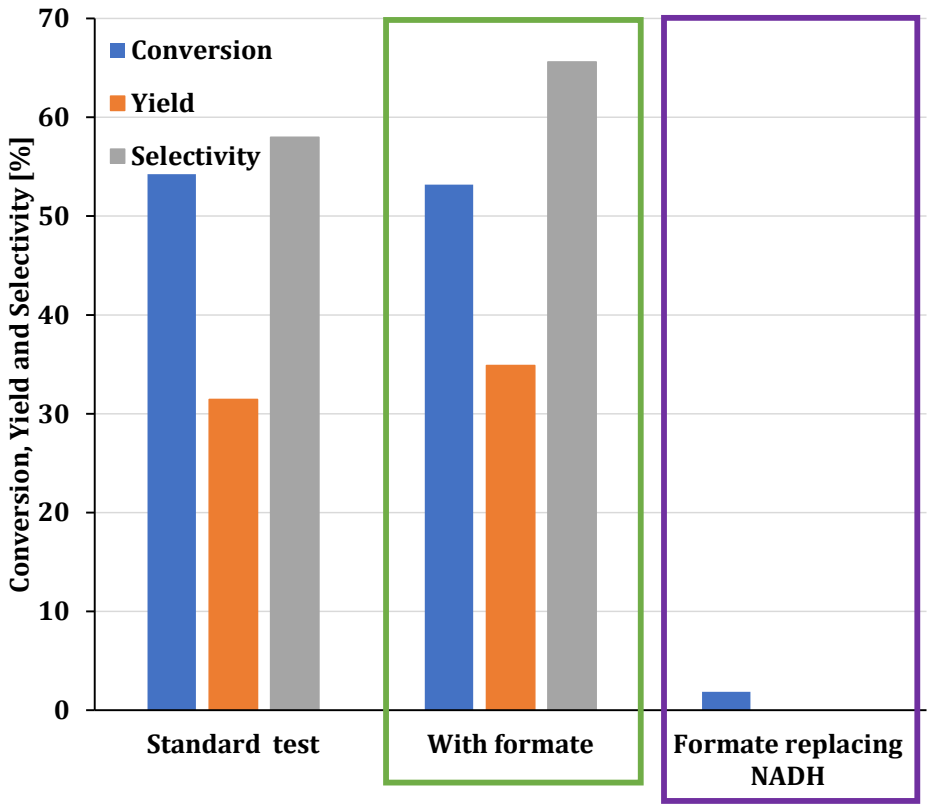

Figure 25: Conversion, yield and selectivity for the standard reduction test, a standard test with the addition of formate and a standard test with the replacement of NADH by formate as electron donor by HLADH after 5h at 42°C.

5.1.5 Enantioselectivity of the HLADH-catalyzed reduction of ketone

Chiral gas chromatography was used to verify the enantioselectivity of the reduction. Figure 26 shows that the reduction of PBON by free HLADH (S-enantioselective [80]) led only to the formation of S-PBOL and no R-PBOL (chiral chromatography of a standard racemic mixture was used as a reference).

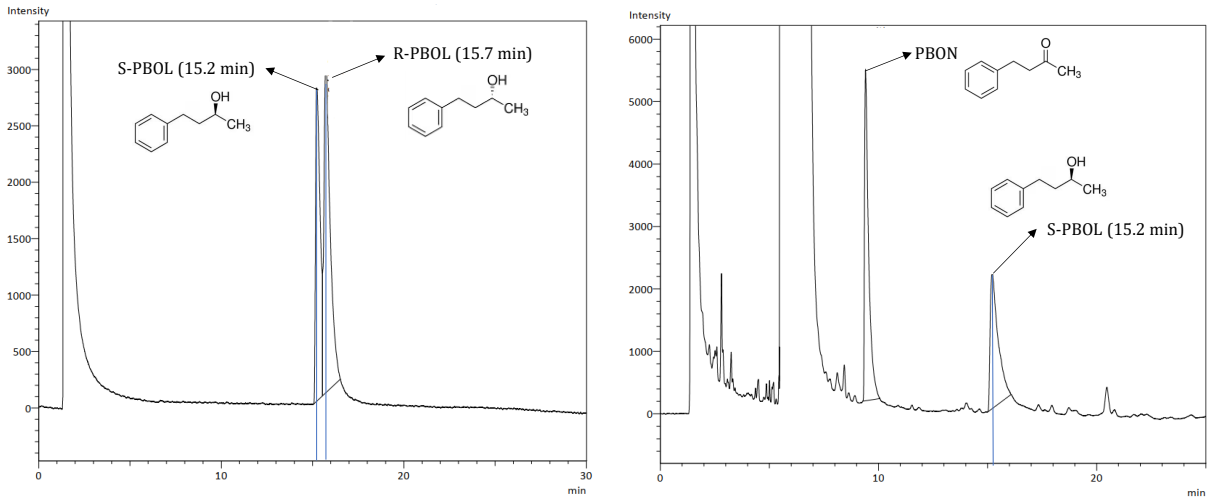

Figure 26: Chiral GC chromatograms, on the left of a PBOL racemic mixture and on the right of the PBON reduction by HLADH as a free catalyst after 5h at 42°C.

5.1.6 Overall adjusted carbon balance for the screening reactions

In our case, in GC, only PBON and PBOL can be detected (in addition to intern standard). However, it is possible that CO2 (without the regeneration of NADH) or other compounds that cannot be detected by GC could be generated during the reaction. A reliable indicator is to divide the moles of PBON and PBOL quantified by GC after the 5-hour test by the initial number of moles quantified by GC at the start of the test (t_0). If the ratio is close to 100%, we can deduce the absence of a side reaction. This metric is referred as the "Adjusted carbon balance" since it exclusively considers PBON and PBOL, omitting NADH, NAD+, or formate. The equation for this calculation is presented in Equation 8:

$$Adjusted\ carbon\ balance = 100 * \frac{n_{PBON,5h} + n_{PBOL,5h}}{n_{PBON,t0} + n_{PBON,t0}} \quad (8)$$

Figure 27 shows the adjusted carbon balance across all preceding tests. It is evident that there is a reduction for the standard test, the formate test, and the low NADH test. The declines may arise from experimental inaccuracies, such as inadequate extraction or pipetting. However, it appears more plausible that the generation of unknown molecules is accountable for this phenomenon, as it would imply that the experimental errors persist consistently across all the tests. This discovery underscores the potential formation of undetected byproducts, which in turn affects the reaction's selectivity.

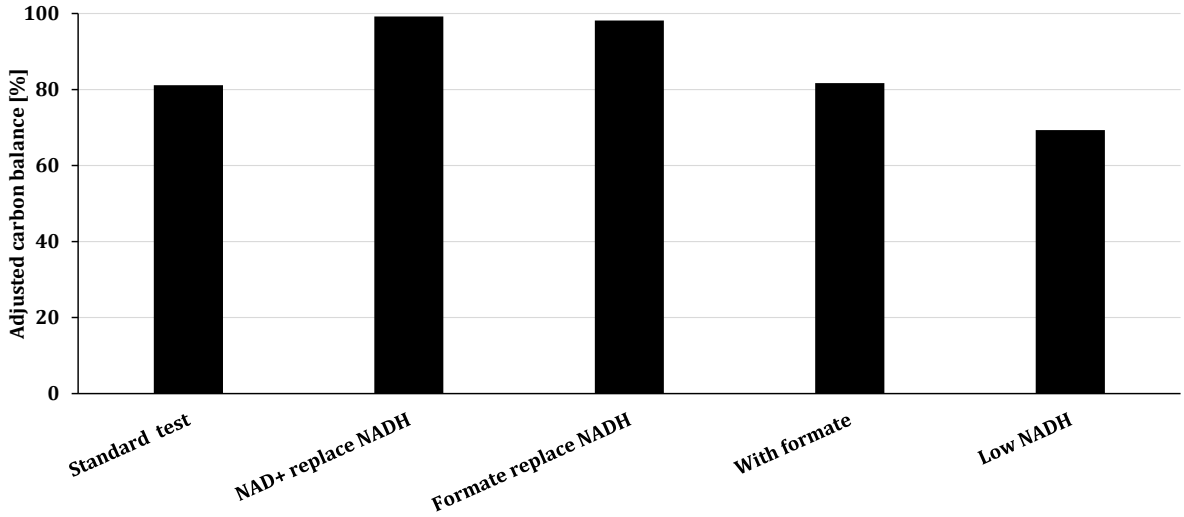

Figure 27: Adjusted carbon balance for the screening reactions after 5h at 42°C.

5.1.7 Discussion on HLADH-CATALYZED KETONE REDUCTION

The results of the HLADH-catalyzed reduction of PBON indicate that the "optimal" temperature for this reaction is 42°C. Increasing the temperature can lead to enzyme deactivation, likely due to denaturation. The deactivation of HLADH can explain the decrease in selectivity observed at 50°C. These preliminary investigations also emphasize the importance of supplying NADH in a stoichiometric amount since it is consumed in the reaction. When it is not supplied or is supplied in insufficient quantities, the reaction either slows down or does not proceed at all. This result underlines the significance of designing a system that includes the regeneration of NADH. The replacement of NADH by formate demonstrates the specificity of HLADH for NADH as an electron donor. Additionally, the addition of formate to the reaction medium, which will be necessary when implementing the cascade reaction, does not

affect the enzyme's performance. The chiral chromatograms obtained from GC analysis confirm that the enzyme exclusively produces S-PBOL, which justifies its application as an enantioselective catalyst. Furthermore, by analyzing the results in conjunction with the adjusted carbon balance, it is possible to gather additional information about the reaction. It appears that HLADH not only produces PBOL but also other chemicals that are not detected in GC analysis. These could potentially include CO_2 or charged molecules that cannot be extracted in ethyl acetate.

5.2 NADH regeneration with the (PMO-immobilized) Rh complex

5.2.1 Temperature range of $[Cp^*RhCl_2]_2$

In the NADH regeneration using $[Cp^*RhCl_2]_2$, yield and productivity increase as the temperature increases (Figure 28). This augmentation highlights the enhanced performance of the rhodium complex at higher temperatures. Considering the sensitivity of enzymes to high temperatures, and in particular the results presented for HLADH (Figure 23), temperatures above 50°C were not investigated.

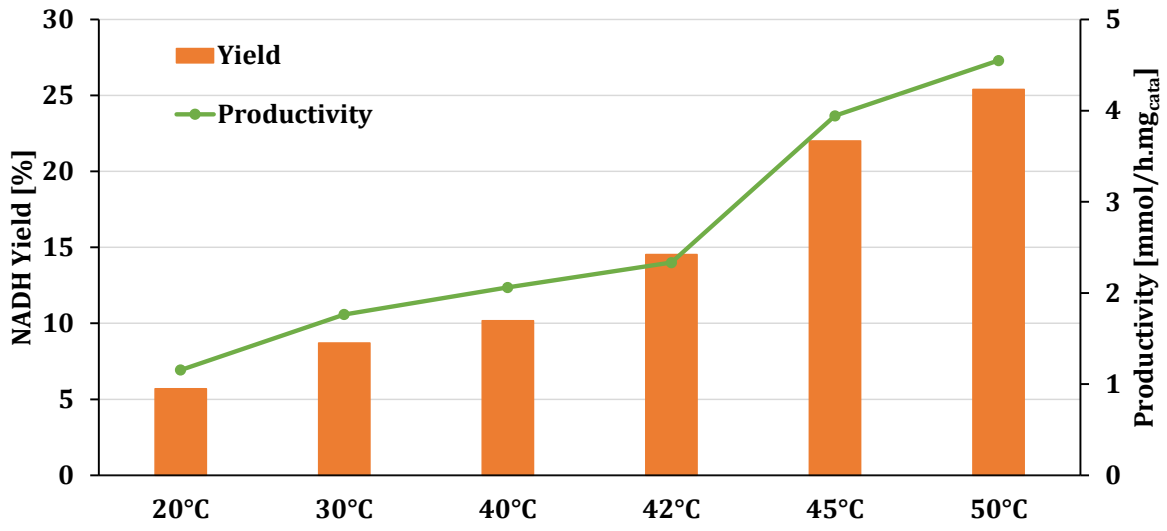

Figure 28: Yield and productivity for the NADH regeneration by the $[Cp^*RhCl_2]_2$ after 1h for different temperatures

5.2.2 Characterization of BPY-PMO and Rh@Bpy-PMO

NITROGEN PHYSISORPTION

Figure 29 depicts the physisorption isotherms obtained for Bpy-PMO and Rh@Bpy-PMO. The textural properties obtained from N_2 physisorption analysis are presented in Table 3. Both isotherms display a type IV pattern, which is indicative of mesoporous materials with uniform pores. The observed hysteresis is of H1 type, suggesting that the materials possess well-ordered mesoporous structures with uniformly cylindrical pores. Although, the overall shape of the isotherm remains consistent, a downward shift is noticeable after the addition of rhodium.

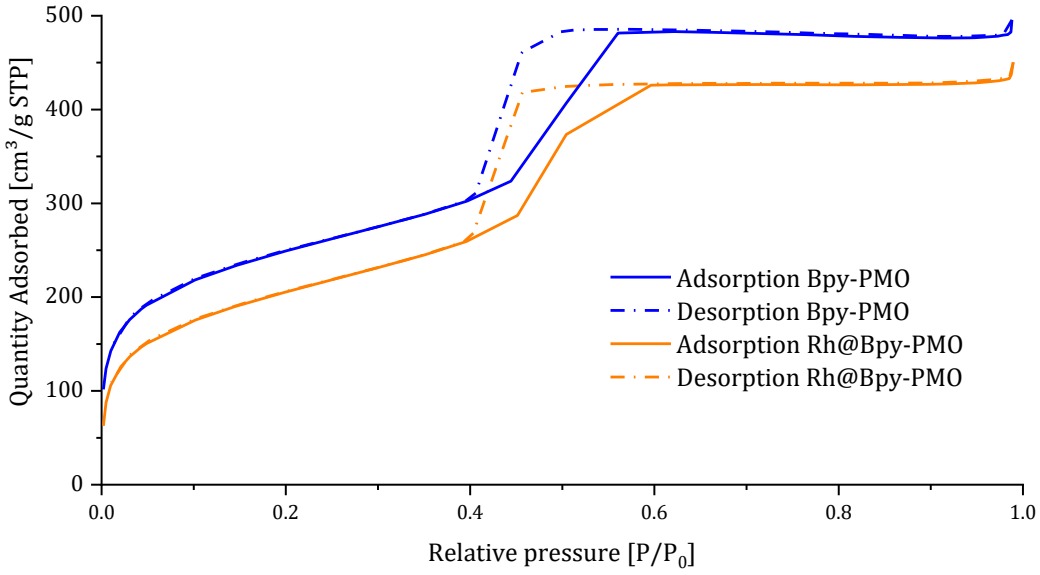

Figure 29: N_2 Adsorption and desorption isotherms of Bpy-PMO and Rh@Bpy-PMO.

Table 3: Summary of the textural properties of Bpy-PMO and Rh@Bpy-PMO.

Sample	Specific surface area [m^2/g]	t-Plot external surface area [m^2/g]	t-Plot micropore volume [cm^3/g]	Cumulative pore volume [cm^3/g]	t-plot BJH mesopore size [nm]
Bpy-PMO	870	290	0.30	0.56	3.4
Rh@Bpy-PMO	730	280	0.24	0.52	3.1

After the rhodium grafting, all the textural properties show a decrease, particularly the specific surface area, which decreases by approximately 16%. Regarding the pore size, a slight reduction from 3.4 nm to 3.1 nm is observed after loading the Rh complex. The lower specific surface area can be partially explained by the increase in the mass of the material after the addition of a nonporous rhodium complex. The denominator on the Y-axis changes, but not the numerator after adding the rhodium complex. If the decrease in specific surface area was solely due to this phenomenon, it would result in a reduction of only 6.4% with a theoretical loading of 6.8 mg for 100 mg of Bpy-PMO. The other explanation is related to the coating of the rhodium complex on the walls of the pores.

FT-IR

FT-IR analyses confirm the presence of Bpy within the Bpy-PMO (Figure 30). The peaks observed between 600 cm^{-1} and 1250 cm^{-1} are specific to the silica framework, particularly at 694 cm^{-1}, 917 cm^{-1}, 1030 cm^{-1}, and 1160 cm^{-1}, which correspond to Si-O symmetric bending, Si-OH stretching, Si-O stretching, and Si-C stretching respectively. Other noticeable bands especially at 1270 cm^{-1} and 1591 cm^{-1}, can be attributed to the vibration of C-N and C=C bonds in bipyridine moieties. Lastly, the broad band spanning from 3000 cm^{-1} to 3500 cm^{-1} corresponds to O-H stretching, while the C-H vibrations are observed around 2900 cm^{-1}. The IR spectrum of Rh@Bpy-PMO shows no significant difference after Rh grafting. IR spectrum of $[Cp^*RhCl_2]_2$, which exhibits a peak around 2900 cm^{-1} associated to C-H stretching and stretching two peaks corresponding to the CH3 around 3000 cm^{-1}. The bands at 1370 cm^{-1} and 1450 cm^{-1} correspond to the C-H bending. These peaks are absent in the Rh@Bpy-PMO curve. The C-H corresponding to the pentadiene is invisible on the Rh@Bpy-PMO spectra because the quantity of rhodium complex bind on the PMO is low. The stretching vibrations in rhodium-pyridine would occur between 150 cm^{-1} – 250 cm^{-1} but the spectra were only recorded between 4000 cm^{-1} and 600 cm^{-1} [127].

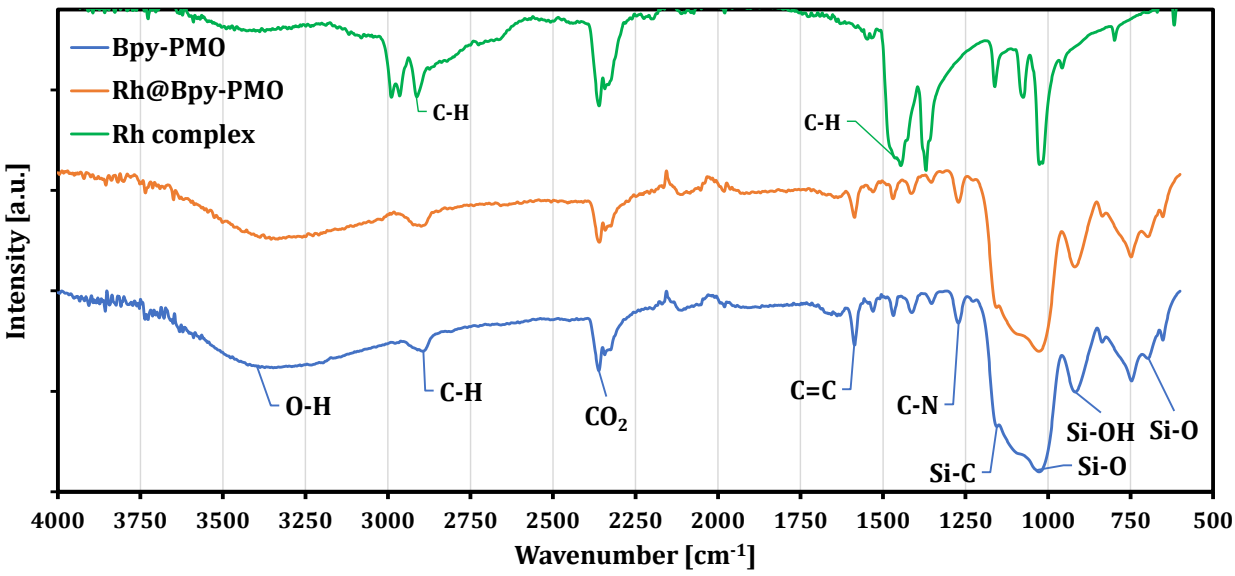

Figure 30: FT-IR spectra of $[Cp^*RhCl_2]_2$, Rh@Bpy-PMO and Bpy-PMO between 4000 cm^{-1} - 600 cm^{-1}

XRD AND TEM

The X-ray diffractogram of Bpy-PMO and Rh@Bpy-PMO, shown in Figure 31, does not display any significant peak within the 2θ angle range of 5° to 80°. Normally, some peaks need to appear demonstrating molecular-scale periodicity of bipyridine and silica moieties in the pore walls (Figure S II) [96], [128], [129].

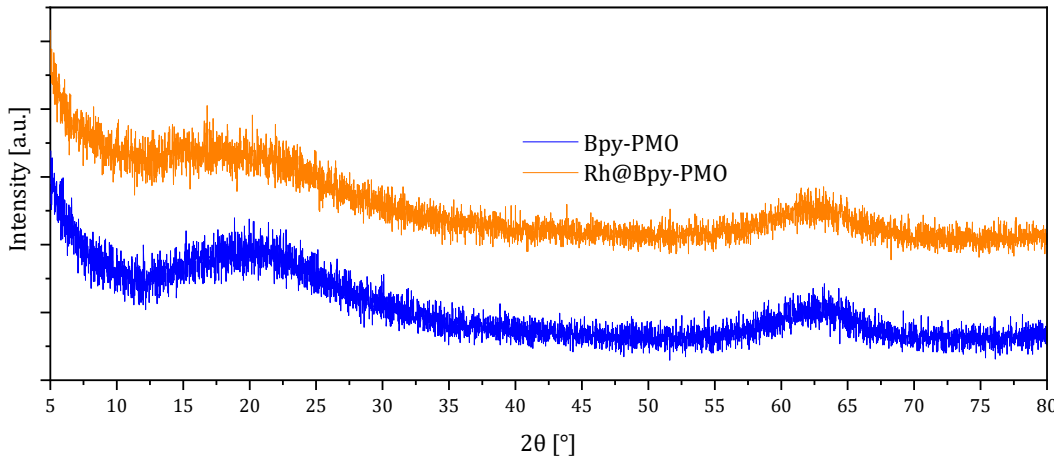

Figure 31: Powder XRD patterns in the 2θ region of 5°-80° of Rh@Bpy-PMO and Bpy-PMO

Figure 32 illustrates the XRD patterns of Bpy-PMO and Rh@Bpy-PMO at low angle values (1°-5°). The diffractograms exhibit three distinct diffractions peaks at 2θ = 1.4°, 2.36°, and 2.72°, which correspond to the (100), (110), and (200) reflection planes of the 2D hexagonal lattice in Bpy-PMO.

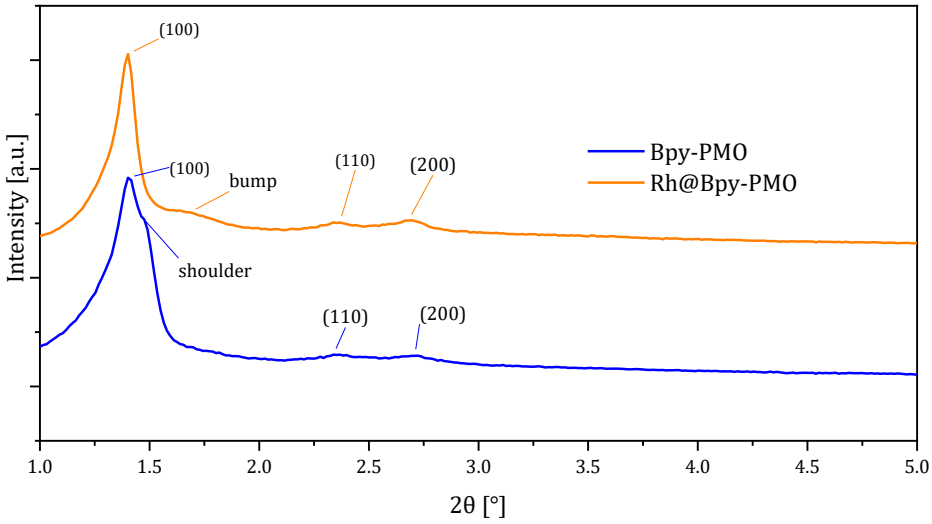

Figure 32: Powder XRD patterns in the 2θ region of 1°- 5° of Rh@Bpy-PMO and Bpy-PMO

Figure 33 is the representation of the reflection planes of the PMOs, the corresponding d-spacing and a_0. The d-spacing corresponds to the distance between adjacent reflection planes. On the other hand, a_0 represents the distance between the centers of two adjacent pores within the PMO material.

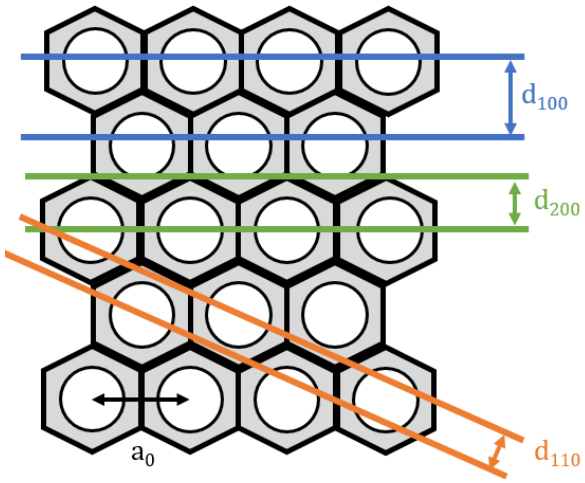

Figure 33: Reflections planes and lattice parameter a_0 for PMO

The structure of the material remains intact after grafting, as evidenced by the presence of the same three peaks at the same diffraction angles. However, there are slight changes observed, the suppression of a hump at 1.4° and the emergence of a bump at 1.7°. The hump could be attributed to the presence of an amorphous phase. The small bump can be the shift of the amorphous phase to 1.7°, although identifying these specific planes proved challenging.

Table 4 displays the values of a_0, wall thickness and the d-spacing for all the reflection planes for the PMOs. The a_0, and the d-spacing values remain unchanged. This confirms the unchanged structure of the PMO after the grafting of the rhodium complex. The only parameter that exhibits a change is the wall thickness. This change was expected because the pore wall is coated with the complex, so the wall thickness is increased, and the pore diameter decreases.

Table 4: Structural properties of Bpy-PMO and Rh@Bpy-PMO

Sample	a_0 [nm]	Wall thickness [1] [nm]	d_{100} [nm]	d_{110} [nm]	d_{200} [nm]
Bpy-PMO	7.2	3.8	6.2	3.7	3.2
Rh@Bpy-PMO	7.3	4.2	6.3	3.6	3.3

The TEM images in Figure 34 confirm the porous nature of Bpy-PMO. The pores are observed as lighter spots within the black particles. The particles size is around the 500 nm and the size of the pores can be roughly estimated to 3.5 nm. This confirms the pore size from the N_2 physisorption.

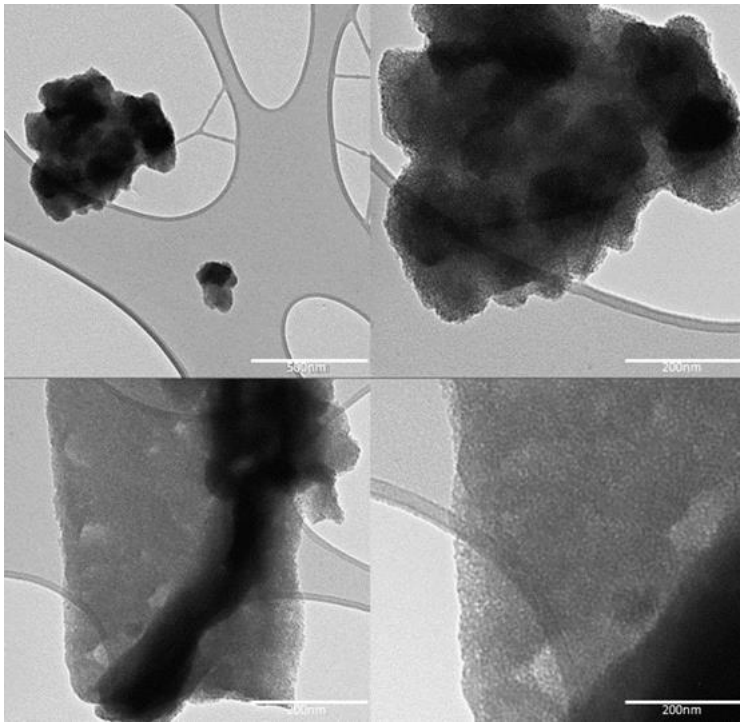

Figure 34: TEM images of Bpy-PMO

[1] Wall thickness = a_0 – BJH mesopore size

UV-VIS

DRUV analysis is used to confirm the presence of rhodium in the walls of Bpy-PMO. The DRUV spectrum in Figure 35 exhibits a decrease of the reflectance at 4 eV for the Bpy-PMO and Rh@Bpy-PMO, which is indicative of the presence of Bpy [130]. After the grafting of the rhodium there is another reflection band for the rhodium at 3 eV [80]. This reflectance band is the consequence of a metal to ligand charge transfer (MLCT)[2].

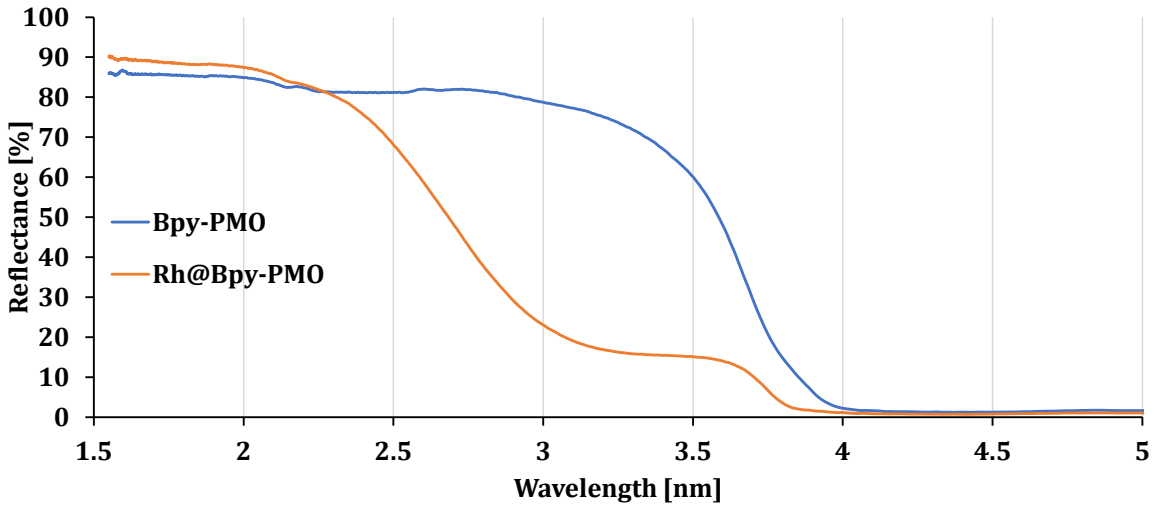

Figure 35: UV-vis diffuse reflectance spectra of Bpy-PMO and Rh@Bpy-PMO

XPS AND ICP-AES ANALYSIS

The surface composition was analyzed using XPS. Atomic concentrations were obtained, and atomic ratios were calculated as shown in Table 5. As expected, there are no significant change observed in the N/Si and O/Si ratios after Rh grafting. The Rh/N ratio indicates the amount of bipyridine occupied by rhodium. With a ratio of 0.1, there is approximately 1 rhodium for every 5 bipyridines (10 nitrogen atoms). The Cl/Rh ratio of 1.1, confirm the successful grafting of the complex, as there should be an equal amount of chlorine and rhodium in Rh@Bpy-PMO.

[2]MLCT is a process in which an electron is transferred from a metal center to a ligand in a coordination compound.

Table 5: XPS result for Bpy-PMO and Rh@Bpy-PMO

Bpy-PMO						
Atom [-]	O	N	C	Si	Rh	Cl
Atomic Concentration [mol_i/mol_{tot}]	44.9	2.8	35.5	16.8	/	/
Rh@Bpy-PMO						
Atom [-]	O	N	C	Si	Rh	Cl
Atomic Concentration [mol_i/mol_{tot}]	43.6	2.8	37.2	15.6	0.3	0.4

Atomic ratio [%]	Rh/N	Cl/Rh	N/Si	O/Si
Bpy-PMO	/	/	0.17	1.5
Rh@Bpy-PMO	0.1	1.1	0.2	1.6

There is a slight discrepancy between the rhodium loadings determined by XPS (0.21 $mmol_{Rh}/g_{Rh@Bpy\text{-}PMO}$)[3] and ICP-AES (0.17 $mmol_{Rh}/g_{Rh@Bpy\text{-}PMO}$) but this is within margin of error, the rhodium complex is well dispersed on the Bpy-PMO. The theoretical loading is 0.22 $mmol_{Rh}/g_{Rh@Bpy\text{-}PMO}$, thus, almost all the rhodium complexes are grafted onto the Bpy-PMO.

In conclusion, the characterization of Rh@Bpy-PMO demonstrates the successful grafting of the rhodium complex onto the Bpy-PMO without altering the structure of the PMO. The coating of the rhodium complex inside the pores leads to a marginal decrease in both the specific surface area and pore diameter.

5.2.3 Catalytic performance of Rh@Bpy-PMO

Regarding the NADH regeneration kinetics by Rh@Bpy-PMO (Figure 36), it demonstrates a significant yield within only 15 minutes, followed by a slight decrease. The figure also includes the results of a hot filtration test, where Rh@Bpy-PMO is removed after 30 minutes. The hot filtration test conducted in this study cannot serve as resistance test for the rhodium leaching because it was performed too late. If the experiment were to be repeated, the catalyst would need to be removed before the 15-minute mark.

[3] The rhodium loading in XPS was evaluated by calculating the total weight fraction of rhodium in the sample as mol_{Rh}/g_{tot}. Using the total weight of the sample, it is possible to calculate the total loading of rhodium in weight and then convert it to mmol/g

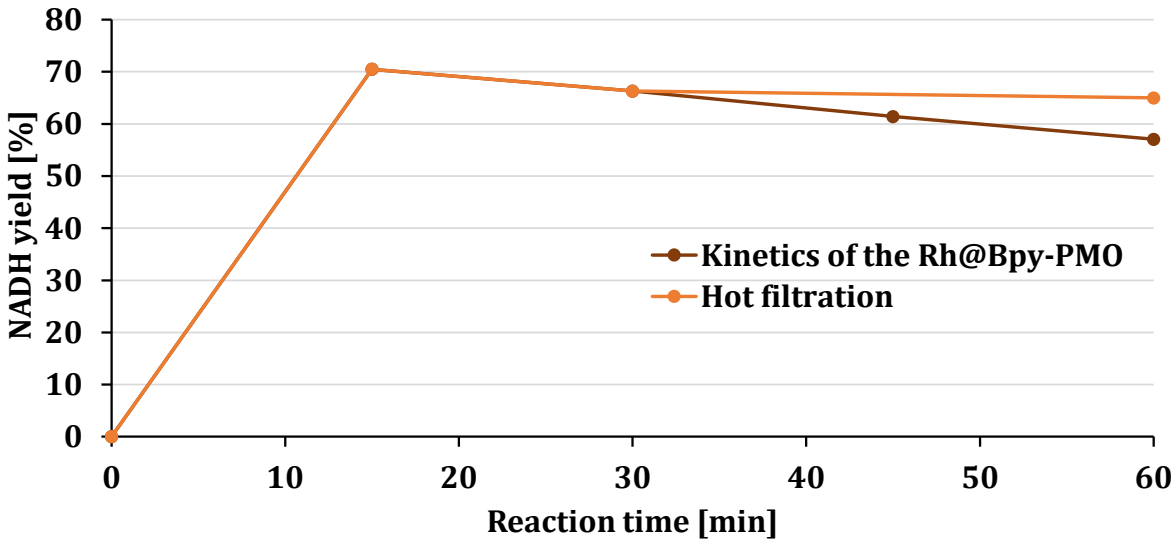

Figure 36: Kinetics of NADH regeneration by Rh@Bpy-PMO for 60 minutes and Rh@Bpy-PMO hot filtration test after 30 minutes at 42°C.

The recyclability of Rh@Bpy-PMO is presented in Figure 37 (see procedure of recycling test, section 4.3.5). There is a significant decrease in NADH yield after just one recycling, indicating a decline in the catalytic efficiency of the material with repeated use. The decrease of the activity can be due to catalyst deactivation or rhodium leaching.

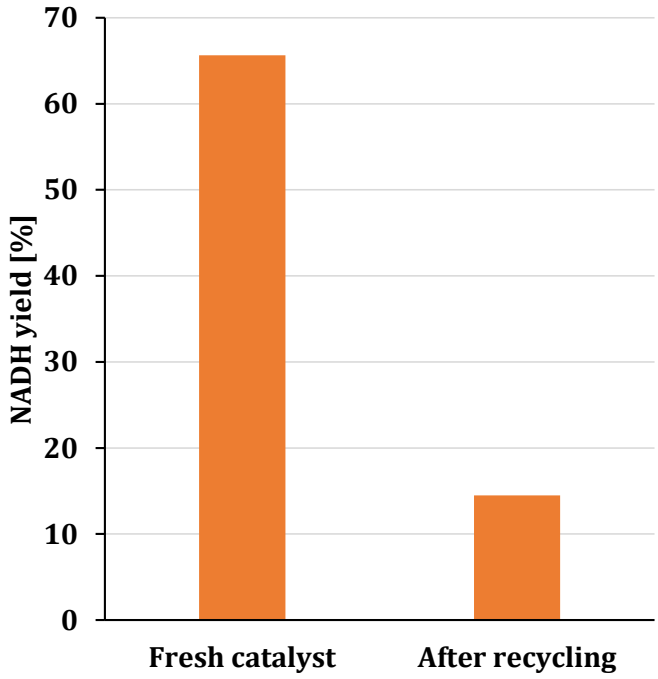

Figure 37: Recycling test of Rh@Bpy-PMO for NADH regeneration.

To evaluate the leaching resistance of Rh@Bpy-PMO, ICP-AES analysis of the medium after removing the catalyst was performed. This revealed that, after the NADH regeneration reaction, the catalyst did not lose any significant amount of rhodium with less than 0.05 mg/L of rhodium. This experiment demonstrates that the decrease of catalytic activity of Rh@Bpy-PMO after one recycling is not a consequence of rhodium leaching. During the catalytic test, a color change occurs Figure 38. This phenomenon was already observed for the NADH regeneration at higher temperatures (42°C and 45°C) by $[Cp^*RhCl_2]_2$. In the proposed mechanism (Figure 13 in section 1.4.4), the final step involves the cleavage of the covalent bond between NADH and rhodium. These color changes can be due to the blocking of NADH on the active site of the catalyst.

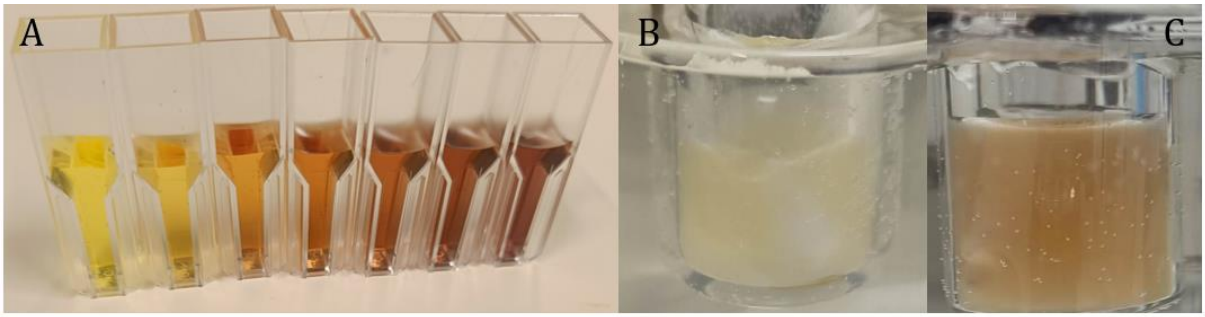

Figure 38: Color change during the regeneration of NADH: A) At 45°C with $[Cp^*RhCl_2]_2$ complex during 1h with 10 minutes intervals from left to the right, B) fresh Rh@Bpy-PMO and C) Rh@Bpy-PMO after NADH regeneration at 42°C during 1h

To confirm this hypothesis, Figure 39 presents the IR spectrum of NADH and the residue of Rh@Bpy-PMO. The Rh@Bpy-PMO residue is obtained by subtracting the IR spectrum of fresh Rh@Bpy-PMO from the IR spectrum of used Rh@Bpy-PMO. The similarity between these two spectra indicates either the blocking or the presence of residual NADH on the solid. The observed color change could also arise from the degradation of the rhodium complex due to ligand loss at elevated temperatures. However, it's noteworthy that the rhodium complex was maintained at 50°C for 1 hour without the presence of other compounds, and no color change was observed under these conditions.

Another plausible explanation for the color change could be the occurrence of multiple catalytic cycles, which might contribute to the complex's degradation. Nevertheless, it's important to highlight that during the cascade reaction with free HLADH (see 5.3.2), no color change was

observed, adding weight to the argument against the catalytic cycle-induced degradation.

Both of these experiments collectively provide evidence supporting the hypothesis of NADH blocking or the presence of residual NADH as potential causes for the observed changes in the system.

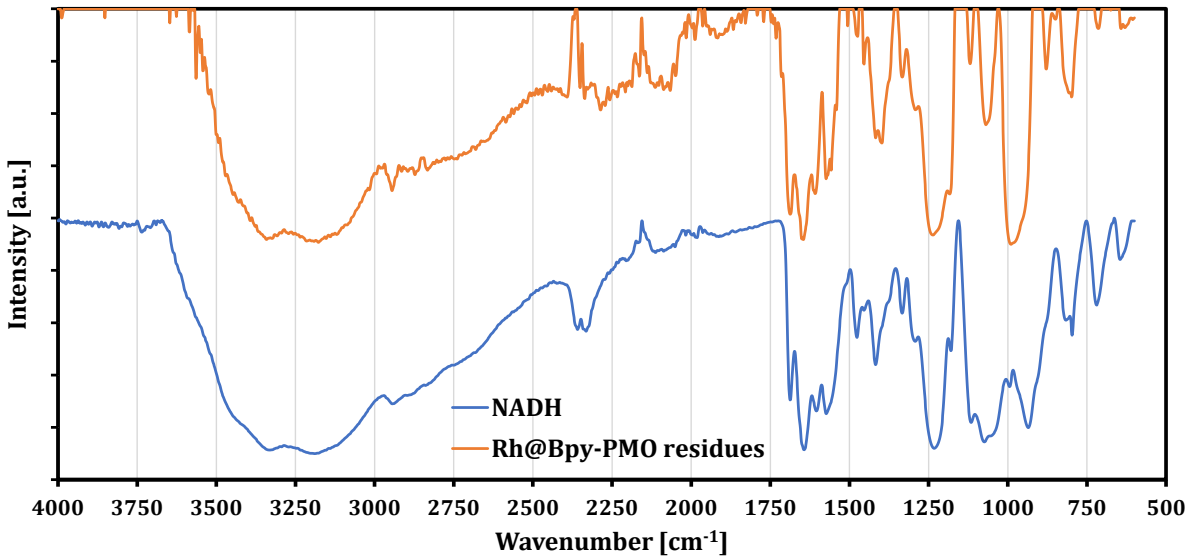

Figure 39: FT-IR spectrum of NADH and the Rh@Bpy-PMO residue between 4000 cm^{-1} and 600 cm^{-1}

During the NADH regeneration test using Rh@Bpy-PMO, the concentration of NADH decreases after 15 min (Figure 36). This phenomenon is consistent with previous observations regarding the issue of color change, suggesting that NADH may become trapped on the rhodium site. To evaluate the rate of NADH adsorption on rhodium, a kinetics study was conducted using Rh@Bpy-PMO as adsorbent (Figure S III). The result indicates that Rh@Bpy-PMO can adsorb $1.91*10^{-3}$ mol of NADH per gram of Rh@Bpy-PMO in 45 minutes. During the NADH regeneration test (45 minutes) by Rh@Bpy-PMO there is a decrease of $1.1*10^{-6}$ mol of NADH for 0.014g of Rh@Bpy-PMO. This represents a decrease of $8.1*10^{-6}$ mol NADH per gram of Rh@Bpy-PMO. These findings confirm the NADH adsorption capability of Rh@Bpy-PMO during the regeneration process. Additionally, the adsorption of NADH on Bpy-PMO was also examined, but no changes in NADH concentration were observed on Bpy-PMO.

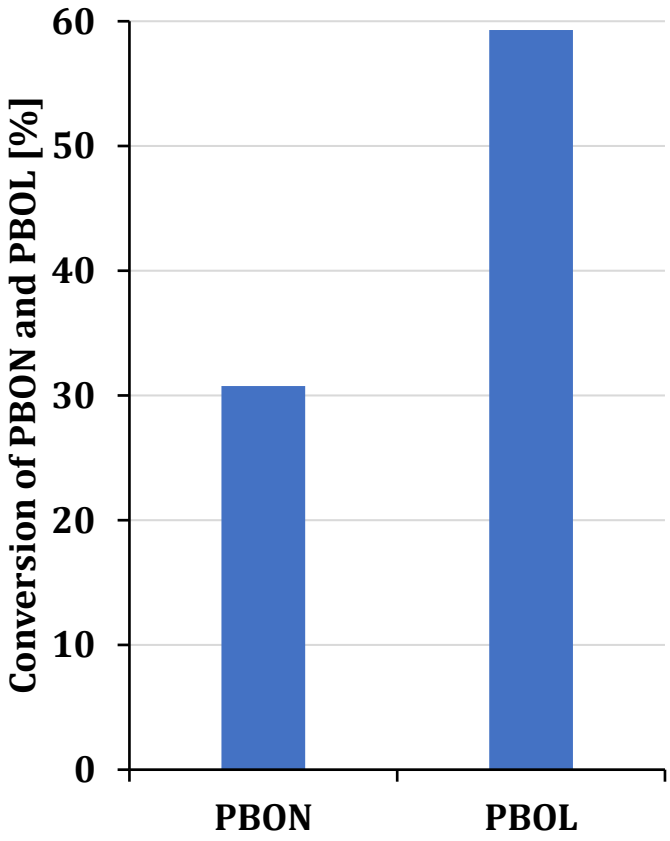

Figure 40: PBON and PBOL conversion by Rh@Bpy-PMO after 5h at 42°C

Finally, the activity of Rh@Bpy-PMO was tested for the conversion of PBON and PBOL using formate, NAD+, and NADH, without the presence of HLADH. The objective of this experiment was to assess whether Rh@Bpy-PMO has the capability to degrade PBON or PBOL. After 5 hours at 42°C, Figure 40 illustrates the conversion of PBON and PBOL. These results provide semi-quantitative information regarding the activity of Rh@Bpy-PMO towards PBON and PBOL, as there is no competition with the enzyme.

However, this experiment reveals that in presence of Rh@Bpy-PMO there is a disappearance PBOL and PBON. The products of these tests were not detected by GC, suggesting that they may be insoluble in ethyl acetate, CO_2 or adsorbed on the PMO.

To be sure that the conversion is due to the rhodium the same test was done but in presence of the $[Cp^*RhCl_2]_2$. After 5h, there is no conversion of the PBON and PBOL by the rhodium complex. This means that the previous result of conversion of PBON and PBOL by Rh@Bpy-PMO is not a “real” conversion but another phenomenon.

One potential explanation as for the NADH, the PBON and PBOL can be adsorb on Rh@Bpy-PMO. To evaluate the amount of PBON that can be adsorbed on Rh@Bpy-PMO, a kinetics of adsorption was conducted for 5 hours (Figure S IV). Considering that PBON is hydrophobic and PMO is also hydrophobic, it is not surprising that PBON adsorbs onto the PMO. The adsorption capacity is determined to be $6.93*10^{-5}$ mol of PBON per gram of Rh@Bpy-PMO. The

adsorption of PBOL was not conduced but the PBON and PBOL having similar polarities it is very likely that the same phenomenon is observed.

5.2.4 Activity comparison between Rh@Bpy-PMO and free HLADH

With the previous results, it is possible to compare the activity of free HLADH and Rh@Bpy-PMO at 42°C. The two catalysts are compared in terms of productivity after 1h. For HLADH, it is $1.2*10^{-7}$ mol of PBOL per mg of HLADH, and for Rh@Bpy-PMO, it is $2.1*10^{-5}$ mol of NADH per mg of rhodium. The Rh@Bpy-PMO catalyst is 2000 times more active than the enzyme on a mass basis.

5.2.5 Discussion on Rh-catalyzed regeneration of NADH

The results of the temperature optimization for the regeneration test indicate that higher temperatures give better yield and productivity. However, the choice of temperature for the catalytic test depends on HLADH, as the NADH regeneration system works much faster than the reduction. The comparison between Rh@Bpy-PMO and HLADH in terms of catalytic activity demonstrates the importance of having much more enzyme than rhodium for the cascade reaction. For future Rh@Bpy-PMO synthesis, the amount of rhodium can be drastically reduced.

Regarding the different characterizations, the obtained results confirmed the successful rhodium grafting on the Bpy-PMO without altering the PMO structure.

Rh@Bpy-PMO demonstrates its ability to regenerate NADH more efficiently than the homogeneous catalyst and to be specific to formate for the NADH regeneration. However, after only one catalytic test, Rh@Bpy-PMO loses 77% of its activity. This decrease was explained as rhodium poisoning by NADH, as evidenced by a color change in the catalyst. However, it is expected that this problem will be resolved during the cascade reaction because NADH will be directly consumed, and there will be a lower amount of NAD+ initially. This will later be confirmed by the remaining pale-yellow color of the catalyst during the cascade reaction in section 5.3.2 Rh@Bpy-PMO has also shown its ability to adsorb PBON and PBOL which can be a problem in the context of a cascade reaction.

5.3 Cascade with two separate catalysts

Before synthesizing the complete hybrid catalyst, we decided to test the reaction with the enzyme and the complex together as a homogeneous catalyst. The test was also conducted with the free enzyme and the Rh@Bpy-PMO.

5.3.1 Cascade with $[Cp^*RhCl_2]_2$ and HLADH as free catalysts

The comparison in terms of conversion, yield and selectivity for the standard reduction test of PBON by HLADH, and the same test with the regeneration of NADH by $[Cp^*RhCl_2]_2$ is shown in Figure 41.

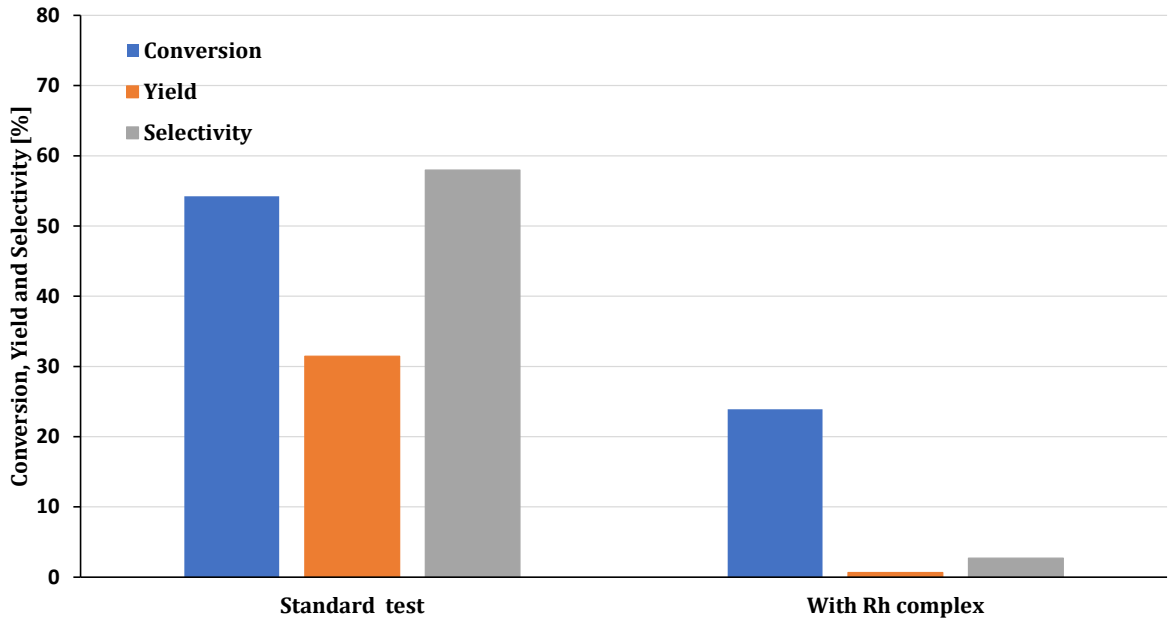

Figure 41: Conversion, yield and selectivity for the reduction of PBON by HLADH in standard conditions and with the addition of $[Cp^*RhCl_2]_2$ (i.e. with NAD+) (5h, 42°C).

The experiment confirms mutual inactivation as all three values decrease drastically. The decrease in all indicators was expected, but the conversion is still significant. It is possible that the enzyme initially works, and the mutual inactivation takes time and during this period, both catalysts may remain active. Additionally, a precipitate is formed at the beginning of the reaction, which could be composed of the enzyme and the complex.

5.3.2 Cascade with Rh@Bpy-PMO and HLADH as free catalyst

Figure 42 presents the results of the cascade reaction involving Rh@Bpy-PMO and free HLADH for the reduction of PBON into PBOL with NADH

regeneration, starting from NAD+. On the left side, the conversion, yield, and selectivity are depicted, while on the right side, the number of moles at the beginning and after 5 hours of the reaction is shown. The full kinetics is available in the appendix (Figure S V)

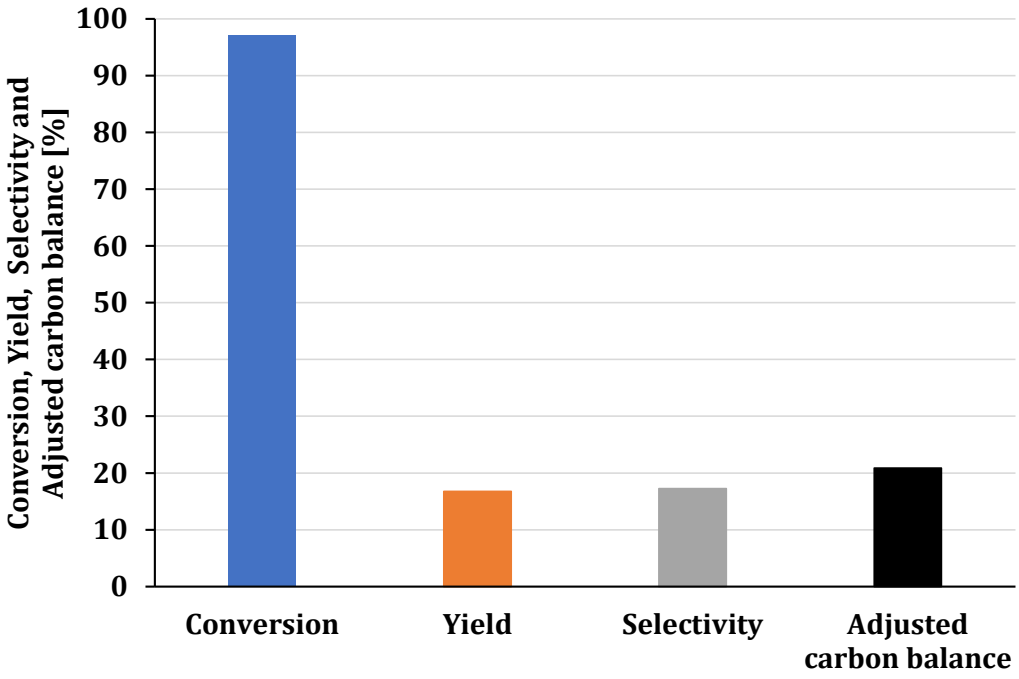

Figure 42: Conversion, yield, selectivity, and the adjusted carbon balance after 5h for the PBON reduction by free HLADH with NADH regeneration by Rh@Bpy-PMO at 42°C.

The cascade reaction involving Rh@Bpy-PMO and free HLADH shows interesting results, achieving 100% conversion after 5 hours. However, the selectivity is quite low (17%). Additionally, the adjusted carbon balance decrease. These results were anticipated, as the PBON adsorption and probably PBOL as well onto the Rh@Bpy-PMO could lead to an overestimation of the conversion value. This is substantiated by the observed decrease in the number of moles.

Figure 43 shows the GC chiral chromatogram of the reduction of PBON by free HLADH with the regeneration of NADH by Rh@Bpy-PMO. As seen in the chromatogram, only S-PBOL is observed, demonstrating the enantioselectivity of the free enzyme despite the presence of Rh@Bpy-PMO.

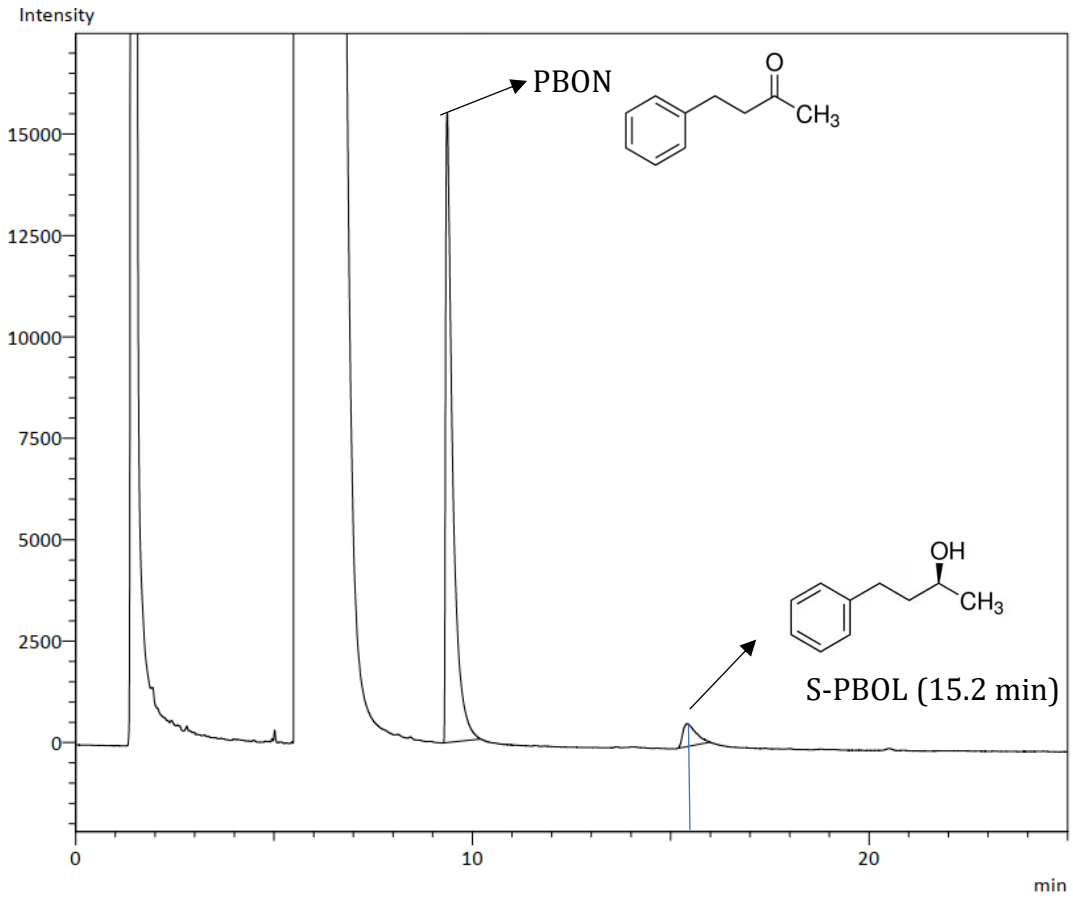

Figure 43: GC chromatogram of the PBON reduction by free HLADH catalyst with NADH regeneration by Rh@Bpy-PMO after 5h at 42°C

5.3.3 Discussion on the cascade with two separate catalysts

The combination of the grafted rhodium catalyst and the free enzyme, seems to work without altering the enantioselectivity of the enzyme. However, the adsorption of PBON (and PBOL) on the catalyst leads to a cascade reaction with low selectivity and very poor adjusted carbon balance. It is therefore expected for all future cascades that the conversion value will be not a good indicator of the catalytic activity, but merely a demonstration of PBON (and PBOL) adsorption. During the cascade and as it was expected the catalyst kept its pale-yellow color throughout the whole batch time. This may confirm the blockage of NADH on rhodium as mentioned earlier in this manuscript.

5.4 Cascade with hybrid catalyst

5.4.1 Characterization of APTES@Bpy-PMO and GLU@Bpy-PMO

N_2 PHYSISORPTION AND XRD

Figure 44 shows the N_2 physisorption isotherm of APTES@Bpy-PMO which exhibits a Type III isotherm without hysteresis. This type of isotherm is characteristic for non-porous or macroporous materials. Grafting APTES decreases the surface area from 870 m^2/g to 10 m^2/g, resulting in a non-porous/macroporous material. The N_2 physisorption of GLU@Bpy-PMO was not performed due to a lack of material.

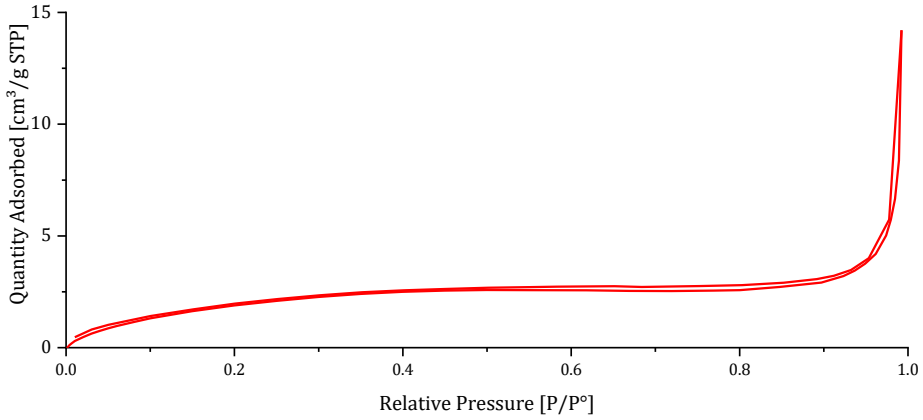

Figure 44: N_2 adsorption and desorption isotherms for APTES@Bpy-PMO

The X-ray diffractogram of Bpy-PMO is compared to APTES@Bpy-PMO and GLU@Bpy-PMO in Figure 45. After the addition of APTES, the (100) XRD peak becomes narrower and shifts towards higher angles. The shift implies a decrease in the value of d_{100} from 6.2 nm for Bpy-PMO to 5.9 nm for APTES@Bpy-PMO. This could be explained by the grafting of APTES inside the pores of the PMO, which results in a narrower peak and a smaller interlayer spacing. The grafting of APTES causes the suppression of (110) and (200) reflection planes, which is a common result when organic compounds are incorporated inside the pore channels of mesoporous materials, leading to an increase in electronic density within the pores. In low-angle XRD mesoporous diffractograms, the intensity depends on the scattering contrast between the pore and the wall. The increase in electronic density decreases the scattering contrast, resulting in a decrease in intensity [131]–[134]. Additionally, a new peak (labeled as "New phase") appears in the diffractogram. This peak could

be attributed to the presence of extra-framework, poorly ordered silica. The grafting of APTES was performed in water-saturated toluene, and APTES, like most organosilanes, undergoes spontaneous hydrolysis and condensation in contact with water. Therefore, the APTES@Bpy-PMO material is likely a mixture of non-porous, aminopropyl-containing silica particles/aggregates, along with fully clogged/covered Bpy-PMO particles. This observation could explain the complete loss of specific surface area measured by N_2 physisorption.

In the XRD diffractogram of GLU@Bpy-PMO, the new phase peak is the only remaining peak. We surmise that multiple GLU molecules react with multiple APTES species inside the pores, creating APTES-GLU-APTES bridges. These bridges increase the electronic density and decrease the intensity of the (100) peak, further supporting the idea of enhanced electronic density within the pores.

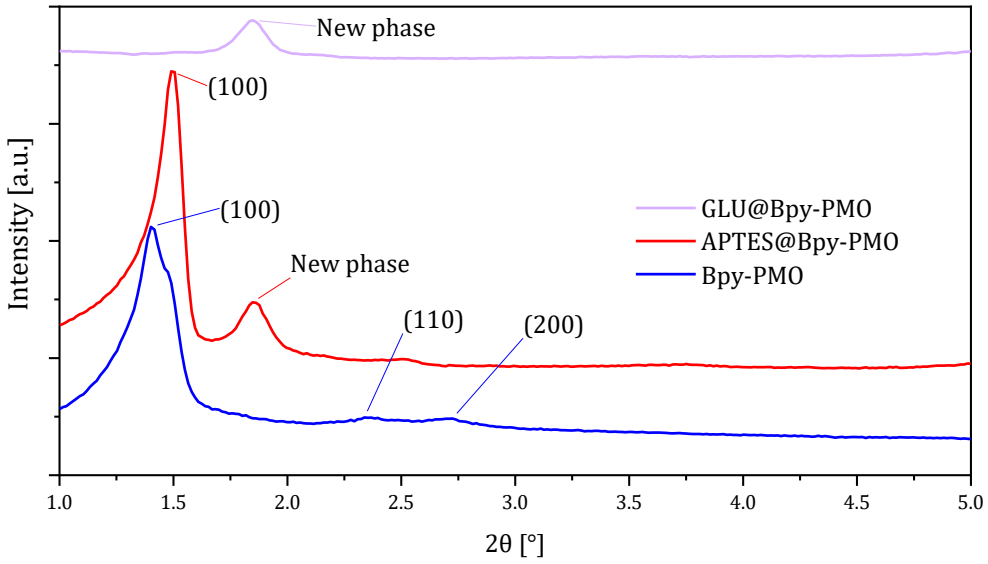

Figure 45: Low angle X-ray diffractograms in the 2θ region of 1°-5° of Bpy-PMO, APTES@Bpy-PMO, and GLU@Bpy-PMO.

To optimize the reaction with APTES, the protocol was modified to investigate the influence of APTES concentration and reaction conditions. By reducing the APTES volume from 5 mL to 1 mL, avoiding the use of dynamic vacuum to prevent APTES from entering the pores, and shortening the reaction time to 6 hours instead of 24 hours, a surface area of 50 m^2/g was achieved (Figure S VI). This result highlights the effective clogging ability of APTES for the PMO material.

FT-IR

IR spectroscopy was utilized to confirm the reactions between Bpy-PMO and APTES and between Bpy-PMO-APTES and GLU. The corresponding spectra can be seen in Figure 46. Upon the addition of APTES, two peaks emerge at 3350 and 1650 cm^{-1}, which can be attributed to the primary amine stretching and bending of APTES. The stretching bands of C-H fall within the range of 2800 to 2930 cm^{-1}, while those between 1000 and 1100 cm^{-1} are associated with Si-O-Si stretching vibration. After the grafting of GLU, the primary amine undergoes conversion into a C=N bond, which becomes evident as a peak at 1645 cm^{-1}.

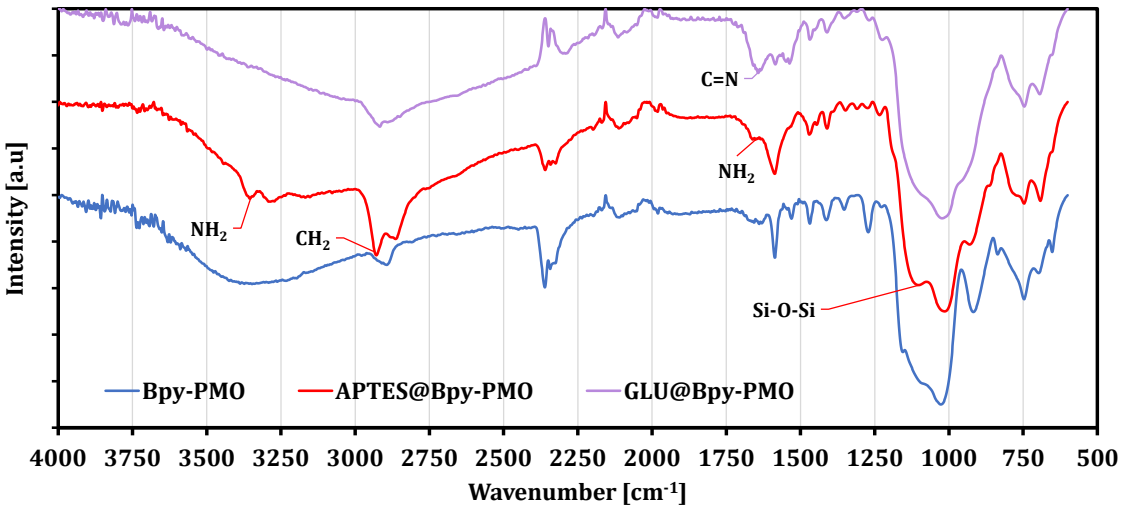

Figure 46: FT-IR spectra of Bpy-PMO, Bpy-PMO-APTES and Bpy-PMO-APTES-GLU between 4000 cm^{-1} and 600 cm^{-1}

The spectra of APTES and GLU are provided for comparison in the appendix (Figure S VII and Figure S VIII).

Based on these measurements, it can be concluded that the functionalization of PMO with APTES and GLU has been achieved and verified by FT-IR analysis. The impact of APTES on the textural properties of PMO, however, is significant. It leads to the complete removal of the surface area by clogging the pores and/or covering the surface with a layer of amorphous silica. These changes in the textural properties are not expected to affect the grafting of HLADH, as the pore diameter of Bpy-PMO is 3.4 nm, which is too small to allow the entry of the enzyme. Therefore, the only available site for enzyme immobilization is the external surface of the PMO material.

5.4.2 HLADH@Bpy-PMO as catalyst for the reduction of PBON

Figure 47 depicts the conversion, yield, selectivity, and the adjusted carbon balance over a 5-hour period for the reduction of PBON by HLADH@Bpy-PMO in the presence of NADH. The corresponding kinetics can be found in the appendix (Figure S IX). The conversion of 98% and the decrease of the adjusted carbon balance after 5 hours, indicate that PBON is again adsorbed on the catalyst. However, both the yield and selectivity plateau at 10%, which are lower results than when the enzyme was free. However, as the amount of enzyme is not quantified on this catalyst, we cannot draw any conclusions about this decrease.

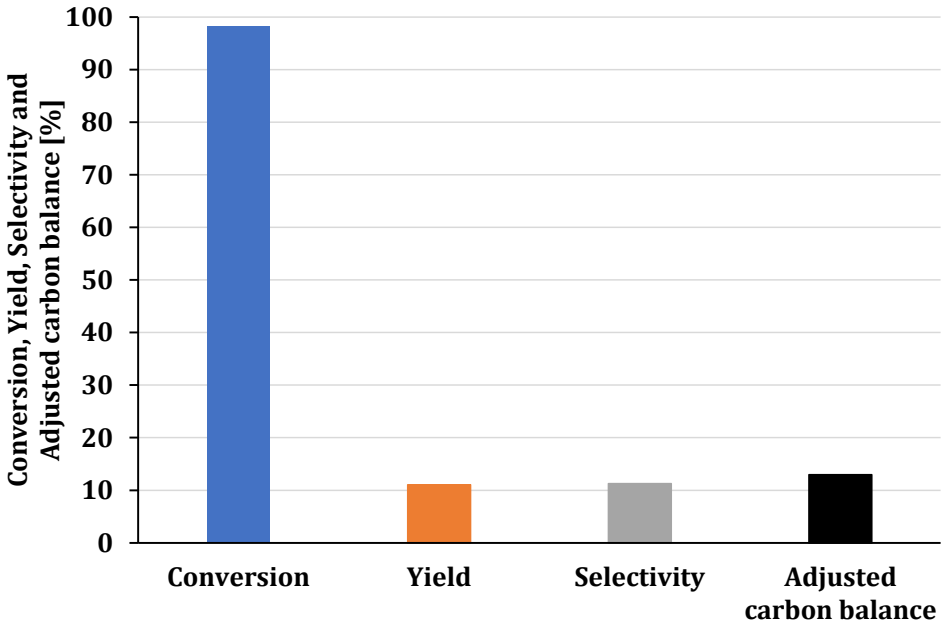

Figure 47: Conversion, yield, selectivity, and the adjusted carbon balance after 5h at 42°C for the PBON reduction by HLADH@Bpy-PMO

The same catalyst was evaluated with NADH regeneration (starting from NAD+) using free $[Cp^*RhCl_2]_2$ as the catalyst. The results are presented in Figure 48, and the complete kinetics provided in the appendix (Figure S X). The presence of the rhodium complex completely changes the results. The observed yield is less than 1%, and the selectivity reaches 4%. The conversion reaches 16%, indicating a 70% decrease compared to the previous test. Consequently, the adjusted carbon balance during the experience decreases by only 14%.

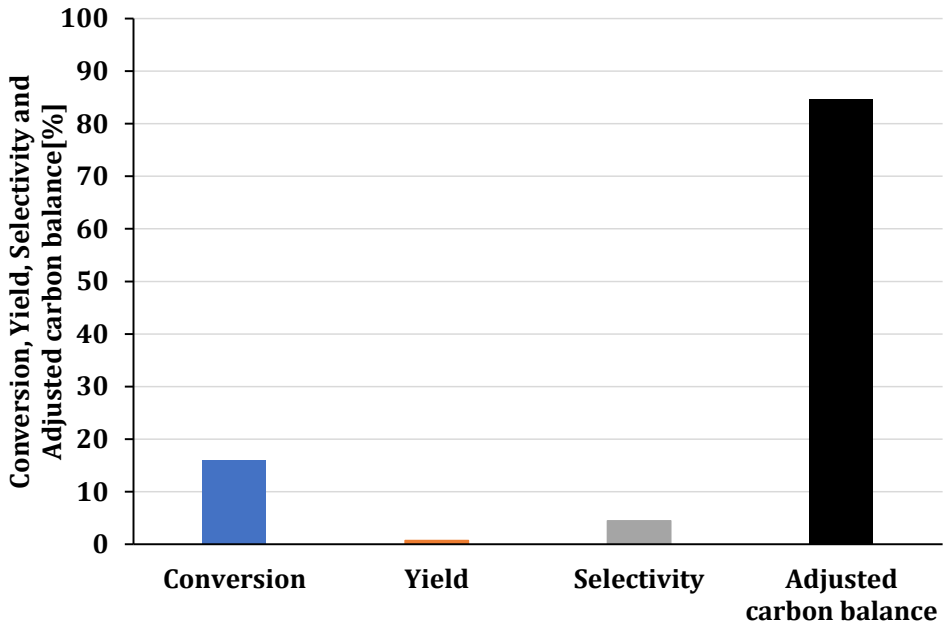

*Figure 48: Conversion, yield, selectivity, and the adjusted carbon balance after 5h at 42°C for the PBON reduction by HLADH@Bpy-PMO with NADH regeneration by [Cp*RhCl$_2$]$_2$.*

These results resemble those obtained in Section 5.3.1 when free HLADH was combined with the free rhodium complex. The rhodium complex deactivates HLADH despite its immobilization. The yields are nearly identical between the two tests: 0.6% for the cascade involving free HLADH and [Cp*RhCl$_2$]$_2$, and 0.7% for the cascade with HLADH@Bpy-PMO and [Cp*RhCl$_2$]$_2$. In this case, the conversion and the decrease of the adjusted carbon balance is low, whereas in the previous test, it reached 100%. This is surprising because this signifies the presence of rhodium complex decrease the possible adsorption of PBON or PBOL. This test should have been repeated to make sure it wasn't an experimental error.

Figure 49 presents the GC chiral chromatogram of the PBON reduction by HLADH@Bpy-PMO after a 5-hour reaction at 42°C. Notably, only the S-PBOL enantiomer is observed in the chromatogram. This outcome holds significant importance as it indicates that HLADH maintains its enantioselectivity even after immobilization.

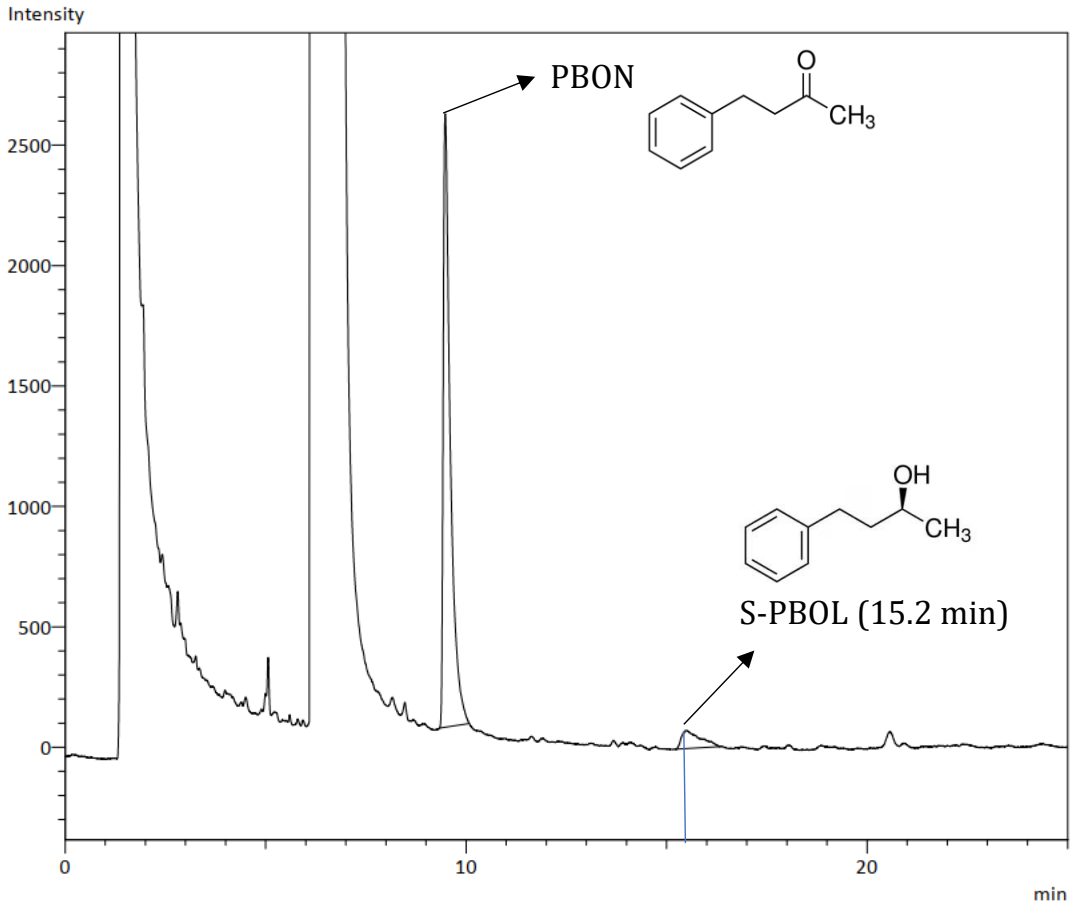

Figure 49: GC chromatogram of the PBON reduction by HLADH@Bpy-PMO after 5h at 42°C

5.4.3 Characterization of APTES-Rh@Bpy-PMO and GLU-APTES-Rh@Bpy-PMO

N_2 PHYSISORPTION

Figure 50 displays the N_2 physisorption isotherms of APTES@Bpy-PMO and APTES-Rh@Bpy-PMO. Both materials exhibit a Type III isotherm, which is typical of non-porous or macroporous materials. There is a minor upward shift observed in the isotherm for Rh@Bpy-PMO-APTES, although the shift is not considered significant.

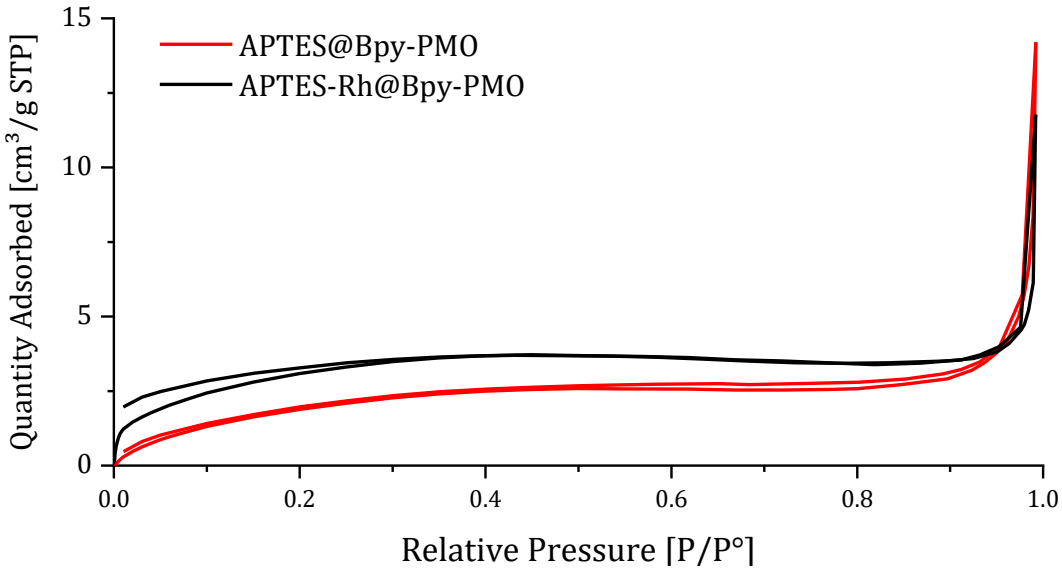

Figure 50: N_2 adsorption and desorption isotherms for APTES@Bpy-PMO and APTES-Rh@Bpy-PMO

The addition of APTES to Rh@Bpy-PMO has a similar effect as observed in Bpy-PMO, leading as anticipated, a substantial decrease of the surface area with a measured value of 10 m^2/g. This outcome is consistent with the isotherm characteristics observed. The same conclusion as observed in APTES@Bpy-PMO can be concluded. N_2 physisorption of GLU-Rh@Bpy-PMO was not performed due to a lack of material.

FT-IR

The presence of APTES and GLU was detected using infrared spectroscopy, as depicted in Figure 51. The characteristic peaks discussed in section 5.4.1, which are associated with APTES and GLU grafting, are clearly evident, confirming the grafting of GLU and APTES onto the material.

An intriguing observation is the presence of a peak for the primary amine at 3350 cm^{-1} in the spectrum of GLU-Rh@Bpy-PMO. This indicates the residual amine from APTES after the addition of GLU, suggesting that some APTES molecules may remain unreacted or partially reacted in the material.

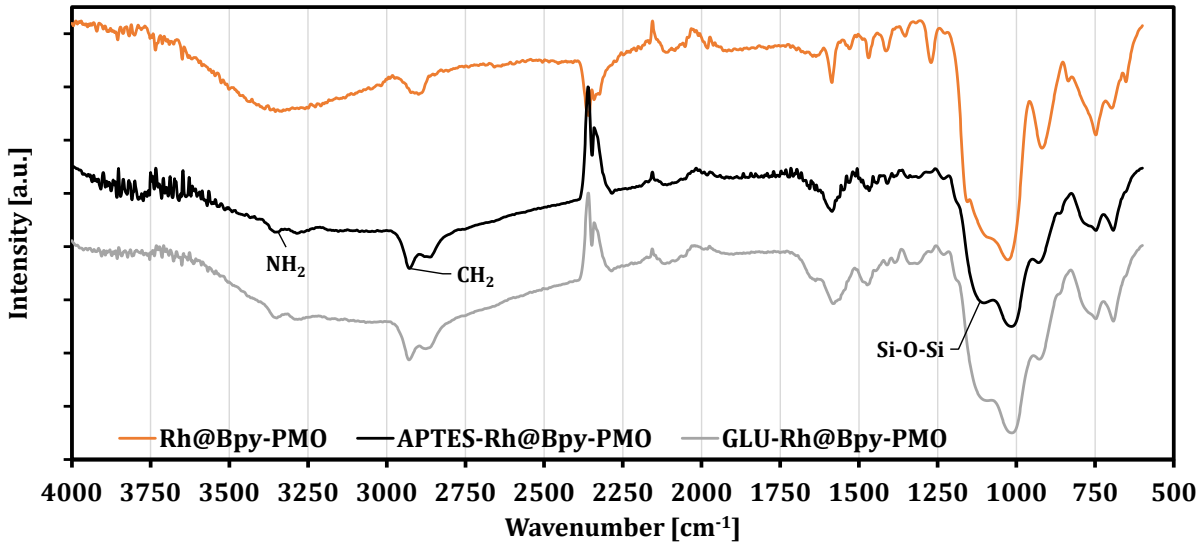

Figure 51: FT-IR spectra of Rh@Bpy-PMO, APTES-Rh@Bpy-PMO and GLU-Rh@Bpy-PMO between 4000 cm^{-1} and 600 cm^{-1}

XRD

The diffractograms of the PMOs are presented in Figure 52. The XRD patterns of APTES-Rh@Bpy-PMO and GLU-Rh@Bpy-PMO exhibit similar results to those of APTES-Bpy-PMO and GLU-Bpy-PMO. The main difference lies in the preservation of the peak corresponding to the (100) plane, though with a shift towards higher angle values. The value of d_{100} decreases from 6.3 nm for Rh@Bpy-PMO to 6.1 nm for APTES-Rh@Bpy-PMO, and further to 4.7 nm for GLU-Rh@Bpy-PMO. This indicates the filling of the pores with each reaction, demonstrating pore occupation.

The hypothesis for the preservation of the (100) peak, despite the addition of GLU, is the incomplete formation of APTES-GLU-APTES bridges inside the pores. This incomplete bridging can also account for the presence of the primary amine peak observed in the FT-IR spectrum of GLU-Rh@Bpy-PMO.

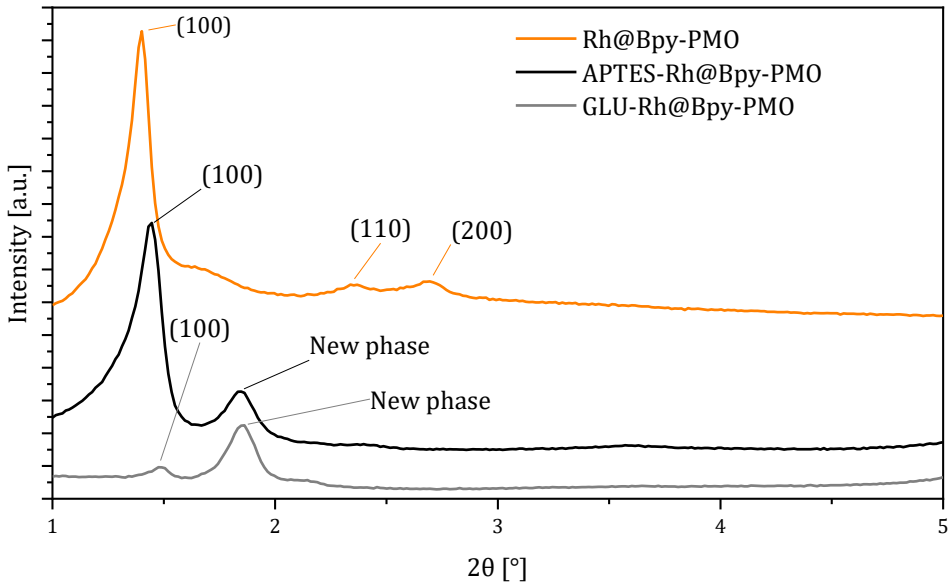

Figure 52: Powder XRD patterns in the 2θ region of 1°-5° of Rh@Bpy-PMO, APTES-Rh@Bpy-PMO, and GLU-Rh@Bpy-PMO

XPS

XPS analysis was conducted to investigate the presence of rhodium on the catalyst's surface of APTES-Rh@Bpy-PMO. Atomic concentrations were obtained, and atomic ratios were calculated as presented in Table 6. An important finding from the XPS analysis is the absence of rhodium. This observation can be explained by comparing the N/Si and O/Si atomic ratios of APTES and APTES-Rh@Bpy-PMO, which provide further information about the catalyst's surface chemistry. The N/Si and O/Si ratios of APTES-Rh@Bpy-PMO closely resemble the theoretical atomic ratio of pure APTES. With the previous characterization results, this demonstrates the formation of a thick amorphous layer of APTES around the Bpy-PMO. The rhodium is likely present beneath this layer, but its presence cannot be detected solely through XPS analysis. To confirm the preservation of the chelating rhodium, further analysis using ICP would be required. A potential concern is that, during the reaction between Rh@Bpy-PMO and APTES, the rhodium could be removed from the material by APTES [135]. To address this hypothesis, ICP analysis of the filtrate obtained after APTES-Rh@Bpy-PMO synthesis would be necessary. If rhodium content is found in the filtrate, it would provide evidence supporting this hypothesis.

Table 6: XPS result APTES-Rh@Bpy-PMO

APTES-Rh@Bpy-PMO						
Atom [-]	O	N	C	Si	Rh	Cl
Atomic Concentration [mol_i/mol_{tot}]	30.3	11.3	47.4	10.7	0	0.31

Atomic ratio [%]	N/Si	O/Si
APTES theoritical	1	3
APTES-Rh@Bpy-PMO	1.06	2.84

In conclusion, the characterization of APTES-Rh@Bpy-PMO and GLU-Rh@Bpy-PMO yielded similar results to APTES@Bpy-PMO and GLU@Bpy-PMO, with the formation of a thick APTES layer around the PMO and the filling of the pores. However, rhodium was not detected on the surface of the catalyst. This finding has significant implications for the efficiency of the catalyst, as the absence of rhodium on the external surface means that NADH cannot be regenerated if the pores are completely clogged.

5.4.4 Cascade with Rh@Bpy-PMO and HLADH@Bpy-PMO

A one-pot reaction using two solid catalysts, HLADH@Bpy-PMO and Rh@Bpy-PMO, was evaluated. Based on the results obtained from the cascade reaction using Rh@Bpy-PMO and free HLADH, as well as the activity of HLADH@Bpy-PMO, it was expected to observe a minimal production of PBOL but a significant conversion and a decrease of the adjusted carbon balance due to the adsorption of PBON. The results (Figure 53) confirm these expectations, showing a substantial conversion but a very low yield and a decrease of the adjusted carbon balance. The complete kinetics data can be found in the appendix in Figure S XI.

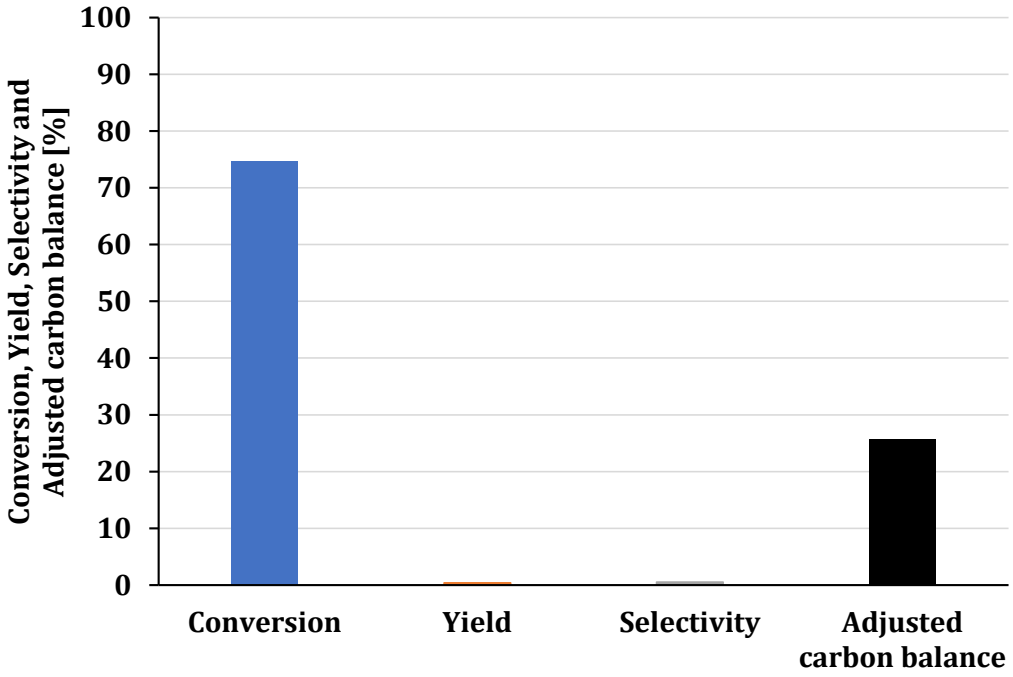

Figure 53: Conversion, yield, selectivity, and the adjusted carbon balance after 5h at 42°C for the PBON reduction by HLADH@Bpy-PMO with NADH regeneration by Rh@Bpy-PMO

5.4.5 Hybrid catalyst HLADH-Rh@Bpy-PMO for the reduction of PBON

Finally, the hybrid catalyst HLADH-Rh@Bpy-PMO was tested for PBON reduction and NADH regeneration, as shown in Figure 54. The complete kinetics data can be found in the appendix in Figure S XII. After 5 hours, the conversion reached 27%, but the yield remained at 0%. A hypothesis to explain like predicted at the end of section 5.4.3, in the absence of accessible rhodium, no NADH was generated, and consequently, no PBOL was produced. The

increase in conversion and the decrease in the adjusted carbon balance is attributed to PBON adsorption, as previously observed in this study.

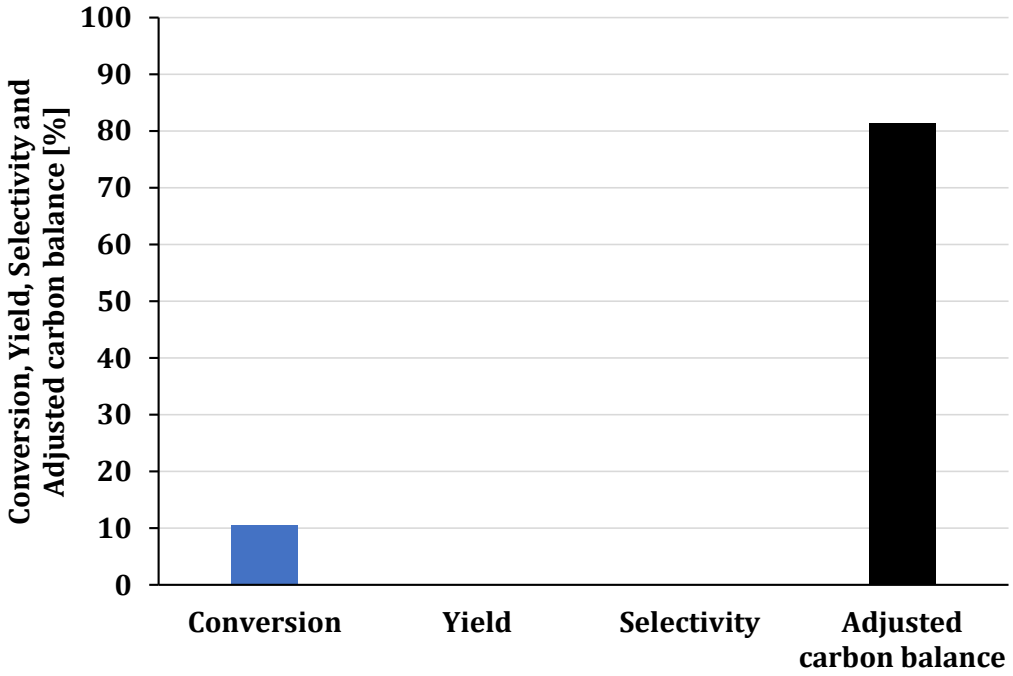

Figure 54: Conversion, yield, selectivity, and the adjusted carbon balance after 5h at 42°C for the PBON reduction by HLADH-Rh@Bpy-PMO

5.4.6 Discussion of the cascade with the hybrid catalyst

The immobilization of HLADH on Bpy-PMO was performed, but the grafting process had a significant impact on the properties of Bpy-PMO. Unfortunately, the high surface area of the material was not preserved after APTES grafting, leading to the formation of a thick APTES layer around the PMO. This outcome can be attributed to the use of dynamic vacuum conditions during APTES grafting and the high concentration of APTES in water-saturated toluene. Although HLADH immobilization maintained the enzyme's enantioselectivity, it resulted in a threefold reduction in PBOL production.

As expected, grafting APTES onto Rh@Bpy-PMO yielded similar results to APTES@Bpy-PMO. The formation of a surrounding layer on APTES-Rh@Bpy-PMO, which probably conceals the rhodium, rendered NADH generation impossible. As a result, HLADH-Rh@Bpy-PMO exhibited no activity.

5.5 General Discussion

The results obtained in this manuscript demonstrate the attempt of producing a hybrid catalyst, but it requires further work. Indeed, rhodium has shown high activity when grafted onto Bpy-PMO. Additionally, the free HLADH enzyme is 2000 times less active, and its activity is reduced by a factor of 3 during grafting. This results in a significant difference in activity between rhodium and the enzyme. In future syntheses, it is necessary to consider this activity differential by increasing the enzyme quantity and reducing the amount of rhodium. However, it has been demonstrated that enzyme deactivation is eliminated when rhodium is immobilized.

Regarding the impact of different grafting processes on Bpy-PMO, rhodium only slightly reduces the pore size due to the size of the complex itself, without modifying the chemical functionalities of the material. On the other hand, the addition of APTES and GLU has a much more significant impact, completely covering the material's surface and forming a layer of APTES on the PMOs. While this does not affect enzyme grafting since the enzyme cannot enter the pores, it covers the rhodium, making NADH regeneration impossible.

Conclusions and perspectives

6. CONCLUSIONS AND PERSPECTIVES

6.1 Conclusions

In conclusion, this master thesis aimed to investigate the synthesis of a rhodium-HLADH hybrid catalyst for the enantioselective reduction of ketone.

We were able to successfully produce Rh@Bpy-PMO and demonstrate its activity as a catalyst for NADH regeneration. The cascade reaction with Rh@Bpy-PMO and HLADH together resulted in high conversion due to PBON adsorption and a lower yield compared to using free HLADH alone. The productivity of Rh@Bpy-PMO was found to be 2000 times higher than that of free HLADH. All the working catalysts in this manuscript demonstrate the production of only S-PBON, indicating enantioselectivity.

The immobilization of HLADH on Bpy-PMO using the APTES strategy was achieved. The results confirm that HLADH@Bpy-PMO works, but when combined with $[Cp^*RhCl_2]_2$, enzyme deactivation occurs, and when HLADH@Bpy-PMO is combined with Rh@Bpy-PMO, the yield was very low.

The current hybrid catalyst consisting of HLADH and the rhodium complex on the same Bpy-PMO showed no production of PBOL after 5 hours.

6.2 Perspectives

Since Rh@Bpy-PMO exhibits high activity, reducing the rhodium loading is crucial for future Rh@Bpy-PMO synthesis. Considering the high cost of rhodium and the superior activity of Rh@Bpy-PMO compared to HLADH, reducing these expenses becomes a valid argument.

It's also crucial to enhance the analytical analysis, particularly concerning the adjusted carbon balance. Introducing the reaction medium into HPLC could provide valuable insights into potential side reactions. To validate the generation of CO_2 by Rh@Bpy-PMO, supplementary tests, such as in situ CO_2 monitoring, should be conducted.

To prevent pore clogging, optimization of reactions between Rh@Bpy-PMO or Bpy-PMO with APTES is necessary. Parameters such as decreasing APTES concentration, reducing reaction time, and eliminating dynamic vacuum should be optimized.

For all the presented catalysts with immobilized HLADH, no quantity of HLADH was provided. This is due to the failure of all quantification attempts. It is necessary to develop an accurate method for enzyme quantification such as indirect UV-vis [136].

If the APTES enzyme immobilization strategy is unsuccessful, covalent attachment using (3-glycidyloxypropyl)trimethoxysilane (GLYMO) can be investigated. Other types of enzyme immobilization, such as the production of hierarchical PMO sphere with the HLADH inside [137].

It would be beneficial to optimize the enantiomer separation in GC chiral in future studies by using a dedicated chiral column in the laboratory for more accurate and precise analysis.

Once the hybrid catalyst is successfully developed, exploring other substrates would be interesting. The next step would be to move beyond model reactions and apply it to more meaningful applications, such as the reduction of ethyl 4-chloro acetoacetate into ethyl (S)-4-chloro-3-hydroxybutanoate. This compound serves as an intermediate for the synthesis of Atorvastatin, a medication used for the prevention of cardiovascular disease [11].

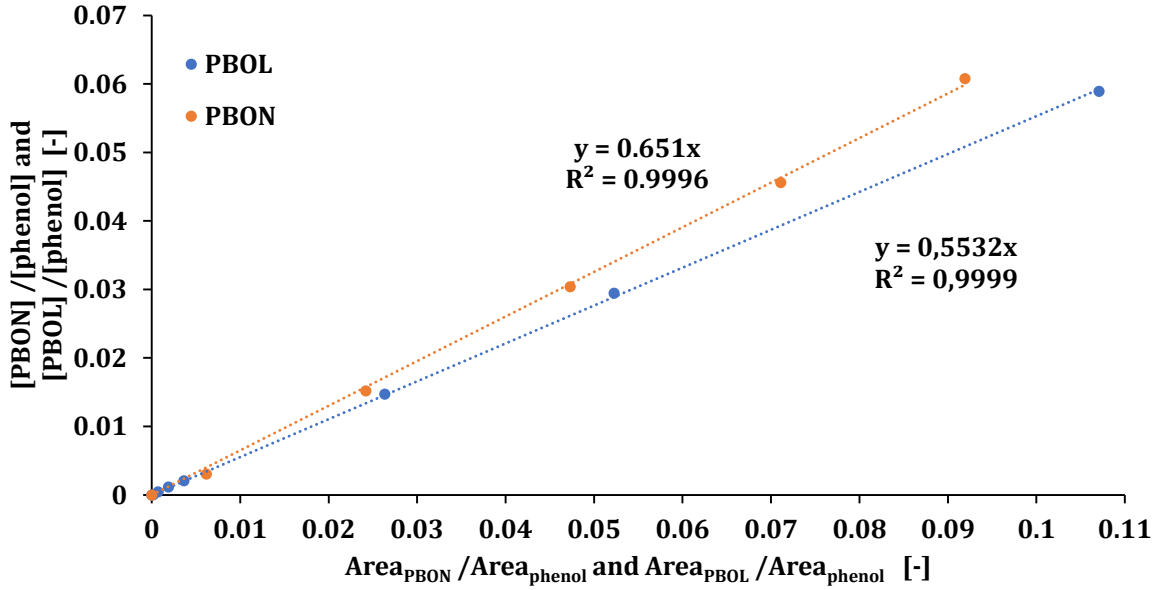

Figure S I: PBON GC calibration curves - Concentration ratio compared to area ratio.

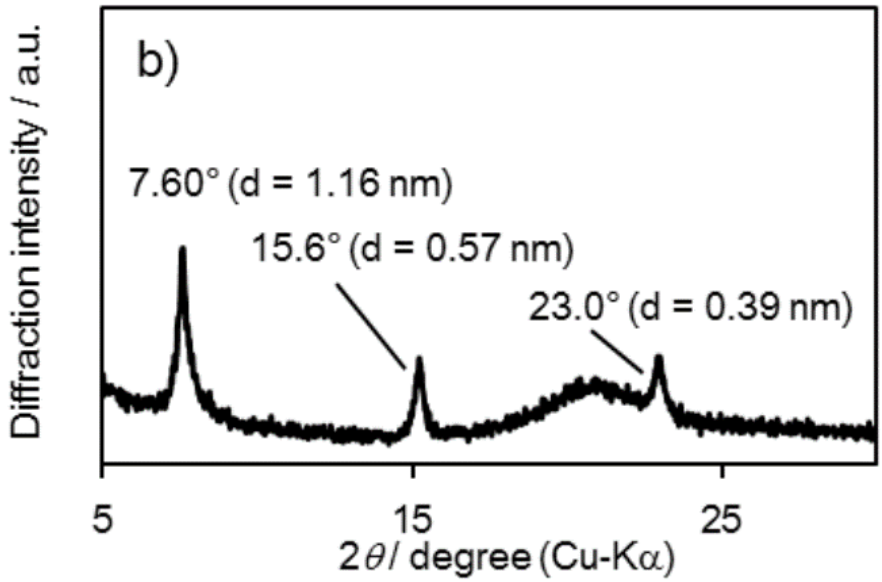

Figure S II: Powder XRD pattern of a Rh@Bpy-PMO in the high-angle region [80]

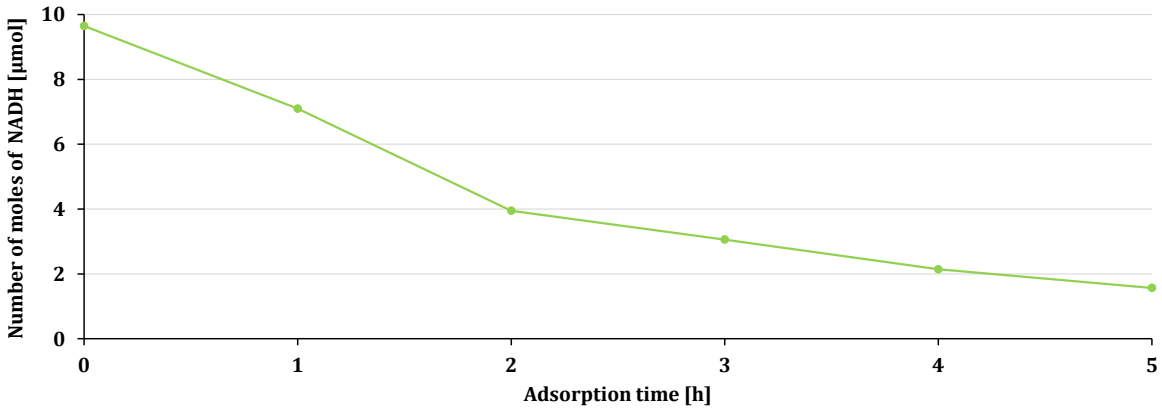

Figure S III: Kinetic of NADH adsorption on Rh@Bpy-PMO during 5h at 42°C

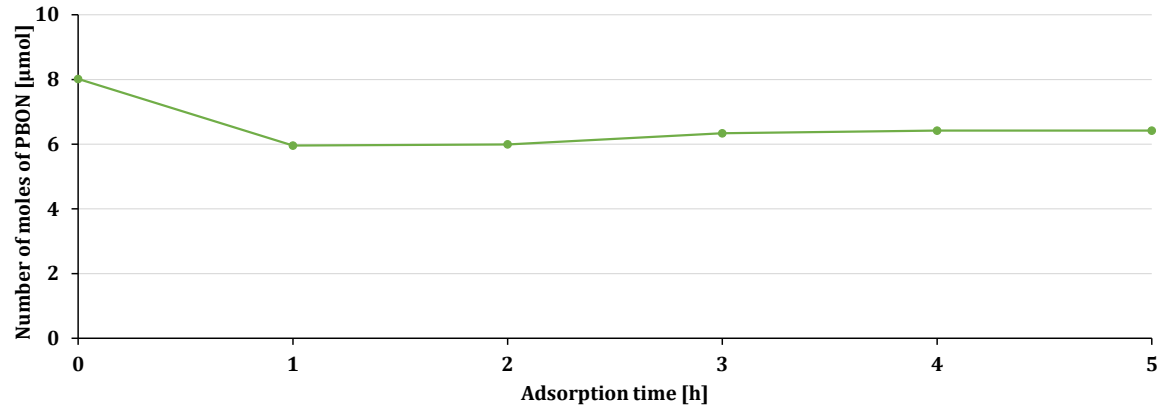

Figure S IV: Kinetic of PBON adsorption on Rh@Bpy-PMO during 5h at 42°

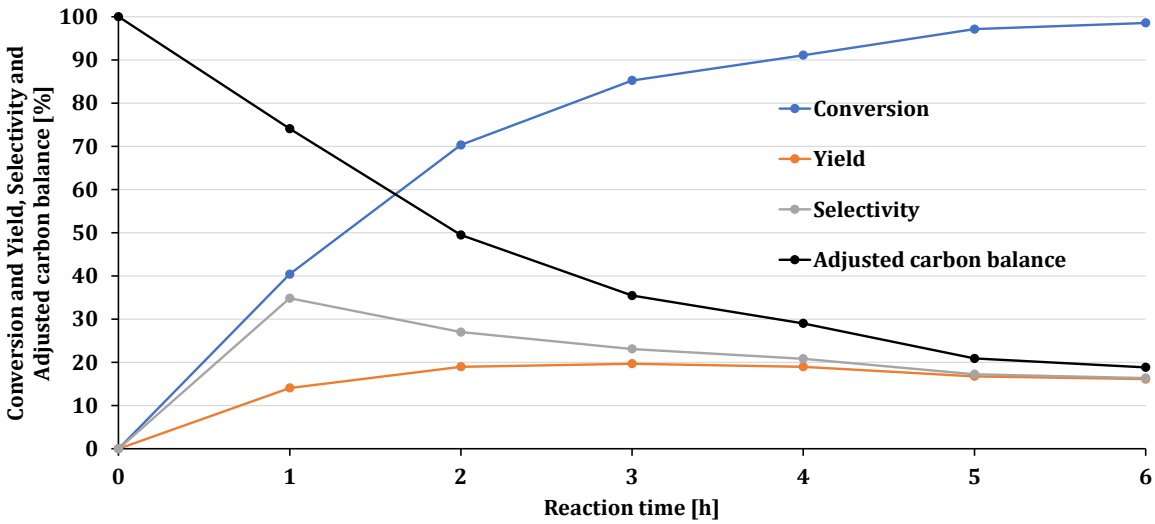

Figure S V: Conversion, yield, selectivity, and adjusted carbon balance for the PBON reduction by free HLADH with NADH regeneration by Rh@Bpy-PMO at 42°C during 5h.

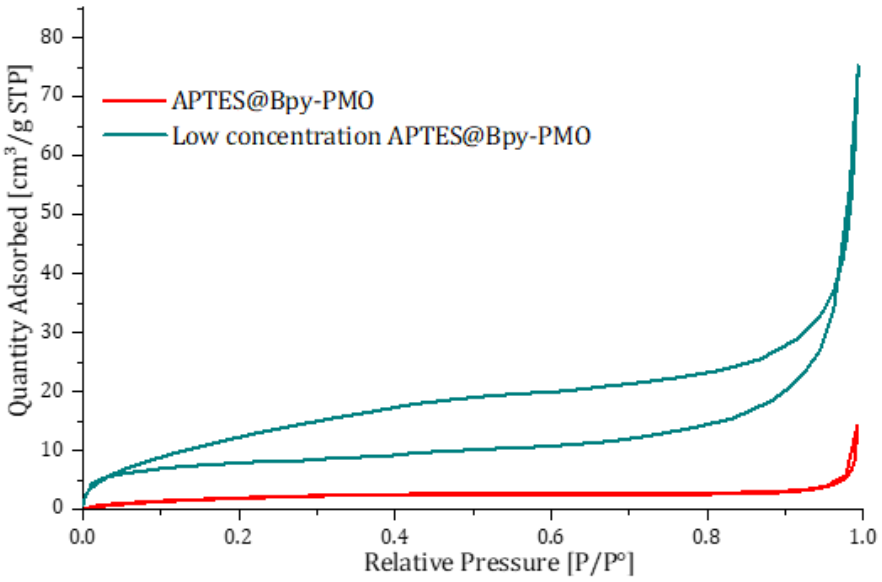

Figure S VI: N_2 adsorption and desorption isotherms for APTES@Bpy-PMO and low concentration APTES@Bpy-PMO

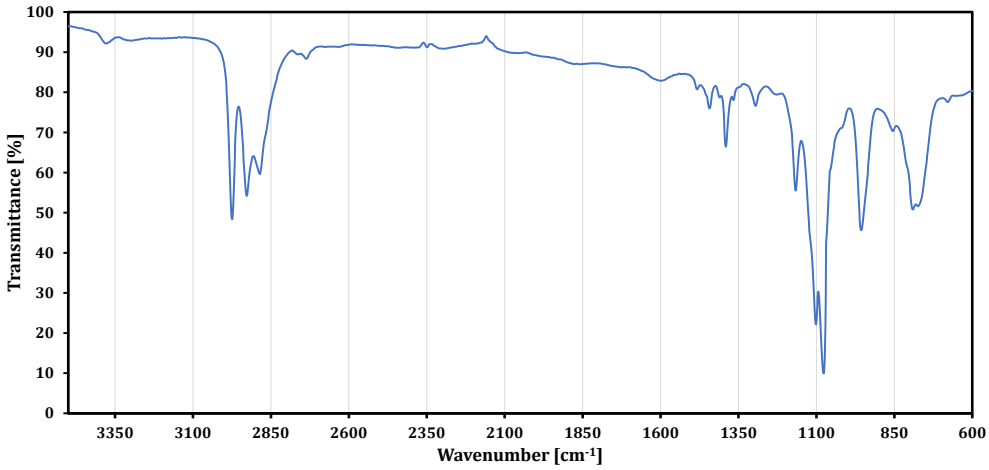

Figure S VII: FT-IR of APTES between 3500 cm^{-1} and 600 cm^{-1}

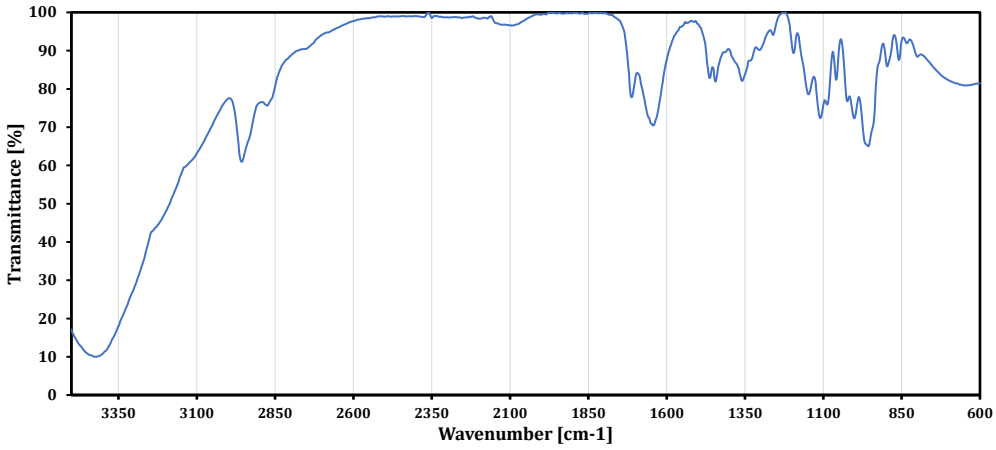

Figure S VIII: FT-IR of GLU between 3500 cm^{-1} and 600 cm^{-1}

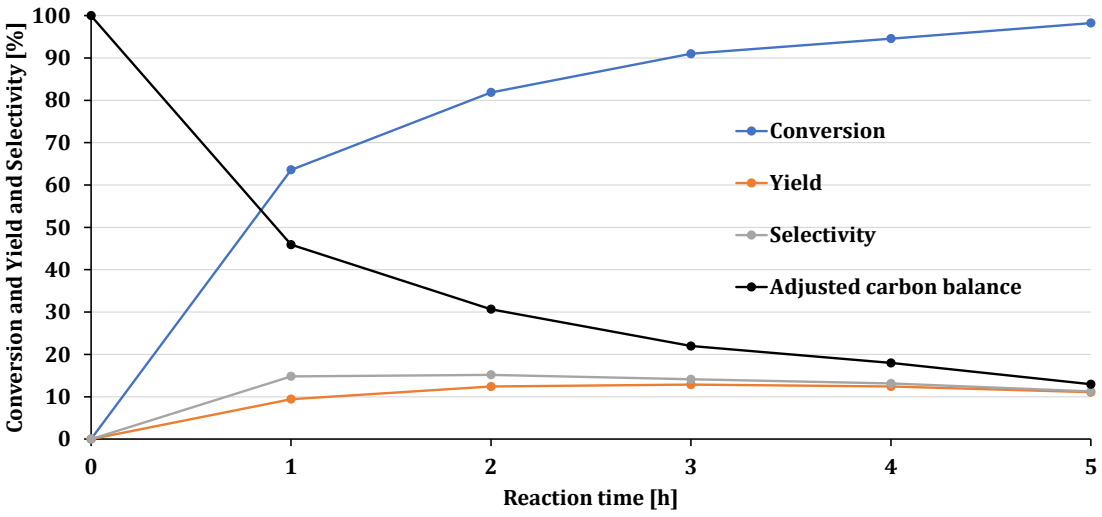

Figure S IX: Conversion, yield, selectivity, and the adjusted carbon balance for the PBON reduction by HLADH@Bpy-PMO at 42°C during 5h.

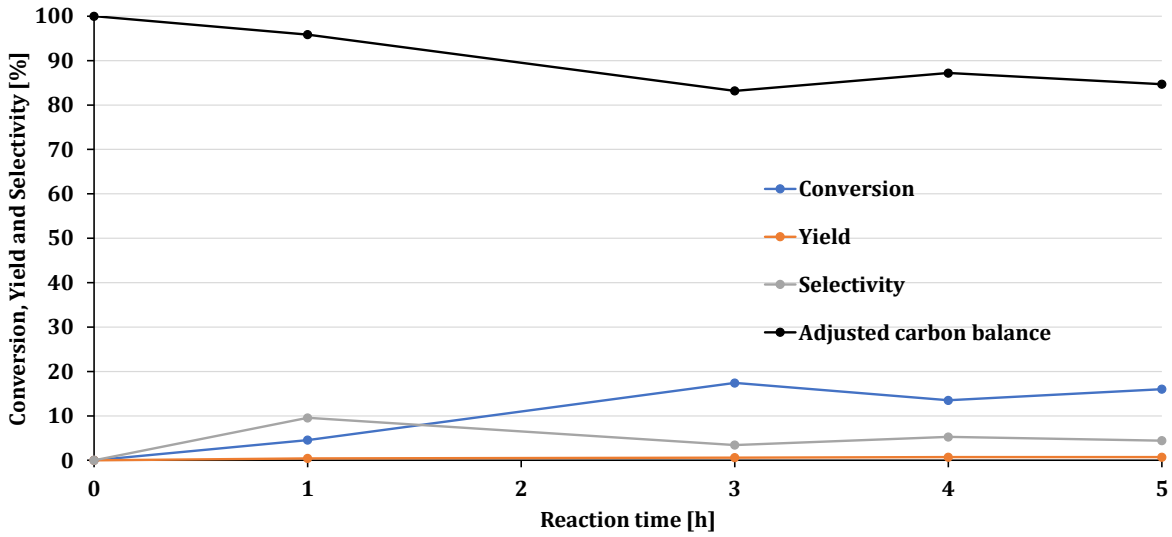

Figure S X: Conversion, yield, selectivity, and the adjusted carbon balance of the PBON reduction by HLADH@Bpy-PMO with NADH regeneration by $[Cp^*RhCl_2]_2$ at 42°C during 5h.

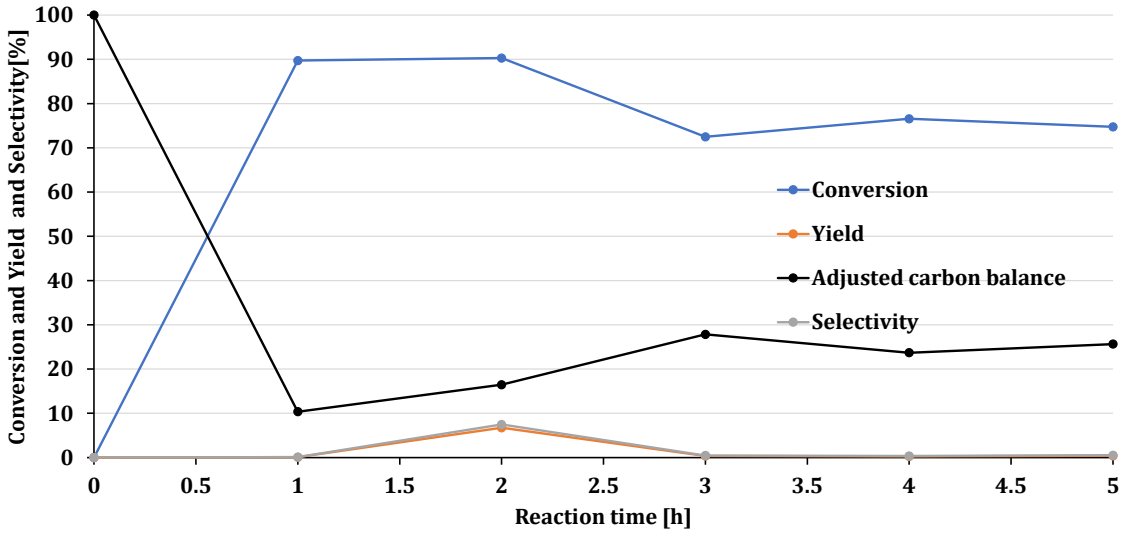

Figure S XI: Conversion, yield, selectivity, and the adjusted carbon balance for the PBON reduction by HLADH@Bpy-PMO with NADH regeneration by Rh@Bpy-PMO at 42°C during 5h

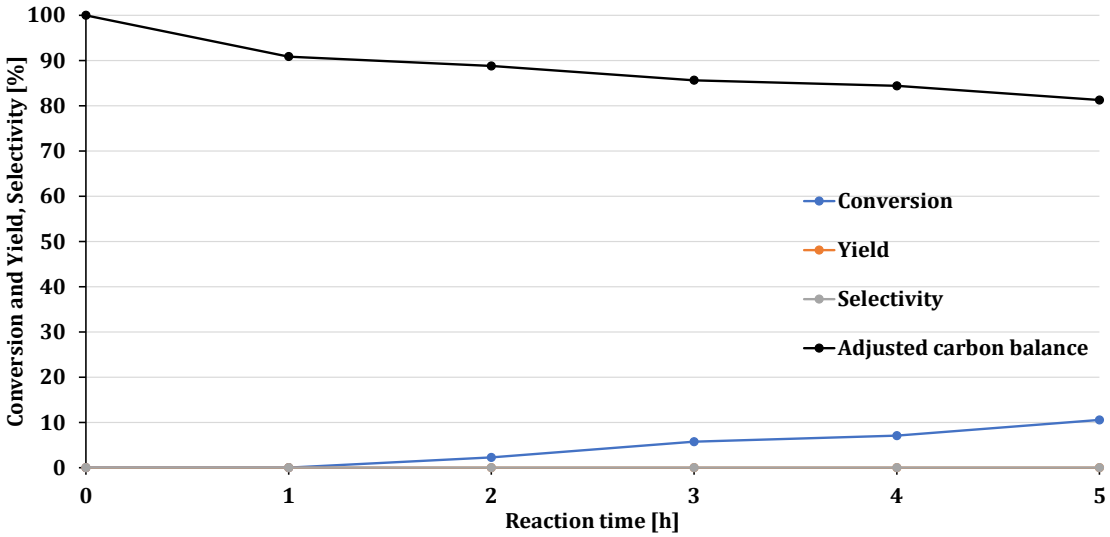

Figure S XII: Conversion, yield, selectivity, and the adjusted carbon balance for the PBON reduction and NADH regeneration by HLADH-Rh@Bpy-PMO at 42°C during 5h

8. BIBLIOGRAPHY

[1] "Environment, Health, Safety and Sustainability." https://www.efpia.eu/about-medicines/development-of-medicines/regulations-safety-supply/environment-health-safety-and-sustainability/ (accessed Mar. 08, 2023).

[2] A. Nawrat, "Pharma and the environment: pollution continues despite public pressure," *Pharmaceutical Technology*, Oct. 02, 2018. https://www.pharmaceutical-technology.com/features/pharma-and-the-environment-pollution-trend/ (accessed Mar. 08, 2023).

[3] M. Hall, W. Kroutil, and V. Kren, "A Career in Biocatalysis: Kurt Faber | ACS Catalysis," Mar. 2022, Accessed: Mar. 26, 2023. [Online]. Available: https://pubs.acs.org/doi/10.1021/acscatal.2c00579

[4] S. Kar, H. Sanderson, K. Roy, E. Benfenati, and J. Leszczynski, "Green Chemistry in the Synthesis of Pharmaceuticals," *Chem. Rev.*, vol. 122, no. 3, pp. 3637–3710, Feb. 2022, doi: 10.1021/acs.chemrev.1c00631.

[5] K. Kümmerer, "Pharmaceuticals in the Environment," *Annual Review of Environment and Resources*, vol. 35, no. 1, pp. 57–75, 2010, doi: 10.1146/annurev-environ-052809-161223.

[6] D. Ager and O. May, "Pharmaceutical Industry: Biocatalysts and Chemocatalysts," 2008. doi: 10.1002/9780470048672.wecb651.

[7] W. Hummel, "New alcohol dehydrogenases for the synthesis of chiral compounds," *Adv Biochem Eng Biotechnol*, vol. 58, pp. 145–184, 1997, doi: 10.1007/BFb0103304.

[8] I. A. Kaluzna, J. David Rozzell, and S. Kambourakis, "Ketoreductases: stereoselective catalysts for the facile synthesis of chiral alcohols," *Tetrahedron: Asymmetry*, vol. 16, no. 22, pp. 3682–3689, Nov. 2005, doi: 10.1016/j.tetasy.2005.10.002.

[9] H. M. Arango *et al.*, "Continuous flow-mode synthesis of (chiral) amines with transaminase: a strategic biocatalytic approach to essential building blocks," *React. Chem. Eng.*, vol. 8, no. 7, pp. 1505–1544, Jun. 2023, doi: 10.1039/D3RE00210A.

[10] S. P. France, R. D. Lewis, and C. A. Martinez, "The Evolving Nature of Biocatalysis in Pharmaceutical Research and Development," *JACS Au*, Feb. 2023, doi: 10.1021/jacsau.2c00712.

[11] R. N. Patel, "Biocatalytic Synthesis of Chiral Alcohols and Amino Acids for Development of Pharmaceuticals," *Biomolecules*, vol. 3, no. 4, pp. 741–777, Oct. 2013, doi: 10.3390/biom3040741.

[12] T. R. McCaw *et al.*, “Gamma Secretase Inhibitors in Cancer: A Current Perspective on Clinical Performance,” *The Oncologist*, vol. 26, no. 4, pp. e608–e621, 2021, doi: 10.1002/onco.13627.

[13] “Merck | Belgium.” https://www.sigmaaldrich.com/BE/fr (accessed Apr. 06, 2023).

[14] P. Bruice, *Chimie oranique*, 2éme. 2012.

[15] lumen, “4.4. Molecules with multiple chiral centers | Organic Chemistry 1: An open textbook.” https://courses.lumenlearning.com/suny-potsdam-organicchemistry/chapter/4-4-molecules-with-multiple-chiral-centers/ (accessed Apr. 23, 2023).

[16] R. S. Cahn, C. Ingold, and V. Prelog, “Specification of Molecular Chirality,” *Angewandte Chemie International Edition in English*, vol. 5, no. 4, pp. 385–415, 1966, doi: 10.1002/anie.196603851.

[17] J. Gal, “The Discovery of Stereoselectivity at Biological Receptors: Arnaldo Piutti and the Taste of the Asparagine Enantiomers—History and Analysis on the 125th Anniversary,” *Chirality*, vol. 24, no. 12, pp. 959–976, 2012, doi: 10.1002/chir.22071.

[18] C. Zipper, M. Bunk, A. J. B. Zehnder, and H.-P. E. Kohler, “Enantioselective Uptake and Degradation of the Chiral Herbicide Dichlorprop [(RS)-2-(2,4-Dichlorophenoxy)propanoic acid] by Sphingomonas herbicidovorans MH,” *J Bacteriol*, vol. 180, no. 13, pp. 3368–3374, Jul. 1998.

[19] K. M. Rentsch, “The importance of stereoselective determination of drugs in the clinical laboratory,” *J Biochem Biophys Methods*, vol. 54, no. 1–3, pp. 1–9, Dec. 2002, doi: 10.1016/s0165-022x(02)00124-0.

[20] J. Leffingwell, “Chirality & Bioactivity I.: Pharmacology.” 203AD.

[21] R. E. Gawley, “Do the Terms ‘%ee’ and ‘%de’ Make Sense as Expressions of Stereoisomer Composition or Stereoselectivity?,” *J Org Chem*, vol. 71, no. 6, pp. 2411–2416, Mar. 2006, doi: 10.1021/jo052554w.

[22] J. R. J. Maynard and S. M. Goldup, “Strategies for the Synthesis of Enantiopure Mechanically Chiral Molecules,” *Chem*, vol. 6, no. 8, pp. 1914–1932, Aug. 2020, doi: 10.1016/j.chempr.2020.07.012.

[23] Dr. K. Kumar, “CHIRAL SYNTHESIS: AN OVERVIEW,” *International Journal of Pharmaceutical Research and development*, vol. 6, p. 70, Jun. 2014.

[24] O. I. Kolodiazhnyi and A. Kolodiazhna, “Nucleophilic substitution at phosphorus: stereochemistry and mechanisms,” *Tetrahedron: Asymmetry*, vol. 28, no. 12, pp. 1651–1674, Dec. 2017, doi: 10.1016/j.tetasy.2017.10.022.

[25] G. Diaz-Muñoz, I. L. Miranda, S. K. Sartori, D. C. de Rezende, and M. Alves Nogueira Diaz, “Use of chiral auxiliaries in the asymmetric synthesis of biologically active compounds: A review,” *Chirality*, vol. 31, no. 10, pp. 776–812, 2019, doi: 10.1002/chir.23103.

[26] T. Fornstedt, P. Forssén, and J. Samuelsson, “Chapter 18 - Modeling of Preparative Liquid Chromatography,” in *Liquid Chromatography*, S. Fanali, P. R. Haddad, C. F. Poole, P. Schoenmakers, and D. Lloyd, Eds., Amsterdam: Elsevier, 2013, pp. 407–425. doi: 10.1016/B978-0-12-415807-8.00018-3.

[27] B. Sekhon, “Enantioseparation of chiral drugs - An overview,” *International Journal of PharmTech Research*, vol. 2, pp. 1584–94, Apr. 2010.

[28] L. A. Nguyen, H. He, and C. Pham-Huy, “Chiral Drugs: An Overview,” *Int J Biomed Sci*, vol. 2, no. 2, pp. 85–100, Jun. 2006.

[29] F. Leng, O. Shemchuk, K. Robeyns, and T. Leyssens, “Complexation: An Interesting Pathway for Combining Two APIs at the Solid State,” *Pharmaceutics*, vol. 14, no. 9, p. 1960, Sep. 2022, doi: 10.3390/pharmaceutics14091960.

[30] X. Buol *et al.*, “Chiral Resolution of Mandelic Acid through Preferential Cocrystallization with Nefiracetam,” *Crystal Growth & Design*, vol. 20, no. 12, pp. 7979–7988, Dec. 2020, doi: 10.1021/acs.cgd.0c01236.

[31] B. Harmsen and T. Leyssens, “Dual-Drug Chiral Resolution: Enantiospecific Cocrystallization of (S)-Ibuprofen Using Levetiracetam,” *Crystal Growth & Design*, vol. 18, no. 1, pp. 441–448, Jan. 2018, doi: 10.1021/acs.cgd.7b01431.

[32] Y. Teng *et al.*, “Advances and applications of chiral resolution in pharmaceutical field,” *Chirality*, vol. 34, no. 8, pp. 1094–1119, 2022, doi: 10.1002/chir.23453.

[33] H. M and H. MR, “Recent Development: Enantioselective Extraction in Chiral Separation,” *Austin Journal of Analytical and Pharmaceutical Chemistry*, vol. 8, Mar. 2021, doi: 10.26420/austininternmed.2021.1130.

[34] P. Y. Quintas, E. F. Fiorentini, M. Llaver, R. E. González, and R. G. Wuilloud, “State-of-the-art extraction and separation of enantiomers through the application of alternative solvents,” *TrAC Trends in Analytical Chemistry*, vol. 157, p. 116733, Dec. 2022, doi: 10.1016/j.trac.2022.116733.

[35] M. Pinto, C. Fernandes, and M. Tiritan, “Chiral Separations in Preparative Scale: A Medicinal Chemistry Point of View,” *Molecules*, vol. 25, p. 1931, Apr. 2020, doi: 10.3390/molecules25081931.

[36] X.-W. Sun and G.-Q. Lin, “Chiral Drugs through Asymmetric Synthesis - Chiral Drugs - Wiley Online Library,” Jul. 18, 2011.

https://onlinelibrary.wiley.com/doi/abs/10.1002/9781118075647.ch2 (accessed Apr. 26, 2023).

[37] "The Nobel Prize in Chemistry 2001," *NobelPrize.org*. https://www.nobelprize.org/prizes/chemistry/2001/summary/ (accessed Jan. 01, 2023).

[38] "The Nobel Prize in Chemistry 2021," *NobelPrize.org*. https://www.nobelprize.org/prizes/chemistry/2021/popular-information/ (accessed Jan. 01, 2023).

[39] H. U. Blaser, "Enantioselective catalysis in fine chemicals production - ScienceDirect," Nov. 30, 2001. https://www.sciencedirect.com/science/article/abs/pii/S0926860X01008018 (accessed Dec. 29, 2022).

[40] P. J. Walsh, "Asymmetric Synthesis by Homogeneous Catalysis Based in part on the article Asymmetric Synthesis by Homogeneous Catalysis by Brice Bosnich which appeared in the Encyclopedia of Inorganic Chemistry, First Edition.," in *Encyclopedia of Inorganic and Bioinorganic Chemistry*, John Wiley & Sons, Ltd, 2011. doi: 10.1002/9781119951438.eibc0015.

[41] M. Heitbaum, F. Glorius, and I. Escher, "Asymmetric Heterogeneous Catalysis," *Angewandte Chemie International Edition*, vol. 45, no. 29, pp. 4732–4762, 2006, doi: 10.1002/anie.200504212.

[42] A. Tungler, É. Sípos, and V. Háda, "Asymmetric heterogeneous catalytic hydrogenation; is it a useful tool for the synthetic organic chemist?," *Arkivoc*, vol. 2004, Jun. 2004, doi: 10.3998/ark.5550190.0005.718.

[43] D. J. Watson, R. J. B. R. John Jesudason, S. K. Beaumont, G. Kyriakou, J. W. Burton, and R. M. Lambert, "Heterogeneously Catalyzed Asymmetric Hydrogenation of C═C Bonds Directed by Surface-Tethered Chiral Modifiers," *J. Am. Chem. Soc.*, vol. 131, no. 40, pp. 14584–14589, Oct. 2009, doi: 10.1021/ja906356g.

[44] T. J. Lawton *et al.*, "Long Range Chiral Imprinting of Cu(110) by Tartaric Acid," *J. Phys. Chem. C*, vol. 117, no. 43, pp. 22290–22297, Oct. 2013, doi: 10.1021/jp402015r.

[45] P. E. V. Paul, V. Sangeetha, and R. G. Deepika, "Chapter 9 - Emerging Trends in the Industrial Production of Chemical Products by Microorganisms," in *Recent Developments in Applied Microbiology and Biochemistry*, V. Buddolla, Ed., Academic Press, 2019, pp. 107–125. doi: 10.1016/B978-0-12-816328-3.00009-X.

[46] J. B. Pyser, S. Chakrabarty, E. O. Romero, and A. R. H. Narayan, "State-of-the-Art Biocatalysis," *ACS Cent. Sci.*, vol. 7, no. 7, pp. 1105–1116, Jul. 2021, doi: 10.1021/acscentsci.1c00273.

[47] C. K. Winkler, J. H. Schrittwieser, and W. Kroutil, “Power of Biocatalysis for Organic Synthesis,” *ACS Cent. Sci.*, vol. 7, no. 1, pp. 55–71, Jan. 2021, doi: 10.1021/acscentsci.0c01496.

[48] S. Wu, R. Snajdrova, J. C. Moore, K. Baldenius, and U. T. Bornscheuer, “Biocatalysis: Enzymatic Synthesis for Industrial Applications,” *Angewandte Chemie International Edition*, vol. 60, no. 1, pp. 88–119, 2021, doi: 10.1002/anie.202006648.

[49] E. Torres and M. Ayala, “6.24 - Biocatalysis by Metalloenzymes,” in *Comprehensive Inorganic Chemistry II (Second Edition)*, J. Reedijk and K. Poeppelmeier, Eds., Amsterdam: Elsevier, 2013, pp. 685–735. doi: 10.1016/B978-0-08-097774-4.00625-2.

[50] H. J. Edenberg and W. F. Bosron, “4.06 - Alcohol Dehydrogenases,” in *Comprehensive Toxicology (Second Edition)*, C. A. McQueen, Ed., Oxford: Elsevier, 2010, pp. 111–130. doi: 10.1016/B978-0-08-046884-6.00406-1.

[51] C. Hertweck and W. Boland, “Horse liver alcohol dehydrogenase (HLADH); biocatalytic redox-transformations in organic synthesis,” *Journal für Praktische Chemie/Chemiker-Zeitung*, 1997, Accessed: Dec. 30, 2022. [Online]. Available: https://onlinelibrary.wiley.com/doi/abs/10.1002/prac.199733901137

[52] J. Luo and T. C. Bruice, “Dynamic Structures of Horse Liver Alcohol Dehydrogenase (HLADH): Results of Molecular Dynamics Simulations of HLADH-NAD+-PhCH2OH, HLADH-NAD+-PhCH2O-, and HLADH-NADH-PhCHO,” *J. Am. Chem. Soc.*, vol. 123, no. 48, pp. 11952–11959, Dec. 2001, doi: 10.1021/ja0109747.

[53] B. Orlich, H. Berger, M. Lade, and R. Schomäcker, “Stability and activity of alcohol dehydrogenases in W/O-microemulsions: Enantioselective reduction including cofactor regeneration,” *Biotechnology and Bioengineering*, 2000, Accessed: Mar. 11, 2023. [Online]. Available: https://onlinelibrary.wiley.com/doi/abs/10.1002/1097-0290%2820001220%2970%3A6%3C638%3A%3AAID-BIT5%3E3.0.CO%3B2-%23

[54] J. Boyle, “Lehninger principles of biochemistry (4th ed.): Nelson, D., and Cox, M.,” *Biochemistry and Molecular Biology Education*, vol. 33, no. 1, pp. 74–75, 2005, doi: 10.1002/bmb.2005.494033010419.

[55] R. P. D. Bank, “RCSB PDB: Homepage.” https://www.rcsb.org/ (accessed Apr. 26, 2023).

[56] H. J. Team, “NADH Reviews - What Is The Function of NADH In Your Body,” *Health Jade*, Aug. 16, 2018. https://healthjade.com/nadh/ (accessed Apr. 26, 2023).

[57] "1,4-Dihydronicotinamide adenine dinucleotide | C21H29N7O14P2 | CID 439153 - PubChem." https://pubchem.ncbi.nlm.nih.gov/compound/1_4-Dihydronicotinamide-adenine-dinucleotide#section=3D-Conformer (accessed Jul. 18, 2023).

[58] L. Gorton and E. Domínguez, "Electrocatalytic oxidation of NAD(P) H at mediator-modified electrodes," *J Biotechnol*, vol. 82, no. 4, pp. 371–392, Feb. 2002, doi: 10.1016/s1389-0352(01)00053-8.

[59] S. Immanuel, R. Sivasubramanian, R. Gul, and M. A. Dar, "Recent Progress and Perspectives on Electrochemical Regeneration of Reduced Nicotinamide Adenine Dinucleotide (NADH)," *Chemistry – An Asian Journal*, vol. 15, no. 24, pp. 4256–4270, 2020, doi: 10.1002/asia.202001035.

[60] S. H. Lee, D. H. Nam, and C. B. Park, "Screening Xanthene Dyes for Visible Light-Driven Nicotinamide Adenine Dinucleotide Regeneration and Photoenzymatic Synthesis," *Advanced Synthesis & Catalysis*, vol. 351, no. 16, pp. 2589–2594, 2009, doi: 10.1002/adsc.200900547.

[61] G. T. Höfler *et al.*, "A Photoenzymatic NADH Regeneration System," *Chembiochem*, vol. 19, no. 22, pp. 2344–2347, Nov. 2018, doi: 10.1002/cbic.201800530.

[62] S. Lee, J. Ryu, D. H. Nam, and C. Park, "Photoenzymatic synthesis through sustainable NADH regeneration by SiO2-supported quantum dots," *Chemical communications (Cambridge, England)*, vol. 47, pp. 4643–5, Feb. 2011, doi: 10.1039/c0cc05246a.

[63] N. H. Pham, F. Hollmann, D. Kracher, M. Preims, D. Haltrich, and R. Ludwig, "Engineering an enzymatic regeneration system for NAD(P)H oxidation," *Journal of Molecular Catalysis B: Enzymatic*, vol. 120, pp. 38–46, Oct. 2015, doi: 10.1016/j.molcatb.2015.06.011.

[64] C. Cocuzza *et al.*, "Simultaneous CO2 reduction and NADH regeneration using formate and glycerol dehydrogenase enzymes co-immobilized on modified natural zeolite," *RSC Adv.*, vol. 12, no. 48, pp. 31142–31155, Oct. 2022, doi: 10.1039/D2RA03459J.

[65] L. Tensi and A. Macchioni, "Extremely Fast NADH-Regeneration Using Phosphonic Acid as Hydride Source and Iridium-pyridine-2-sulfonamidate Catalysts," *ACS Catal.*, vol. 10, no. 14, pp. 7945–7949, Jul. 2020, doi: 10.1021/acscatal.0c02261.

[66] T. Saba, J. Li, J. W. H. Burnett, R. F. Howe, P. N. Kechagiopoulos, and X. Wang, "NADH Regeneration: A Case Study of Pt-Catalyzed NAD+ Reduction with H2," *ACS Catal.*, vol. 11, no. 1, pp. 283–289, Jan. 2021, doi: 10.1021/acscatal.0c04360.

[67] S. Minteer, B. Tan, D. Hickey, R. Milton, and F. Giroud, "Regeneration of the NADH Cofactor by a Rhodium Complex Immobilized on Multi-Walled

Carbon Nanotubes," *Journal of The Electrochemical Society*, vol. 162, Jan. 2015, doi: 10.1149/2.0111503jes.

[68] I. Ali, B. Soomro, and S. Omanovic, "Electrochemical regeneration of NADH on a glassy carbon electrode surface: The influence of electrolysis potential," *Electrochemistry Communications*, vol. 13, no. 6, pp. 562–565, Jun. 2011, doi: 10.1016/j.elecom.2011.03.010.

[69] W. Li, C. Zhang, Z. Zheng, X. Zhang, L. Zhang, and A. Kuhn, "Fine-Tuning the Electrocatalytic Regeneration of NADH Cofactor Using [Rh(Cp*)(bpy)Cl]+-Functionalized Metal–Organic Framework Films," *ACS Appl. Mater. Interfaces*, vol. 14, no. 41, pp. 46673–46681, Oct. 2022, doi: 10.1021/acsami.2c13631.

[70] C. Corbari, G. Ravazzani, M. Galvagno, E. Cremonese, and M. Mancini, "Assessing Crop Coefficients for Natural Vegetated Areas Using Satellite Data and Eddy Covariance Stations," *Sensors (Basel)*, vol. 17, no. 11, Nov. 2017, doi: 10.3390/s17112664.

[71] X. Wang, T. Saba, H. H. P. Yiu, R. F. Howe, J. A. Anderson, and J. Shi, "Cofactor NAD(P)H Regeneration Inspired by Heterogeneous Pathways," *Chem*, vol. 2, no. 5, pp. 621–654, May 2017, doi: 10.1016/j.chempr.2017.04.009.

[72] L. Han and B. Liang, "New approaches to NAD(P)H regeneration in the biosynthesis systems," *World J Microbiol Biotechnol*, vol. 34, no. 10, p. 141, Sep. 2018, doi: 10.1007/s11274-018-2530-8.

[73] J. Nishigaki, T. Ishida, T. Honma, and M. Haruta, "Oxidation of β-Nicotinamide Adenine Dinucleotide (NADH) by Au Cluster and Nanoparticle Catalysts Aiming for Coenzyme Regeneration in Enzymatic Glucose Oxidation," *ACS Sustainable Chem. Eng.*, vol. 8, no. 28, pp. 10413–10422, Jul. 2020, doi: 10.1021/acssuschemeng.0c01893.

[74] E. Steckhan, S. Herrmann, R. Ruppert, E. Dietz, M. Frede, and E. Spika, "Analytical study of a series of substituted (2,2'-bipyridyl)(pentamethylcyclopentadienyl)rhodium and -iridium complexes with regard to their effectiveness as redox catalysts for the indirect electrochemical and chemical reduction of NAD(P)+," *Organometallics*, vol. 10, no. 5, pp. 1568–1577, May 1991, doi: 10.1021/om00051a056.

[75] C. L. Pitman, O. N. L. Finster, and A. J. M. Miller, "Cyclopentadiene-mediated hydride transfer from rhodium complexes," *Chem. Commun.*, vol. 52, no. 58, pp. 9105–9108, Jul. 2016, doi: 10.1039/C6CC00575F.

[76] J. Liu and M. Antonietti, "Bio-inspired NADH regeneration by carbon nitride photocatalysis using diatom templates," *Energy Environ. Sci.*, vol. 6, no. 5, pp. 1486–1493, Apr. 2013, doi: 10.1039/C3EE40696B.

[77] F. Hollmann, B. Witholt, and A. Schmid, "[Cp∗Rh(bpy)(H2O)]2+: a versatile tool for efficient and non-enzymatic regeneration of nicotinamide and flavin coenzymes," *Journal of Molecular Catalysis B: Enzymatic*, vol. 19–20, pp. 167–176, Dec. 2002, doi: 10.1016/S1381-1177(02)00164-9.

[78] L. Zhang *et al.*, "Versatile (Pentamethylcyclopentadienyl)rhodium-2,2′-Bipyridine (Cp*Rh-bpy) Catalyst for Transfer Hydrogenation of N-Heterocycles in Water," *Advanced Synthesis & Catalysis*, vol. 357, no. 16–17, pp. 3529–3537, 2015, doi: 10.1002/adsc.201500491.

[79] V. Ganesan, D. Sivanesan, and S. Yoon, "Correlation between the Structure and Catalytic Activity of [Cp*Rh(Substituted Bipyridine)] Complexes for NADH Regeneration," *Inorganic Chemistry*, vol. 56, Jan. 2017, doi: 10.1021/acs.inorgchem.6b02474.

[80] S. Inagaki, Y. Maegawa, M. Waki, and T. Himiyama, "Cooperative Catalysis of an Alcohol Dehydrogenase and Rhodium-Modified Periodic Mesoporous Organosilica - Himiyama - 2019 - Angewandte Chemie International Edition - Wiley Online Library," 2019, Accessed: Nov. 11, 2022. [Online]. Available: https://onlinelibrary.wiley.com/doi/abs/10.1002/anie.201904116

[81] M. Poizat, I. W. C. E. Arends, and F. Hollmann, "On the nature of mutual inactivation between [Cp*Rh(bpy)(H2O)]2+ and enzymes – analysis and potential remedies," *Journal of Molecular Catalysis B: Enzymatic*, vol. 63, no. 3, pp. 149–156, May 2010, doi: 10.1016/j.molcatb.2010.01.006.

[82] M. Sohrabi, M. Saeedi, B. Larijani, and M. Mahdavi, "Recent advances in biological activities of rhodium complexes: Their applications in drug discovery research," *European Journal of Medicinal Chemistry*, vol. 216, p. 113308, Apr. 2021, doi: 10.1016/j.ejmech.2021.113308.

[83] M. O. Ivanytsya, S. V. Ryabukhin, D. M. Volochnyuk, and S. V. Kolotilov, "Modern Approaches to the Creation of Immobilized Metal-Complex Catalysts for Hydrogenation, Alkene Metathesis, and Cross-Coupling Processes: A Review," *Theor Exp Chem*, vol. 56, no. 5, pp. 283–308, Nov. 2020, doi: 10.1007/s11237-020-09660-4.

[84] E. C. Constable and C. E. Housecroft, "The Early Years of 2,2'-Bipyridine-A Ligand in Its Own Lifetime," *Molecules*, vol. 24, no. 21, p. 3951, Oct. 2019, doi: 10.3390/molecules24213951.

[85] C. Kaes, A. Katz, and M. W. Hosseini, "Bipyridine: The Most Widely Used Ligand. A Review of Molecules Comprising at Least Two 2,2'-Bipyridine Units," *Chem. Rev.*, vol. 100, no. 10, pp. 3553–3590, Oct. 2000, doi: 10.1021/cr990376z.

[86] S. Shimizu *et al.*, "Pyridine and Pyridine Derivatives," in *Ullmann's Encyclopedia of Industrial Chemistry*, John Wiley & Sons, Ltd, 2000. doi: 10.1002/14356007.a22_399.

[87] W.-H. Wang, Y. Suna, Y. Himeda, J. T. Muckerman, and E. Fujita, “Functionalized cyclopentadienyl rhodium(III) bipyridine complexes: synthesis, characterization, and catalytic application in hydrogenation of ketones,” *Dalton Trans.*, vol. 42, no. 26, pp. 9628–9636, Jun. 2013, doi: 10.1039/C3DT50445J.

[88] D. Amarante, C. Cherian, and E. G. Megehee, “Synthesis and electronic characterization of mixed diimine ligand rhodium(III) complexes using a versatile triflate precursor,” *Inorganica Chimica Acta*, vol. 461, pp. 239–247, May 2017, doi: 10.1016/j.ica.2017.02.011.

[89] R. Dorta, R. Dorta, L. J. W. Shimon, and D. Milstein, “New ligand systems incorporating two and three 4,4’-bipyridine units. Characterization of bi- and trimetallic rhodium and iridium complexes,” *Inorg Chem*, vol. 43, no. 22, pp. 7180–7186, Nov. 2004, doi: 10.1021/ic049285x.

[90] D. Amarante *et al.*, “Improved synthetic routes to rhodium bipyridine complexes: Comparison of microwave vs. conventional synthesis,” *Inorganica Chimica Acta*, vol. 358, no. 7, pp. 2231–2238, Apr. 2005, doi: 10.1016/j.ica.2005.01.024.

[91] F. Hoffmann, M. Cornelius, J. Morell, and M. Fröba, “Periodic Mesoporous Organosilicas (PMOs): Past, Present, and Future,” *Journal of nanoscience and nanotechnology*, vol. 6, pp. 265–88, Mar. 2006, doi: 10.1166/jnn.2006.902.

[92] B. Karimi, N. Ganji, O. Pourshiani, and W. R. Thiel, “Periodic mesoporous organosilicas (PMOs): From synthesis strategies to applications,” *Progress in Materials Science*, vol. 125, p. 100896, Apr. 2022, doi: 10.1016/j.pmatsci.2021.100896.

[93] P. V. D. Voort, D. Esquivel, E. D. Canck, F. Goethals, I. V. Driessche, and F. J. Romero-Salguero, “Periodic Mesoporous Organosilicas: from simple to complex bridges; a comprehensive overview of functions, morphologies and applications,” *Chem. Soc. Rev.*, vol. 42, no. 9, pp. 3913–3955, Apr. 2013, doi: 10.1039/C2CS35222B.

[94] M. Waki and S. Inagaki, “Metal scavenging and catalysis by periodic mesoporous organosilicas with 2,2′-bipyridine metal chelating ligands,” *Applied Organometallic Chemistry*, vol. 35, no. 10, p. e6341, 2021, doi: 10.1002/aoc.6341.

[95] M. Waki, S. Shirai, K. Yamanaka, Y. Maegawa, and S. Inagaki, “Heterogeneous water oxidation photocatalysis based on periodic mesoporous organosilica immobilizing a tris(2,2′-bipyridine)ruthenium sensitizer,” *RSC Adv*, vol. 10, no. 24, pp. 13960–13967, doi: 10.1039/d0ra00895h.

[96] A. M. Kaczmarek, Y. Maegawa, A. Abalymov, A. G. Skirtach, S. Inagaki, and P. Van Der Voort, “Lanthanide-Grafted Bipyridine Periodic Mesoporous

Organosilicas (BPy-PMOs) for Physiological Range and Wide Temperature Range Luminescence Thermometry," *ACS Appl. Mater. Interfaces*, vol. 12, no. 11, pp. 13540–13550, Mar. 2020, doi: 10.1021/acsami.0c01470.

[97] Y. Naganawa *et al.*, "Heterogeneous hydrosilylation reaction catalysed by platinum complexes immobilized on bipyridine-periodic mesoporous organosilicas," *Dalton Trans.*, vol. 48, no. 17, pp. 5534–5540, Apr. 2019, doi: 10.1039/C9DT00078J.

[98] K. Matsui, Y. Maegawa, M. Waki, S. Inagaki, and Y. Yamamoto, "Transfer hydrogenation of nitrogen heterocycles using a recyclable rhodium catalyst immobilized on bipyridine-periodic mesoporous organosilica," *Catal. Sci. Technol.*, vol. 8, no. 2, pp. 534–539, Jan. 2018, doi: 10.1039/C7CY02167D.

[99] M. Kanai and M. Beller, "Introduction to hybrid catalysis," *Organic & Biomolecular Chemistry*, vol. 19, no. 4, pp. 702–704, 2021, doi: 10.1039/D0OB90177F.

[100] D. N. Tran and K. J. Jr. Balkus, "Perspective of Recent Progress in Immobilization of Enzymes," *ACS Catal.*, vol. 1, no. 8, pp. 956–968, Aug. 2011, doi: 10.1021/cs200124a.

[101] M. Romero-Fernández and F. Paradisi, "General Overview on Immobilization Techniques of Enzymes for Biocatalysis," in *Catalyst Immobilization*, John Wiley & Sons, Ltd, 2020, pp. 409–435. doi: 10.1002/9783527817290.ch12.

[102] D.-M. Liu, J. Chen, and Y.-P. Shi, "Advances on methods and easy separated support materials for enzymes immobilization," *TrAC Trends in Analytical Chemistry*, vol. 102, pp. 332–342, May 2018, doi: 10.1016/j.trac.2018.03.011.

[103] N. R. Mohamad, N. H. C. Marzuki, N. A. Buang, F. Huyop, and R. A. Wahab, "An overview of technologies for immobilization of enzymes and surface analysis techniques for immobilized enzymes," *Biotechnol Biotechnol Equip*, vol. 29, no. 2, pp. 205–220, Mar. 2015, doi: 10.1080/13102818.2015.1008192.

[104] G. Cirillo, F. Nicoletta, M. Curcio, U. Spizzirri, N. Picci, and F. Iemma, "Enzyme immobilization on smart polymers: Catalysis on demand," *Reactive and Functional Polymers*, vol. 83, Oct. 2014, doi: 10.1016/j.reactfunctpolym.2014.07.010.

[105] C. Zhang and X.-H. Xing, "2.23 - Enzyme Bioreactors," in *Comprehensive Biotechnology (Second Edition)*, M. Moo-Young, Ed., Burlington: Academic Press, 2011, pp. 319–329. doi: 10.1016/B978-0-08-088504-9.00099-4.

[106] D. Zhang, H. Hegab, Y. Lvov, L. Snow, and J. Palmer, "Immobilization of cellulase on a silica gel substrate modified using a 3-APTES self-assembled

monolayer," *SpringerPlus*, vol. 5, Dec. 2016, doi: 10.1186/s40064-016-1682-y.

[107] N. S. K. Gunda, M. Singh, L. Norman, K. Kaur, and S. K. Mitra, "Optimization and characterization of biomolecule immobilization on silicon substrates using (3-aminopropyl)triethoxysilane (APTES) and glutaraldehyde linker," *Applied Surface Science*, vol. 305, pp. 522–530, Jun. 2014, doi: 10.1016/j.apsusc.2014.03.130.

[108] J. de O. N. Ribeiro *et al.*, "Role of the type of grafting solvent and its removal process on APTES functionalization onto SBA-15 silica for CO2 adsorption," *J Porous Mater*, vol. 26, no. 6, pp. 1581–1591, Dec. 2019, doi: 10.1007/s10934-019-00754-6.

[109] D. Norouzian, "Enzyme immobilization : the state of art in biotechnology," 2003. Accessed: Apr. 02, 2023. [Online]. Available: https://www.semanticscholar.org/paper/Enzyme-immobilization-%3A-the-state-of-art-in-Norouzian/20c73f81dc1bfbb367dc390d16ee4e1a583e8428

[110] H. T. Imam, P. C. Marr, and A. C. Marr, "Enzyme entrapment, biocatalyst immobilization without covalent attachment," *Green Chem.*, vol. 23, no. 14, pp. 4980–5005, Jul. 2021, doi: 10.1039/D1GC01852C.

[111] D. P. Debecker, V. Smeets, M. Van der Verren, H. Meersseman Arango, M. Kinnaer, and F. Devred, "Hybrid chemoenzymatic heterogeneous catalysts," *Current Opinion in Green and Sustainable Chemistry*, vol. 28, p. 100437, Apr. 2021, doi: 10.1016/j.cogsc.2020.100437.

[112] S. González-Granda, J. Albarrán-Velo, I. Lavandera, and V. Gotor-Fernández, "Expanding the Synthetic Toolbox through Metal–Enzyme Cascade Reactions," *Chem. Rev.*, Jan. 2023, doi: 10.1021/acs.chemrev.2c00454.

[113] X. Li, X. Cao, J. Xiong, and J. Ge, "Enzyme–Metal Hybrid Catalysts for Chemoenzymatic Reactions," *Small*, vol. 16, no. 15, p. 1902751, 2020, doi: 10.1002/smll.201902751.

[114] M. Xu, Z. Tan, C. Zhu, W. Zhuang, H. Ying, and P. Ouyang, "Recent advance of chemoenzymatic catalysis for the synthesis of chemicals: Scope and challenge," *Chinese Journal of Chemical Engineering*, vol. 30, pp. 146–167, Feb. 2021, doi: 10.1016/j.cjche.2020.12.016.

[115] S. Itsuno, "Enantioselective Reduction of Ketones," in *Organic Reactions*, John Wiley & Sons, Ltd, 2004, pp. 395–576. doi: 10.1002/0471264180.or052.02.

[116] Z. Dalicsek, F. Pollreisz, Á. Gömöry, and T. Soós, "Recoverable Fluorous CBS Methodology for Asymmetric Reduction of Ketones," *Org. Lett.*, vol. 7, no. 15, pp. 3243–3246, Jul. 2005, doi: 10.1021/ol051024j.

[117] L. Zheng *et al.*, "Asymmetric Catalytic Meerwein–Ponndorf–Verley Reduction of Ketones with Aluminum(III)-VANOL Catalysts," *ACS Catal.*, vol. 10, no. 13, pp. 7188–7194, Jul. 2020, doi: 10.1021/acscatal.0c01734.

[118] K. Nishide and M. Node, "Recent development of asymmetric syntheses based on the Meerwein-Ponndorf-Verley reduction," *Chirality*, vol. 14, no. 10, pp. 759–767, Nov. 2002, doi: 10.1002/chir.10142.

[119] R. Cohen, C. R. Graves, S. T. Nguyen, J. M. L. Martin, and M. A. Ratner, "The Mechanism of Aluminum-Catalyzed Meerwein–Schmidt–Ponndorf–Verley Reduction of Carbonyls to Alcohols," *J. Am. Chem. Soc.*, vol. 126, no. 45, pp. 14796–14803, Nov. 2004, doi: 10.1021/ja047613m.

[120] L. Huang, G. V. Sayoga, F. Hollmann, and S. Kara, "Horse Liver Alcohol Dehydrogenase-Catalyzed Oxidative Lactamization of Amino Alcohols," *ACS Catal.*, vol. 8, no. 9, pp. 8680–8684, Sep. 2018, doi: 10.1021/acscatal.8b02355.

[121] V. Gascón, I. Díaz, R. M. Blanco, and C. Márquez-Álvarez, "Hybrid periodic mesoporous organosilica designed to improve the properties of immobilized enzymes," *RSC Adv.*, vol. 4, no. 65, pp. 34356–34368, Aug. 2014, doi: 10.1039/C4RA05362A.

[122] W. Bensch, L. Kienle, U. Schürmann, and J. Timm, "High azobenzene functionalization enhances stability of the cis isomer: Periodic mesoporous organosilica network on the way to new light triggered applicable materials - ScienceDirect," 2016, Accessed: Mar. 26, 2023. [Online]. Available: https://www.sciencedirect.com/science/article/abs/pii/S1387181116300531

[123] van den Biggelaar, "Design of heterogeneous biocatalysts for flow chemical processes : towards a greener transamination reaction," UCL - Université Catholique de Louvain, 2018. Accessed: Mar. 26, 2023. [Online]. Available: https://dial.uclouvain.be/pr/boreal/object/boreal:207945

[124] T. Itozawa and H. Kise, "Immobilization of HLADH on polymer materials for reduction of cyclohexanone with NADH regeneration under two-phase conditions," *Journal of Fermentation and Bioengineering*, vol. 80, no. 1, pp. 30–34, Jan. 1995, doi: 10.1016/0922-338X(95)98172-H.

[125] H. Wang and P. K. Chu, "Chapter 4 - Surface Characterization of Biomaterials," in *Characterization of Biomaterials*, A. Bandyopadhyay and S. Bose, Eds., Oxford: Academic Press, 2013, pp. 105–174. doi: 10.1016/B978-0-12-415800-9.00004-8.

[126] S. Hudson, D. A. Tanner, W. Redington, E. Magner, K. Hodnett, and S. Nakahara, "Quantitative TEM analysis of a hexagonal mesoporous silicate

structure," *Phys. Chem. Chem. Phys.*, vol. 8, no. 29, pp. 3467–3474, Jul. 2006, doi: 10.1039/B605581H.

[127] J. R. Durig and D. W. Wertz, "Spectroscopic Review of the Normal Vibrations of Metal Complexes with Nitrogen-Containing Ligands," *Appl. Spectrosc., AS*, vol. 22, no. 6, pp. 627–633, Nov. 1968.

[128] M. Waki *et al.*, "A Solid Chelating Ligand: Periodic Mesoporous Organosilica Containing 2,2′-Bipyridine within the Pore Walls," *J. Am. Chem. Soc.*, vol. 136, no. 10, pp. 4003–4011, Mar. 2014, doi: 10.1021/ja4131609.

[129] H. Matsukawa *et al.*, "Fast and stable vapochromic response induced through nanocrystal formation of a luminescent platinum(II) complex on periodic mesoporous organosilica," *Scientific Reports*, vol. 9, p. 15151, Oct. 2019, doi: 10.1038/s41598-019-51615-w.

[130] S. Zhang, H. Wang, M. Li, J. Han, X. Liu, and J. Gong, "Molecular heterogeneous catalysts derived from bipyridine-based organosilica nanotubes for C–H bond activation †Electronic supplementary information (ESI) available: Experimental details, material characterization data, catalytic measurement details. See DOI: 10.1039/c7sc00713b Click here for additional data file.," *Chem Sci*, vol. 8, no. 6, pp. 4489–4496, Jun. 2017, doi: 10.1039/c7sc00713b.

[131] M. Bandyopadhyay, N. Tsunoji, and T. Sano, "Mesoporous MCM-48 Immobilized with Aminopropyltriethoxysilane: A Potential Catalyst for Transesterification of Triacetin," *Catal Lett*, vol. 147, no. 4, pp. 1040–1050, Apr. 2017, doi: 10.1007/s10562-017-1997-5.

[132] M. Impéror-Clerc, P. Davidson, and A. Davidson, "Existence of a Microporous Corona around the Mesopores of Silica-Based SBA-15 Materials Templated by Triblock Copolymers," *J. Am. Chem. Soc.*, vol. 122, no. 48, pp. 11925–11933, Dec. 2000, doi: 10.1021/ja002245h.

[133] D. F. Enache *et al.*, "Schiff base-functionalized mesoporous silicas (MCM-41, HMS) as Pb(ii) adsorbents," *RSC Advances*, vol. 8, no. 1, pp. 176–189, 2018, doi: 10.1039/C7RA12310H.

[134] R.-A. Mitran, S. Nastase, C. Matei, and D. Berger, "Tailoring the dissolution rate enhancement of aminoglutethimide by functionalization of MCM-41 silica: a hydrogen bonding propensity approach," *RSC Adv.*, vol. 5, no. 4, pp. 2592–2601, Dec. 2014, doi: 10.1039/C4RA11224E.

[135] J. A. Bae, K.-C. Song, J.-K. Jeon, Y. S. Ko, Y.-K. Park, and J.-H. Yim, "Effect of pore structure of amine-functionalized mesoporous silica-supported rhodium catalysts on 1-octene hydroformylation," *Microporous and Mesoporous Materials*, vol. 123, no. 1, pp. 289–297, Jul. 2009, doi: 10.1016/j.micromeso.2009.04.015.

[136] P. Silvina, “An accurate UV/visible method to quantify proteins and enzymes: Impact of aggregation, buffer concentration and the nature of the standard,” *Current Topics in Analytical Chemistry*, vol. 8, Jan. 2011.

[137] V. Smeets *et al.*, “Hollow zeolite microspheres as a nest for enzymes: a new route to hybrid heterogeneous catalysts,” *Chemical Science*, vol. 11, no. 4, pp. 954–961, 2020, doi: 10.1039/C9SC04615A.

Hybrid catalysis for stereoselective ketone reduction

Presented by Aurélien Doutry

Production of chiral alcohol in pharmaceutical industries has a huge impact on the environment. The utilization of current homogeneous catalysts for asymmetric reduction generates wasted chemicals for the synthesis of the catalyst and post purification of the pharmaceutical's drugs. Moreover, for the reduction of ketones to chiral alcohol, stoichiometric concentration of NADH needs to be provided. The combination of an active metal for the regeneration of NADH and an enzyme for the synthesis of chiral alcohol is impossible because there is a mutual inactivation. New catalysts with the heterogenization of a metal active and an enzyme appear to be the future generation of catalysts. This combination generates good activity and enantioselectivity. This master thesis aims to study a hybrid catalyst for stereoselective ketone reduction.

The hybrid catalyst used in this case is the combination of a rhodium complex and an alcohol dehydrogenase (HLADH). The enzyme is used to reduce an alcohol into a ketone in presence of NADH as an electron donor and produce NAD+. The regeneration of NADH is done by the oxidation of NAD+ in presence of formate with the rhodium as catalysts. The enzyme and the rhodium are supported on special material: bipyridine-periodic-mesoporous-organosilica (Bpy-PMO). PMO are new materials with uniform pores, huge specific surface and highly functionalization capability. The presence of Bypiridine inside the PMO allows the immobilization of rhodium complex and the hydroxyl group serve for the immobilization of the enzyme.

This work focuses on a model reaction. It is the reduction of 4-phenyl-2-butabone into 4-phenyl-2-butanol with in parallel the regeneration of NADH with formate as electrons donor. The study of the reaction conditions for the reduction by HLADH and rhodium complex for the regeneration was done. Rh@Bpy-PMO as catalysts demonstrates his capacity to degrade the substrates to regenerate NADH degradation in homogeneous phase, Rh@Bpy-PMO as regeneration catalyst and the interaction between HLADH and Rh@Bpy-PMO was studied. The immobilization of HLADH by APTES demonstrates remaining activity but also massive textural changes for the support of the decrease of the specific area. The current hybrid catalyst has shown no activity for the alcohol reduction, but some other possible strategies can be tested.

UNIVERSITÉ CATHOLIQUE DE LOUVAIN
Faculté des bioingénieurs
Croix du Sud, 2 bte L7.05.01, 1348 Louvain-la-Neuve, Belgique | **www.uclouvain.be/agro**